9-10-2014 12:00 AM

Investigation of Fracture Toughness Measurement for Pipeline Steels Based on SE(B) and SE(T) Specimens

Zijian Yan
The University of Western Ontario

Supervisor
Dr. Wenxing Zhou
The University of Western Ontario

Graduate Program in Civil and Environmental Engineering
A thesis submitted in partial fulfillment of the requirements for the degree in Master of Engineering Science

INVESTIGATION OF FRACTURE TOUGHNESS MEASUREMENT FOR PIPELINE STEELS BASED ON SE(B) AND SE(T) SPECIMENS

(Thesis format: Integrated Article)

by

Zijian Yan

Graduate Program in Engineering Science
Department of Civil and Environmental Engineering

A thesis submitted in partial fulfillment
of the requirements for the degree of
Master of Engineering Science

The School of Graduate and Postdoctoral Studies
The University of Western Ontario
London, Ontario, Canada

ABSTRACT

This thesis deals with issues related to the experimental determination of the fracture toughness resistance curves, i.e. the J-integral (*J*)-R curve and crack tip opening displacement (*CTOD*)-R curves, using the single-edge bend (SE(B)) and single-edge tension (SE(T)) specimens. First, the impact of the crack front curvature on the *J-R* curve measured from the SE(B) specimen is investigated through systematic linear-elastic and elastic-plastic three-dimensional (3D) finite element analyses (FEA) of SE(B) specimens containing both straight and curved crack fronts. Three average relative crack lengths are considered, namely 0.3, 0.5 and 0.7, and three specimen width-to-thickness ratios are considered: 0.25, 0.5 and 1. The curved crack fronts are characterized by a power-law expression. The analysis results suggest that the crack length evaluated from the *CMOD* compliance of the SE(B) specimen is insensitive to the crack front curvature and that the impact of the crack front curvature on the experimentally-evaluated *J* values varies with the specimen configurations. For a given specimen configuration, as the crack front curvature increases, the value of *J* evaluated based on the test standard ASTM E1820-11 without considering the crack front curvature becomes less conservative and tends to overestimate the actual *J*. New crack front straightness criteria that are in most cases less stringent than ASTM E1820-11, are recommended. The accuracy of the double clip-on gauge method for experimentally determining *CTOD* is examined through systematic 3D elastic-plastic large-strain FEA of clamped SE(T) specimens. The relative crack lengths of the specimens range from 0.3 to 0.7, and the thickness-to-width ratios are 0.5, 1 and 2. It is observed that the *CTOD* values determined from the double clip-on gauge method may involve significant errors. This error primarily depends on the crack length, the material property and the loading level. Based on the analysis results, a modified *CTOD* evaluation equation is developed to improve the accuracy of *CTOD* evaluated using the double-clip on gauge method.

Keywords

Fracture toughness; J-integral; Curved crack front; FEA; Crack tip opening displacement (*CTOD*); Double clip-on gauge; SE(B) specimen; SE(T) specimen

CO-AUTHORSHIP STATEMENT

The material presented in Chapter 2, 3 and 4 of this thesis have been published or submitted for potential publication in international conference proceedings or peer-reviewed journals. The permission to reproduce the published work in this thesis has been granted by the copyright holders and included at the end of this thesis.

A version of Chapter 2 has been published and presented as a technical paper co-authored by Zijian Yan and Wenxing Zhou in the *CSME International Congress*, Toronto, Ontario, Canada, June 1-4, 2014.

Chapter 3 contains materials of a manuscript co-authored by Zijian Yan and Wenxing Zhou that has been accepted for publication in the *Journal of Testing and Evaluation, ASTM International*. Reproduced in this chapter, with permission, from the *Journal of Testing and Evaluation*, copyright ASTM International, 100 Barr Harbor Drive, West Conshohocken PA 19428-2959.

A version of Chapter 4, co-authored by Zijian Yan, Yifan Huang and Wenxing Zhou, will be presented as an accepted technical paper and one of seven finalists in the 7th student paper competition in *the 10th International Pipeline Conference*, Calgary, Alberta, Canada, September 29- October 3, 2014. Paper No. IPC2014-33219.

DEDICATION

To my parents and grandparents

ACKNOWLEDGMENTS

This thesis was carried out in the Department of Civil and Environmental Engineering at Western. Foremost, I would like to express my most sincere gratitude to my supervisor Dr. Wenxing Zhou for his continuously patient guidance, support and encouragement throughout the completion of this program. His vast knowledge, enthusiasm and dedication to research were guiding me on a daily basis during the last two years. He was serious, sharp and precise to every discussion we had, which I believe are the crucial qualities for a researcher. I was fortunate enough to have the opportunity of being a member of his research group.

I would also like to thank my thesis committee members and examiners, Dr. Ashraf A. El Damatty, Dr. Timothy A. Newson and Dr. Liying Jiang for reviewing this thesis. I am certain that the quality of my thesis is improved by their minds and hands. The guidance from Dr. Hanping Hong as the supervisory committee member is also acknowledged.

Sincerely, I wish to extend my appreciation to my colleagues in the research group and all my friends in Canada, for their help, support and most of all the friendship they provided during the past two years. Their presence colored my personal life.

Financial support provided by TransCanada, Natural Sciences and Engineering Research Council of Canada (NSERC) and the Faculty of Engineering at the University of Western Ontario is gratefully acknowledged.

Finally, I would like to thank my parents and grandparents, for their continual support and encouragement in pursuit of higher levels of academia. It is to them that this thesis is dedicated.

TABLE OF CONTENTS

Abstract II

Co-authorship Statement III

Dedication IV

Acknowledgments V

Table of Contents VI

List of Tables IX

List of Figures X

List of Abbreviations and Symbols XIV

Chapter 1 Introduction 1

1.1 Background 1

1.2 Fundamentals of Fracture Mechanics 2

1.2.1 Linear Elastic Fracture Mechanics 2

1.2.2 Elastic Plastic Fracture Mechanics 4

1.3 Objective and Research Significance 8

1.3.1 Investigation of the Effect of Crack Front Curvature on the Measurement of *J-R* Curve of Single-Edge Bend Specimens 8

1.3.2 Investigation of the Accuracy of the Double-Clip on Gauge Method for Evaluating *CTOD* of Single-Edge Tension Specimens 8

1.4 Thesis Format and Outline 9

References 9

Chapter 2 Effect of Crack Front Curvature on *CMOD* Compliance and Crack Length Evaluation for Single-edge Bend Specimens 15

2.1 Introduction 15

2.1.1 Fracture Toughness Resistance Curve Tests on Small-scale Specimens .. 15

2.1.2 Literature Review and Objective 16
2.1.3 Approach 17
2.2 Characteristics of Curved Crack Front 18
2.3 Finite Element Analyses 21
2.4 Analysis and Discussions 22
2.4.1 Effect of the Crack Front Curvature on *CMOD* compliance 22
2.4.2 Crack Length - *COMD* Compliance Equations 23
2.4.3 Effect of the Crack Front Curvature on the Evaluated Crack Length 24
2.5 Summary and Concluding Remarks 25
References 26
Chapter 3 Effect of Crack Front Curvature on Experimental Evaluation of J-integral for Single-edge Bend Specimens 45
3.1 Introduction 45
3.1.1 Experimental Evaluation of *J* 45
3.1.2 Literature Review and Objective 48
3.1.3 Approach 49
3.2 Finite Element Analyses 50
3.2.1 Finite Element Model 50
3.2.2 Material Model 51
3.2.3 Computational Procedure 52
3.3 Results and Discussions 54
3.4 Summary and Concluding Remarks 56
Reference 57
Chapter 4 Accuracy of the Double Clip-on Gauge Method for Evaluating *CTOD* from Single-edge Tension Specimens 81

4.1 Introduction 81
4.1.1 Experimental Determination of *CTOD* 81
4.1.2 Single-edge Tension Specimen 83
4.1.3 Literature Review 84
4.1.4 Objective and Approach 84
4.2 *CTOD* Measured from Double Clip-on Gauge Method 85
4.3 Finite Element Analyses 86
4.3.1 Finite Element Model 86
4.3.2 Material Model 87
4.3.3 Computational Procedure 88
4.4 Results and Discussions 89
4.5 Summary and Concluding Remarks 92
Reference 93
Chapter 5 Summary and Conclusions 116
5.1 Effect of the Crack Front Curvature on the *CMOD* Compliance and *J* for SE(B) Specimens 116
5.2 Accuracy of the Double Clip-on Gauge Method for Evaluating *CTOD* of SE(T) Specimens 119
5.3 Recommendations for Future Work 120
Appendix A Derivation of the Relationship between β and λ for Symmetric Bowed Crack Fronts 121
Appendix B Computation of J-integral using Virtual Crack Extension Method 123
Reference 124
Appendix C Copyright Permission 128
Curriculum Vitae 135

LIST OF TABLES

Table 2.1: Summary of the curved crack fronts of the specimens collected in this study 28

Table 2.2: The coefficients used in Eq. (2.9)..... 29

Table 3.1: Recommended crack front straightness criteria for SE(B) specimens 60

LIST OF FIGURES

Figure 1.1. Three typical loading modes in fracture mechanics 12

Figure 1.2. Stress field solutions surrounding the crack tip 12

Figure 1.3. Arbitrary contour around the crack tip 13

Figure 1.4. Schematically illustration of *CTOD* definitions 14

Figure 2.1. Schematic and experiment set-up of small-scale specimens 32

Figure 2.2. *P-CMOD* curve using elastic unloading compliance method (Wang et al. 2012) 33

Figure 2.3. Schematic illustration of symmetric bowed crack fronts 34

Figure 2.4. Typical crack fronts of SE(B) and SE(T) specimens 34

Figure 2.5. Comparison of actual and fitted crack fronts for one SE(B) specimen and one SE(T) specimen 35

Figure 2.6. Schematic illustration of symmetric bowed crack fronts with a fixed β and varying p 36

Figure 2.7. Geometric and mesh configuration of the finite element model 37

Figure 2.8. Variation of C_c/C_s against λ 39

Figure 2.9. Variation of the error e_a against λ 44

Figure 3.1. Determination of the potential energy 61

Figure 3.2. Plastic area under the load-displacement curve 62

Figure 3.3. Variation of the error $e_J = (J^{\eta} - J^{FEA})/J^{FEA}$ against P/P_y for specimens with different values of a_{ave}/W, B/W and crack fronts curvature λ (*CMOD*-based analysis, $p = 3$ and $n = 10$) 66

Figure 3.4. Variation of the error $e_J = (J^{\eta} - J^{FEA})/J^{FEA}$ against P/P_y for specimens with different values of a_{ave}/W, B/W and crack fronts curvature λ (*LLD*-based analysis, $p = 3$ and $n = 10$) 70

Figure 3.5. Variation of the error $e_J = (J^{\eta} - J^{FEA})/J^{FEA}$ against P/P_y for specimens with different values of a_{ave}/W, B/W and crack fronts curvature λ (*CMOD*-based analysis, $p = 3$ and $n = 20$) 74

Figure 3.6. Variation of the error $e_J = (J^{\eta} - J^{FEA})/J^{FEA}$ against P/P_y for specimens with different values of a_{ave}/W, B/W and crack fronts curvature λ (*LLD*-based analysis, $p = 3$ and $n = 20$) 78

Figure 3.7. Impact of the shape parameter p ($p = 3$ and $p = 2.5$) on e_J 80

Figure 4.1. Schematically illustration of the geometric relationship for the evaluation of *CTOD* using single clip-on gauge plastic hinge model 98

Figure 4.2. Illustration of the installation of knife edges for the double clip-on gauge method 99

Figure 4.3. Typical toughness resistance curves for various types of small-scale specimens 100

Figure 4.4. Schematically illustration of *CTOD* definitions 101

Figure 4.5. Schematically illustration of the geometric relationship for the evaluation of *CTOD* 102

Figure 4.6. Geometric and mesh configuration of the finite element model with a blunt crack tip 102

Figure 4.7. A typical side-grooved finite element model for clamped SE(T) specimen 103

Figure 4.8. Schematically illustration of the determination of *CTOD* in FEA 104

Figure 4.9. Schematically illustration of the double clip-on gauge method in FEA 104

Figure 4.10. Variation of e_1 against *P/Py* for plane-sided specimens with n = 10 and the same *B/W* 105

Figure 4.11. Variation of e_1 against *P/Py* for plane-sided specimens with n = 10 and the same *a/W* 106

Figure 4.12. Variation of e_1 against *P/Py* for plane-sided specimens with *B/W* = 1 and the same *a/W* 107

Figure 4.13. Geometric relationship surrounding the blunt crack tip 108

Figure 4.14. Variation of the proposed correction factor μ against *P/Py* for plane-sided specimens with n = 10 109

Figure 4.15. Variation of the proposed correction factor μ against *P/Py* for specimens with n = 10 110

Figure 4.16. Variation of the proposed correction factor μ against *P/Py* for plane-sided specimens with *B/W* = 1, *a/W* = 0.5, n = 10 and different initial radius 111

Figure 4.17. Variation of the proposed correction factor μ against *P/Py* for plane-sided specimens with *B/W* = 1 and different n values 111

Figure 4.18. Variation of e_c against *P/Py* for plane-sided specimens with n = 10 and the same *B/W* 112

Figure 4.19. Variation of e_c against *P/Py* for plane-sided specimens with n = 10 and the same *a/W* 113

Figure 4.20. Variation of e_c against *P/Py* for specimens with n = 10, *B/W* = 1 and the same *a/W* 114

Figure 4.21. Variation of e_c against *P/Py* for plane-sided specimens with *B/W* = 1 and the same *a/W* 115

Figure B.1. The virtual crack extension method in two-dimensional analysis 126

Figure B.2. The virtual crack extension method in three-dimensional analysis 127

LIST OF ABBREVIATIONS AND SYMBOLS

Abbreviations

ASTM	American Society for Testing and Materials
CMOD	Crack mouth opening displacement
C(T)	Compact tension
CTOD	Crack tip opening displacement
DCG	Double clip-on gauge
DIC	Digital image correlation
EPFM	Elastic-plastic fracture mechanics
FEA	Finite element analyses
HRR	Hutchinson-Rice-Rosengren
LEFM	Linear-elastic fracture mechanics
LLD	Load line displacement
LSY	Large scale yielding
PS	Plane-sided
SE(B)	Single-edge bend
SE(T)	Single-edge tension
SSY	Small scale yielding
SG	Side-grooved
2D	Two dimensional
3D	Three dimensional

Symbols

CHAPTER 2

a	Crack length
$a(0)$	Crack length at the mid-plane of the specimen
$a(\pm B/2)$	Crack length at the surface of the specimen

a_{ave}	Average crack length
a_i	Crack length at the nine measurement points (i = 1, 2, …, 9)
a_{max9}	Maximum value of the nine physical measurements, a_{max9} = max (a_i) where i = 1, 2, …, 9
a_{max}	Maximum crack length over the entire crack front
a_{min9}	Minimum value of the nine physical measurements, a_{min9} = min (a_i) where i = 1, 2, …, 9
a_{min}	Minimum crack length over the entire crack front
a_p	Predicted crack length
A_i	Coefficients, i = 0, 1, …, 4
B	Specimen thickness
B_N	Net thickness for side-grooved specimens
C	Specimen compliance
C_c	Compliance for specimens with curved crack fronts
C_i	Measured specimen compliance at load step i
C_s	Compliance for specimens with straight fronts
e_a	Error, $e_a = (a_p - a_{ave})/a_{ave}$
E	Young's modulus
E_e	Effective modulus
E'	Elastic modulus corresponding to the plane strain condition, i.e. $E' = E/(1 - \nu^2)$
H	Daylight length for clamped SE(T) specimen
J	J-integral
p	A shape parameter
P	Applied load
S	Specimen span
W	Specimen width
x	Coordinate in the specimen thickness direction
β	Difference of relative crack lengths at the mid-plane and free surface, $\beta = a(0)/W - a(B/2)/W$
Δ	$\Delta = 0.005W$ for ASTM E1820-11

Δa	Crack growth
v	Poisson's ratio
λ	Characterizing the fatigue crack front curvature level in this study based on ASTM E1820-11, λ = max (a_{max9} - a_{ave}, a_{ave} - a_{min9})/B

CHAPTER 3

a	Crack length
a_{ave}	Average crack length
A	Total area under the load versus displacement curve
A_{el}	Elastic area under the load versus displacement curve
A_{pl}	Plastic area under the load versus displacement curve
A_{pl}^{CMOD}	Plastic area under the *P-CMOD* curve
A_{pl}^{LLD}	Plastic area under the *P-LLD* curve
B	Specimen thickness
da	Increment of crack length
dP	Increment of applied load
dU	Increment of strain energy
$d\Delta$	Increment of displacement
e	Base of the natural logarithm, e = 2.71828
e_J	Error, $e_J = (J^{\eta} - J^{FEA})/ J^{FEA}$
E	Young's modulus
H	Daylight length for clamped SE(T) specimen
J	J-integral
J^{FEA}	J-integral value from FEA considering crack front curvature
J_{el}	Elastic component of J-integral
J_{pl}	Plastic component of J-integral
J^{η}	J-integral value evaluated based on plastic geometry factor η_{pl} as specified in ASTM E1820-11
K	Linear elastic stress intensity factor
n	Strain hardening exponent
p	A shape parameter

P	Applied load
P_y	Reference load, $P_y = B(W - a_{ave})^2\sigma_Y/S$
S	Specimen span
U	Strain energy
W	Specimen width
α	A dimensionless parameter
β	Difference of relative crack lengths at the mid-plane and free surface, $\beta = a(0)/W - a(B/2)/W$
Δ	Specimen displacement
Δ_{el}	Elastic component of the specimen displacement
Δ_{pl}	Plastic component of the specimen displacement
ε	Strain
ε_0	Reference strain, satisfying $\varepsilon_0 = \sigma_0/E$
η	A dimensionless geometry factor
η_{pl}	Plastic geometry factor used to calculate J-integral
η_{pl}^{CMOD}	*CMOD*-based plastic geometry factor used to calculate J-integral
η_{pl}^{LLD}	*LLD*-based plastic geometry factor used to calculate J-integral
λ	Characterizing the fatigue crack front curvature level in this study based on ASTM E1820-11, $\lambda = \max(a_{max9} - a_{ave}, a_{ave} - a_{min9})/B$
ν	Poisson's ratio
σ	Stress
σ_0	Reference stress, equal to the yield strength σ_{YS} in this study
σ_{TS}	Ultimate tensile strength
σ_Y	Effective yield strength, $\sigma_Y = (\sigma_{YS} + \sigma_{TS})/2$ as specified in ASTM E1820-11
σ_{YS}	Yield strength

CHAPTER 4

a	Crack length
a_0	Original Crack length
B	Specimen thickness

e	Base of the natural logarithm, e = 2.71828
e_1	Error, $e_1 = (\delta_{DC90} - \delta_{FE90})/\delta_{FE90}$
e_c	Error of the DCG method by employing the modified equations, i.e. Eqs. (4.8), (4.9) and (4.10)
E	Young's modulus
J	J-integral
K	Linear elastic stress intensity factor
m	A dimensionless constraint factor
n	Strain hardening exponent
P	Applied load
P_y	Reference load, $P_y = B(W - a)\sigma_Y$
q_0, q_1 and q_2	Fitting coefficients
r_p	A dimensionless rotation factor
V_{pl}	Plastic component of the measured crack mouth opening displacement
V_{pl1}, V_{pl2}	Plastic component of the two measured crack mouth opening displacements corresponding to the two different knife edge heights in double clip-on gauge method
V_1, V_2	Two measured crack mouth opening displacements corresponding to the two different knife edge heights in double clip-on gauge method
W	Specimen width
z	The height of the clip-on gauge for single clip-on gauge method
z_1, z_2	The heights of the clip-on gauge for double clip-on gauge method
δ	Crack tip opening displacement (*CTOD*)
δ_{BS}	Crack tip opening displacement (*CTOD*) obtained based on BS 7448
δ_{DC90}	Crack tip opening displacement (*CTOD*) evaluated from double clip-on gauge method based on the 90 degree definition
δ_{FE90}	Crack tip opening displacement (*CTOD*) evaluated from FEA based on the 90 degree definition
δ_{el}	Elastic component of crack tip opening displacement (*CTOD*)
δ_{pl}	Plastic component of crack tip opening displacement (*CTOD*)

δ_{90}	Crack tip opening displacement (*CTOD*) based on the 90 degree definition
ε	Strain
ε_0	Reference strain, satisfying $\varepsilon_0 = \sigma_0/E$
η_{pl}	Plastic geometry factor used to calculate J-integral
θ	Rotational angle
μ	Proposed correction factor
ν	Poisson's ratio
ρ_0	The initial radius of the blunt crack tip in FEA model
σ	Stress
σ_0	Reference stress
σ_{TS}	Ultimate tensile strength
σ_Y	Effective yield strength, $\sigma_Y = (\sigma_{YS} + \sigma_{TS})/2$
σ_{YS}	Yield strength

Chapter 1 Introduction

1.1 Background

Pipelines are the safest and most effective means to transport large quantity of hydrocarbons (e.g. crude oil and natural gas) over a long distance and are vital to the economic well-being and security of a society. Canada has the largest crude oil pipeline network in the world. According to the Canadian Energy Pipeline Association, there are approximately 98 pipeline companies, which operate approximately 73,000 km of pipelines and approximately 1,400 km of international power lines across Canada (NEB 2012). In 2012, these pipelines shipped approximately $106.3 billion worth of crude oil, petroleum products, natural gas liquids and natural gas to Canadians and export customers at an estimated transportation cost of $6.9 billion (NEB 2012).

Energy pipelines may contain cracks or flaws due to various causes, such as the third party interference, fatigue, corrosion, stress-corrosion cracking (SCC) and welding process. The fracture toughness of the pipeline steel is a key input in the integrity assessment of pipelines containing cracks (i.e. planar defects) and the strain-based design of pipelines. For instance, the fracture toughness is related to the tolerable flaw sizes in the pipeline and governs the tensile strain capacity of the pipeline, e.g. the allowable longitudinal tensile strain in the pipeline girth weld containing circumferential cracks (Fairchild et al., 2012).

For ductile materials such as the modern pipeline steels, the fracture failure process is usually accompanied with significant plastic deformation. The ductile fracture behavior can lead to a slow and stable crack extension, which is a continuous process of ductile tearing. The material can carry more applied load with the growth of the crack length. In such circumstances, a relationship between the crack extension and the fracture toughness value (e.g. J-integral or crack tip opening displacement, see Section 1.2) corresponding to the crack extension, called fracture toughness resistance curve or *R*-curve, can be used to characterize the fracture toughness of ductile materials. The toughness resistance curves are commonly measured on small-scale specimens, e.g. three-point single-edge bend

(SE(B)), compact tension (C(T)) and single-edge tension (SE(T)) specimens. The objective of the study reported in this thesis is to address several issues related to the experimental determination of the fracture toughness resistance curve based on the SE(B) and SE(T) specimens. Some basic concepts of fracture mechanics are briefly reviewed first in Section 1.2.

1.2 Fundamentals of Fracture Mechanics

1.2.1 Linear Elastic Fracture Mechanics

Fracture mechanics deals with the behavior of bodies containing cracks and sharp notches, and is one of the most important development in the theory of mechanics. It can generally be separated into two domains: namely linear-elastic fracture mechanics (LEFM) and elastic-plastic fracture mechanics (EPFM). The former is valid if nonlinear deformation is confined to a small region in the vicinity of the crack tip, which is known as the small scale yielding (SSY) condition (Anderson, 2005); whereas the latter applies to the large scale yielding (LSY), which refers to conditions where fracture is accompanied by considerable plastic deformation (Anderson, 2005).

There are typically three modes of loading defined in fracture mechanics (Anderson, 2005), namely the opening mode or Mode I, the (in-plane) shear mode or Mode II and the tearing (out-of-plane shear) mode or Mode III, as illustrated in Fig. 1.1. The current study focuses on the Mode I loading because it is the most critical and representative fracture mode for pipelines.

For a given cracked isotropic linear elastic body subjected to external forces, if we define a polar coordinate system with the origin at the crack tip, as shown in Fig. 1.2, early studies (Westergaard, 1939; Irwin, 1957; Williams, 1957) showed that the stress field can be expressed as:

$$\sigma_{ij} = \frac{K}{\sqrt{2\pi r}} f_{ij}(\theta) + \sum_{m=0}^{\infty} A_m r^{m/2} g_{ij}^{(m)}(\theta) \tag{1.1}$$

where σ_{ij} (i, j = 1, 2 and 3) is the stress tensor; r and θ are coordinates defined in Fig. 1.2; f_{ij} is a dimensionless function of θ, and K is the so-called stress intensity factor in the unit

of force/area×(length)$^{0.5}$. For the higher-order terms, A_m is the amplitude and $g_{ij}^{(m)}$ is a dimensionless function of θ for the m^{th} term. As $r \rightarrow 0$, the leading term approaches infinity, but the higher-order terms remain finite or approach zero. Thus the stress field ahead of the crack tip can be written as:

$$\lim_{r \to 0} \sigma_{ij} = \frac{K}{\sqrt{2\pi r}} f_{ij}(\theta) \tag{1.2}$$

Equation (1.2) describes a stress singularity at the crack tip. The stress intensity factor, K, completely defines the amplitude of the stress singularity, which means that for a given K, the stresses, strains and displacements near the crack tip can be completely determined, and they are independent of the geometry of the cracked body and details of the loading (Hutchinson, 1983; Anderson, 2005).

The single-parameter characterization of the stress field near the crack tip relies on the satisfaction of the SSY condition, which requires the zone of plastic deformation to be sufficiently small compared with the crack length and other relevant geometric length quantities (Hutchinson, 1983). The size of the plastic zone ahead of the crack tip, r_p, can be approximately determined by (Hutchinson, 1983):

$$r_p = \frac{1}{\alpha\pi}\left(\frac{K}{\sigma_{YS}}\right)^2 \tag{1.3}$$

where α = 1 for the plane stress condition and α = 3 for the plane strain condition; σ_{YS} is the yield strength of the material. Because the stress field corresponding to the plane strain condition is more severe than that corresponding to the plane stress condition, for a given material at a given temperature, fracture can more easily occur for material under the plane strain condition. Therefore, for a material behaving in a linear elastic manner prior to unstable fracture, a critical point value of stress intensity factor under the Mode I loading and plane strain condition, denoted by K_{Ic}, is expected to be an appropriate fracture parameter of the material (Anderson, 2005; ASTM, 2012). To ensure the validity of the evaluated toughness value (i.e. the specimen being under SSY and the plane strain condition), the ASTM standard for experimentally determining the linear elastic plane strain fracture toughness of metallic materials, i.e. ASTM E399 (ASTM,

2012), requires the crack length, the length of the uncracked remaining ligament and the thickness of the test specimen to be no less than $2.5(K_{Ic}/\sigma_{YS})^2$ at the point of fracture.

Under the SSY condition, the energy release rate G, defined as the rate of decrease in the potential energy with a unit increase in the crack area (Irwin, 1957), can be related to the stress intensity factor K through the following relationship:

$$G = \frac{K^2}{E'} \tag{1.4}$$

For the plane stress condition, $E' = E$; for the plane strain condition, $E' = E/(1 - \nu^2)$, where E denotes the elastic modulus and ν is Poisson's ratio. Although the energy release rate describes global behavior and the stress intensity factor is a local parameter, Eq. (1.4) is proved to be adequate for all cracked configurations under the SSY condition (Anderson, 2005).

1.2.2 Elastic Plastic Fracture Mechanics

Linear elastic fracture mechanics (LEFM) is valid as long as nonlinear material deformation is confined to a relatively small region surrounding the crack tip (the SSY condition) (Anderson, 2005). For many ductile materials with medium-to-high toughness, it is virtually impossible to characterize the fracture behavior within LEFM, therefore an alternative approach, i.e. elastic-plastic fracture mechanics (EPFM), is required. Two commonly-used and most important EPFM parameters, i.e. J-integral and crack tip opening displacement (*CTOD*), developed primarily in the US and UK, respectively, are briefly introduced in this section.

The J-integral (J) concept was named by its inventor Dr. James R. Rice (1968) as a path-independent contour integral, which equals the decrease in the potential energy per unit increase in the crack area for nonlinear elastic cracked body, and equals G for a linear elastic cracked body. For a two-dimensional cracked body with an arbitrary counterclockwise contour (Γ) surrounding the crack tip as shown in Fig. 1.3, J is defined as the following contour integral with the unit of energy/area or equivalently force/length:

$$J = \int_{\Gamma} \left(w dy - T_i \frac{\partial u_i}{\partial x} ds \right) \tag{1.5}$$

where w denotes the strain energy density; T_i and u_i are the components of the traction and displacement vectors, respectively; ds is the length increment along the assigned contour Γ, as shown in Fig. 1.3. The mathematical proof of the path-independence of J-integral can be found in many fracture mechanics textbooks (e.g. Anderson, 2005). The strain energy density can be written as (Anderson, 2005):

$$w = \int_0^{\varepsilon_{ij}} \sigma_{ij} d\varepsilon_{ij} \tag{1.6}$$

where ε_{ij} is the strain tensor.

Hutchinson (1968) and Rice and Rosengren (1968) independently showed that due to its path-independence, J can also be used to characterize the crack tip condition in a non-linear elastic cracked body, similar to the stress intensity factor, K, in a linear elastic body. They adopted the following Ramberg-Osgood stress-strain relationship:

$$\frac{\varepsilon}{\varepsilon_0} = \frac{\sigma}{\sigma_0} + \alpha \left(\frac{\sigma}{\sigma_0} \right)^n \tag{1.7}$$

where σ_0 is the reference stress; ε_0 is the reference strain, $\varepsilon_0 = \sigma_0/E$; α is a dimensionless parameter, and n is commonly known as the strain hardening exponent of the material. For the region well within the plastic zone, close to the crack tip, the elastic strains are relatively small compared with the total strain. Therefore, Eq. (1.7) reduces to a simple power-law relationship, and the stresses and strains ahead the crack tip can be completely characterized by J through the following expressions, known as the HRR solutions (singularity):

$$\sigma_{ij} = \sigma_0 \left(\frac{J}{\alpha \sigma_0 \varepsilon_0 I_n r} \right)^{\frac{1}{n+1}} \tilde{\sigma}_{ij}(\theta, n) \tag{1.8}$$

$$\varepsilon_{ij} = \frac{\alpha \sigma_0}{E} \left(\frac{J}{\alpha \sigma_0 \varepsilon_0 I_n r} \right)^{\frac{n}{n+1}} \tilde{\varepsilon}_{ij}(\theta, n) \tag{1.9}$$

where I_n is an dimensionless constant depending on n and the stress state (plane stress or plane strain), and $\tilde{\sigma}_{ij}$ and $\tilde{\varepsilon}_{ij}$ are dimensionless functions of n, θ, and stress state. For linear elastic material, i.e. n = 1, Eq. (1.8) predicts $1/\sqrt{r}$ singularity, which is consistent with the LEFM theory. Therefore, J provides a single-parameter characterization of the crack-tip fields in EPFM, just as K in LEFM (see Eq. (1.2)), and the experimentally determined critical value of J at the onset of crack growth, known as J_{Ic}, can be used as the fracture toughness value of the material. For more ductile materials, J always increases with the small amount of crack advance; therefore, the *J-R* curve is commonly used as a characterization of the material toughness, as the *K*-based resistance curve for material under the SSY condition. The *J-R* curve has significant practical implications for engineering structures that are made of ductile materials and can tolerate certain amount of crack growth, because significant additional load carrying capacity can be achieved with the application of the *J-R* curve. The issues related to the experimental determination of the *J-R* curve for pipeline steels will be the main focus of the following chapters of this thesis.

The crack tip opening displacement (*CTOD*) is first proposed by Wells (1961) at the British Welding Institute as a measure of fracture toughness for high toughness materials, because it is found that for such kinds of materials, the sharp crack faces can move apart and becomes blunt due to the plastic deformation prior to fracture as illustrated in Fig. 1.4, and the degree of crack blunting increases in proportion to the toughness of the material (Anderson, 2005). Therefore, *CTOD* is found to be an appropriate parameter to characterize the crack tip states when K_{Ic} is not applicable and LEFM is no longer valid. Based on the strip-yield model analyzed by Burdekin and Stone (1966), the value of *CTOD* (δ) can be related to K or G in the limit of the SSY condition:

$$\delta = \frac{K^2}{m\sigma_{YS}E'} = \frac{G}{m\sigma_{YS}} \tag{1.10}$$

where m is a dimensionless constraint parameter that is approximately unity for the plane stress condition and 2 for the plane strain condition.

At present, there are two widely used definitions of *CTOD*, namely the displacement at the original crack tip and the 90 degree intercept definition, as illustrated in Figs. 1.4 (a) and (b), respectively. The first one was originally proposed by Well (1961), and the second definition was suggested by Rice (1968) and Shih (1981) and commonly used for the *CTOD* evaluation in the finite element analysis. If a semicircle (blunt) crack tip is assumed, these two definitions are essentially equivalent.

For linear elastic conditions, J is equivalent to the energy release rate G, and Eq. (1.10) can be written as follows in the limit of small scale yielding:

$$\delta = \frac{J}{m\sigma_{YS}} \tag{1.11}$$

where m = 1 for the plane stress condition. Under the stress state that is neither plane stress nor plane strain, the constraint parameter m usually has a value between 1 and 2 (Hollstein and Blauel, 1977). Equations (1.10) and (1.11), together with Eq. (1.4), demonstrate the equivalence of the fracture parameters (K, G, J and δ) under the linear elastic conditions. By comparing the displacements at the crack tip obtained from the HRR solutions and the elastic-plastic finite element analyses, Shih (1981) further showed that the linear relationship between *CTOD* and J, i.e. Eq. (1.11), applies well beyond the validity limits of LEFM, so that *CTOD* and J can be considered as equivalent fracture toughness parameters in EPFM. To consider the stain hardening effect, the yield stress, σ_{YS}, in Eq. (1.11) is commonly replaced by a so-called effective yield stress σ_Y defined as the average of σ_{YS} and the ultimate tensile stress σ_{TS}. Various expressions of the constraint constant m are developed for different specimen configurations through finite element analyses (Kirk and Wang, 1995; Wang et al., 1997; Panontin et al., 2000; Shen and Tyson, 2009; Ruggieri, 2012).

1.3 Objective and Research Significance

1.3.1 Investigation of the Effect of Crack Front Curvature on the Measurement of *J-R* Curve of Single-Edge Bend Specimens

The single-edge notched three-point bend (SE(B)) specimen is one of the commonly used standard small-scale specimens to experimentally determine the *J-R* curve. As specified in the test standards, e.g. ASTM 1820-11(ASTM, 2011), BS 7448-97 (BSI, 1997), all machine notched specimens need to be fatigue pre-cracked to simulate natural cracks before the *J-R* curve testing. The fatigue pre-cracking often introduces curved as opposed to straight crack fronts. The objective of the first study reported in this thesis (Chapters 2 and 3) was to investigate the impact of the specimen crack front curvature on the evaluated crack length and the J-integral values. Based on the analysis results, new crack front straightness criteria that are in most cases less stringent than the existing criteria specified in the relevant test standard, ASTM E1820-11, are recommended. The suggested criteria could potentially lead to reduced specimen rejection rates and cost savings.

1.3.2 Investigation of the Accuracy of the Double-Clip on Gauge Method for Evaluating *CTOD* of Single-Edge Tension Specimens

The objective of the second study reported in this thesis (Chapter 4) was to examine the accuracy of *CTOD* measured from the double-clip on gauge method based on a systematic 3D FEA of clamped single-edge tension (SE(T)) specimens. The analysis considers both plane-sided and side-grooved SE(T) specimens with ranges of crack lengths, thickness-to-width ratios and strain hardening characteristic of the material. Based on the analysis results, the existing equation for evaluating *CTOD* based on the double-clip on gauge method was slightly modified to improve the accuracy of the *CTOD* evaluation. This study will facilitate the application of the fracture toughness determined from the non-standard SE(T) specimen in the strain-based design of pipelines.

1.4 Thesis Format and Outline

This thesis is prepared in an integrated-article format as specified by the School of Graduate and Postdoctoral Studies at the University of Western Ontario and consists of five chapters. Each chapter, except Chapters 1 and 5, is presented in a manuscript format with its own list of notations and references.

Chapter 1 is the introduction of the entire thesis where a review of fundamentals of LEFM and EPFM, including the concepts of stress intensity factor, energy release rate, J-integral, *CTOD* and toughness resistance curve is presented. Chapter 2 investigates the effect of the specimen crack front curvature on the crack mouth opening displacement (*CMOD*)-based compliance and the crack length evaluation for the SE(B) specimen. The effect of the crack front curvature on the evaluation of J-integral for the SE(B) specimen is presented in Chapter 3. Chapter 4 examines the accuracy of the double-clip on gauge method for evaluating *CTOD* using the SE(T) specimen. Finally, Chapter 5 summarizes the concluding remarks of the thesis and provides recommendations for future studies.

References

Anderson, T. L. (2005). *Fracture Mechanics—Fundamentals and Applications, Third edition*. CRC Press, Boca Raton.

ASTM (2011). *ASTM E1820-11: Standard Test Method for Measurement of Fracture Toughness*. America Society of Testing and Materials International, West Conshohocken, PA.

ASTM (2012). *ASTM E399-12*: *Standard Test Method for Linear-Elastic Plane-Strain Fracture Toughness K_{Ic} of Metallic Materials*. America Society of Testing and Materials International, West Conshohocken, PA.

BSI (1997). *BS 7448: Fracture Mechanics Toughness Tests*. British Standard Institution, London.

Burdekin, F. M. and Stone, D. E. W. (1966). The Crack Opening Displacement Approach to Fracture Mechanics in Yielding Materials. *The Journal of Strain Analysis for Engineering Design*, 1(2), 145-153.

Fairchild, D. P., Kibey, S. A., Tang, H., Krishnan, V. R., Wang, X., Macia, M. L., and Cheng, W. (2012). Continued Advancements Regarding Capacity Prediction of Strain-based Pipelines. *Proceedings of 9th International Pipeline Conference (IPC2012)*, Calgary, Alberta, Canada, September 24–28.

Hollstein, T. and Blauel, J. G. (1977). On the Relation of the Crack Opening Displacement to the J-integral, *International Journal of Fracture*, 13, 385-390.

Hutchinson, J. W. (1968). Singular Behavior at the End of a Tensile Crack in a Hardening Material. *Journal of the Mechanics of Physics and Solids*, 16, 13-31.

Hutchinson, J. W. (1983). Fundamentals of the Phenomenological Theory of Nonlinear Fracture Mechanics. *Journal of Applied Mechanics*, 50, 1042-1051.

Irwin, G. R. (1957). Analysis of Stresses and Strains Near the End of a Crack Traversing a Plate. *Journal of Applied Mechincs*, 24, 361-364.

Kirk, M. T. and Wang, Y. Y. (1995). Wide Range CTOD Estimation Formulae for SE(B) Specimens. *Fatigue and Fracture Mechanics, ASTM STP 1256*, American Society for Testing and Materials, 26, 126-141.

National Energy Board (NEB), (2012). *Annual Report 2012 to Parliament*, National Energy Board, Canada.

Panontin, T. L., Makino, A. and Williams, J. F. (2000). Crack Tip Opening Displacement Estimation Formulae for C(T) Specimens. *Engineering Fracture Mechanics*, 67, 293-301.

Rice, J. R. (1968). A Path Independent Integral and the Approximate Analysis of Strain Concentration by Notches and Cracks. *Journal of Applied Mechanics*, 35, 379-86.

Rice, J. R. and Rosengren, G. F. (1968). Plane Strain Deformation Near a Crack Tip in a Power Law Hardening Material. *Journal of the Mechanics of Physics and Solids*, 16, 1-12.

Ruggieri, C. (2012). Further Results in J and CTOD Estimation Procedures for SE (T) Fracture Specimens–Part I: Homogeneous Materials. *Engineering Fracture Mechanics*, 79, 245-265.

Shen, G., and Tyson, W. R. (2009). Evaluation of CTOD from J-integral for SE(T) Specimens. *Pipeline Technology Conference*, Ostend, Belgium, October 12-14.

Shih, C. F. (1981). Relationships between the J-integral and the Crack Opening Displacement for Stationary and Extending Cracks. *Journal of the Mechanics and Physics of Solids*, 29(4), 305-326.

Wang, Y. Y., Reemsnyder, H. S. and Kirk, M. T. (1997). Inference Equations for Fracture Toughness Testing: Numerical Analysis and Experimental Verification. *Fatigue and Fracture Mechanics, ASTM STP 1321*, American Society for Testing and Materials, 28, 469-484.

Wells, A. A. (1961). Unstable Crack Propagation in Metals, Cleavage and Fast Fracture. *Proceedings of the Crack Propagation Symposium*, Cranfield, UK, 1, 84.

Westergaard, H. M. (1939). Bearing Pressures and Cracks. *Journal of Applied Mechanics*, 6, 49-53.

Williams, M. L. (1957). On the Stress Distribution at the Base of a Stationary Crack. *Journal of Applied Mechincs*, 24, 109-114.

Zhu, X. K. and Joyce, J. A. (2012). Review of Fracture Toughness (G, K, J, CTOD, CTOA) Testing and Standardization. *Engineering Fracture Mechanics*, 85, 1-46.

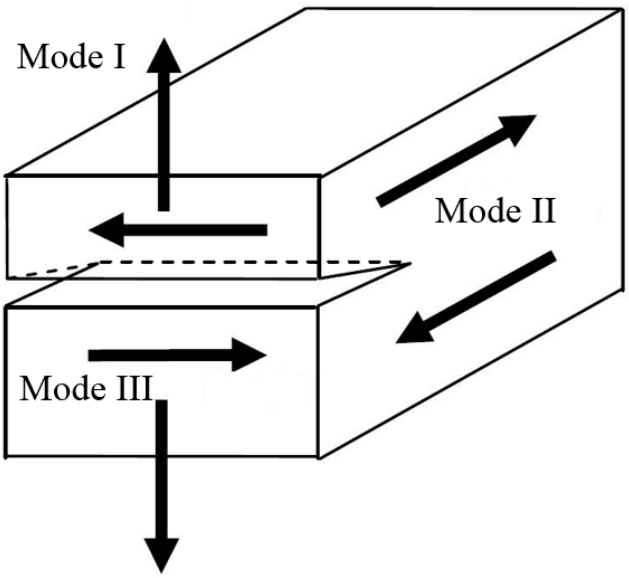

Figure 1.1. Three typical loading modes in fracture mechanics

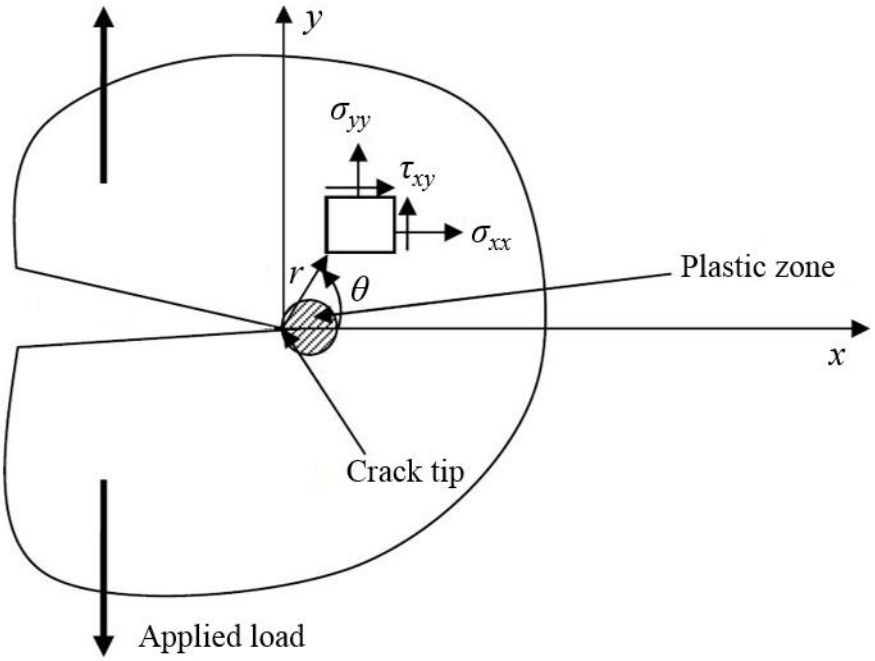

Figure 1.2. Stress field solutions surrounding the crack tip

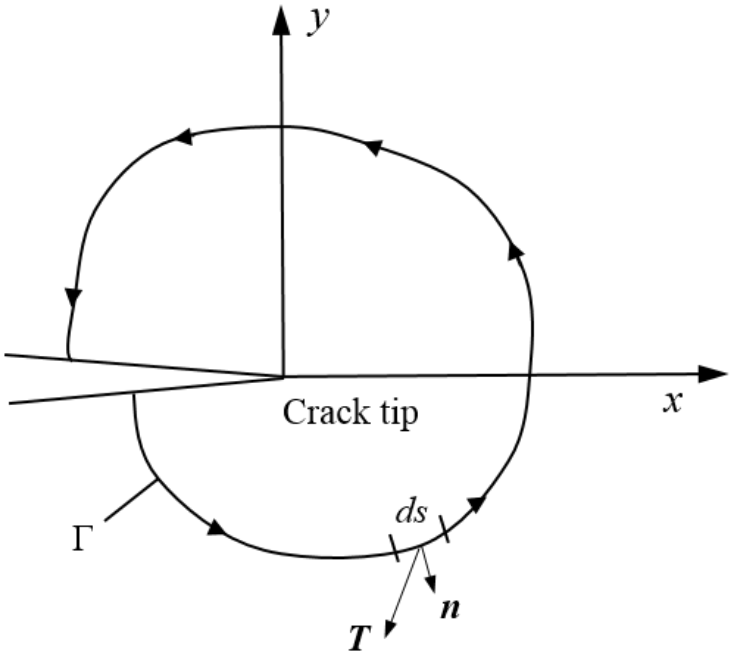

Figure 1.3. Arbitrary contour around the crack tip

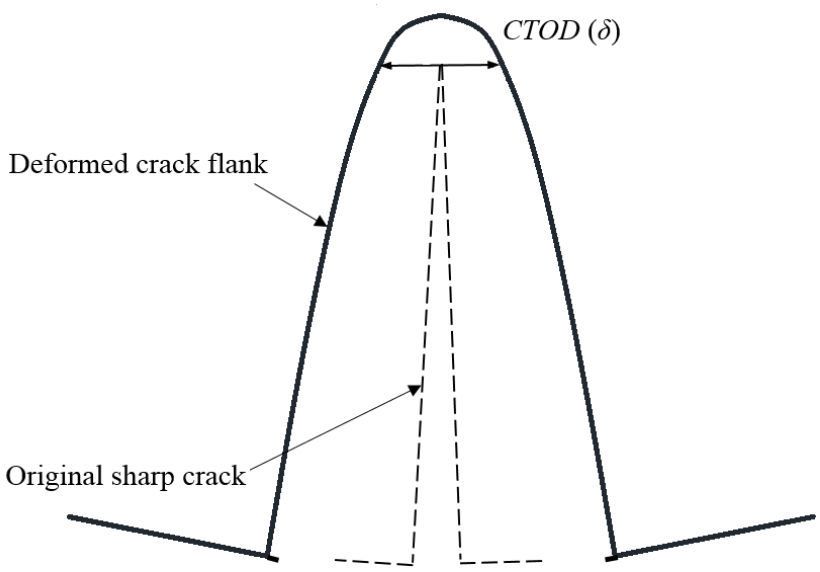

(a) Displacement at the original crack tip

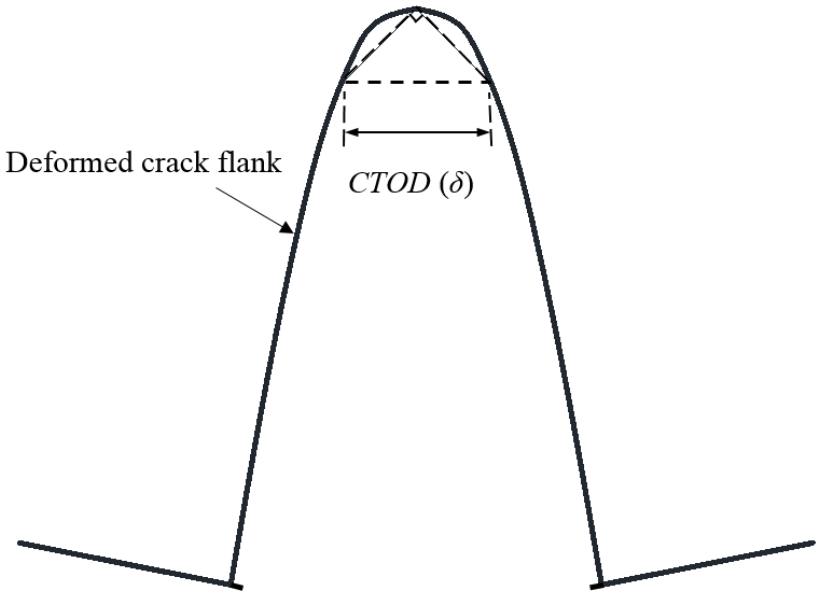

(a) Displacement at the intersection of a 90 degree vertex with the crack flanks

Figure 1.4. Schematically illustration of *CTOD* definitions

Chapter 2 Effect of Crack Front Curvature on *CMOD* Compliance and Crack Length Evaluation for Single-edge Bend Specimens

2.1 Introduction

2.1.1 Fracture Toughness Resistance Curve Tests on Small-scale Specimens

The fracture toughness resistance curve of ductile materials, such as the J-integral (J) or crack tip opening displacement ($CTOD$) resistance curve, is an important input of the integrity assessment and strain-based design of energy pipelines containing planar defects (i.e. cracks). There are two main components of the fracture toughness resistance curves (i.e. *J-R* or *CTOD-R* curves), namely the crack growth, Δa, and the toughness value (J or $CTOD$) corresponding to the crack growth.

The *J-R* or *CTOD-R* curves are commonly measured on small-scale specimens, e.g. three-point single-edge bend (SE(B)), compact tension (C(T)) and single-edge tension (SE(T)) specimens. The configurations of typical SE(B), C(T) and SE(T) specimens as well as the difference between the plane-sided and side-grooved specimens are schematically shown in Fig. 2.1, where a, B, B_N, H, S and W denote the crack length, specimen thickness, net thickness for side-grooved specimens, daylight length, specimen span and specimen width, respectively. SE(B) and C(T) specimens have been standardized in test standards such as ASTM E1820-11 (ASTM, 2011) and BS 7448 (BSI, 1991). During the *J-* and *CTOD-R* curve test, a displacement controlled load (P) is applied to the specimen as illustrated in Figs. 2.1(b) to (d), and the corresponding load line displacement (LLD) and crack mouth opening displacement ($CMOD$) can be measured by the test machine and clip-on gauge instrumented at the crack mouth, respectively. Figure 2.1 (f) shows the real test set-up for the single-edge bend (SE(B)) and the clamped single-edge tension (SE(T)) specimens. The obtained *P-LLD* or *P-CMOD* curves are the key input to the experimental evaluation of the *J-R* or *CTOD-R* curves based on these specimens. The evaluation of the J value for the SE(B) specimen and the $CTOD$ value for the SE(T) specimen are discussed in Chapters 3 and 4, respectively.

The elastic unloading compliance method (Clarke et al., 1976) is widely used to experimentally determine the fracture toughness resistance curve from a single test specimen. In this method, a series of partial unloading and reloading sequences are conducted on the specimen during the test as illustrated in Fig. 2.2. At load step *i*, the slope of the corresponding unloading line was evaluated to obtain the measured compliance of the specimen, C_i (i.e. the inverse of the specimen stiffness). The instantaneous crack length can then be estimated from the corresponding compliance through the crack length-compliance equation. Although the compliance of the specimen can be determined based on either *LLD* or *CMOD*, the latter is usually preferred over the former because *CMOD* can be more easily and accurately measured than *LLD* during tests (Zhu et al., 2008).

2.1.2 Literature Review and Objective

As specified in ASTM E1820-11 (ASTM, 2011), all machine notched specimens need to be fatigue pre-cracked to simulate natural cracks before the resistance curve testing. The fatigue pre-cracking often introduces curved as opposed to straight crack fronts, as illustrated in Fig. 2.3. The shape of the curved initial crack front is largely affected by specimen dimensions, notch machining conditions, fatigue pre-cracking conditions and residual stress distributions (Zhou and Soboyejo, 2002). Furthermore, the crack growth during the test is in general non-uniform across the crack front. The crack generally grows faster at the mid-plane as a result of the high local stress triaxiality, and grows slower near the free surfaces due to the near plane stress conditions (Zhou and Soboyejo, 2002).

Steenkamp (1985) investigated the influence of the crack front curvature on the specimen compliance using two-dimensional (2D) plane strain finite element analyses for SE(B) specimens with the same average crack length but different crack front curvatures. He concluded that for the same average crack length by increasing the crack front curvature, the *CMOD* compliance would decrease, and for the same crack front curvature, the effect of curvature on the compliance became more pronounced as the average crack length increases. Many crack length-compliance equations for various

specimens have been reported in the literature (e.g. Tada et al., 1973; Saxena and Hudak, 1978; Wu, 1984; Joyce, 1992). However, these equations were all developed based on specimens with straight crack fronts. Applying such equations to specimens with curved crack fronts will inevitably lead to errors in the predicted crack length. Therefore, the main objective of the study reported in this chapter was to quantify the crack front curvature-induced error in the crack length predicted from the crack length-compliance equation. The focus of the study was on the *CMOD* compliance of the plane-sided SE(B) specimen because 1) the SE(B) specimen is widely used in the resistance curve testing; 2) the crack fronts in the plane-sided specimens are typically more curved than those in the side-grooved specimens (Zhou and Soboyejo, 2002; Park et al., 2011), and 3) *CMOD* is the preferred deformation measurement than *LLD*.

ASTM E1820-11 (ASTM, 2011) specifies the allowable deviation of a curved crack front from a straight front based on the so-called nine-point measurement method (see Section 2.2). It requires that none of the nine physical measurements of the initial (final) crack size differ by more than $0.05B$ from the average initial (final) crack length a_{ave} obtained from the nine measurements. Test specimens that do not meet this criterion are deemed unacceptable and therefore rejected. In this regard, the other objective of the present study was to examine if the crack front straightness criterion in ASTM E1820-11 is adequate to ensure the accuracy of the predicted crack lengths for SE(B) specimens with curved crack fronts.

2.1.3 Approach

Linear elastic three-dimensional (3D) finite element analyses of plane-sided SE(B) specimens with a wide range of thickness-to-width ratios, average crack lengths and crack front curvatures were carried out to evaluate the elastic compliance of the specimens. For a given specimen with either a straight or curved crack front, the crack length predicted from the *CMOD* compliance was compared with its actual average crack length to quantify the curvature-induced error in the predicted crack length. The impact of the equivalent elastic modulus corresponding to the plane stress or plane strain

condition used in the crack length-compliance equation on the accuracy of the predicted crack length was also investigated.

The rest of this chapter is organized as follows. Section 2.2 describes the characteristics of the curved crack front as reported in the literature as well as reflected in the actual crack front data; the 3D FEA models and analysis procedures are described in Section 2.3; Section 2.4 presents the analysis results and discussions; the summary and concluding remarks of this chapter are included in Section 2.5.

2.2 Characteristics of Curved Crack Front

Previous experimental studies (Towers, 1983; Nikishkov et al., 1999; Zhou and Soboyejo, 2002; Park et al., 2011; Wang et al., 2012) showed that curved crack fronts are typically bowed and symmetric about the mid-plane of the specimen. Figure 2.4 photographically shows the machined notches, fatigue pre-crack fronts and final crack fronts for three plane-sided specimens (one SE(B) and two SE(T) specimens) fabricated and tested in the Department of Civil and Environmental Engineering at Western. The figure shows that the pre-crack and final crack fronts are all bowed and approximately symmetric with respect to the mid-plane, consistent with the observations reported in the literature. Therefore, only symmetric bowed crack fronts were considered in this study.

The following power-law expression was proposed by Nikishkov et al. (1999) to characterize a typical symmetric bowed crack front (see Fig. 2.3):

$$a(x) = a(0) - \beta W \left(\frac{abs(x)}{B/2}\right)^p \tag{2.1}$$

where x is the coordinate in the specimen thickness direction varying from $-B/2$ to $B/2$; $a(x)$ is the crack length as a function of x; $a(0)$ and $a(\pm B/2)$ denote the crack lengths at the mid-plane and free surfaces of the specimen, respectively; $\beta = a(0)/W - a(B/2)/W$, and p ($p > 1$) is a shape parameter. For a symmetric bowed crack front such as shown in Fig. 2.3, β is equal to $a_{max}/W - a_{min}/W$. It follows from Eq. (2.1) that both β and p influence the crack front curvature, albeit in different ways: β is a linear scaling factor to the

curvature over the entire crack front, whereas the effect of p on the curvature depends on the value of x.

By examining the fatigue pre-crack fronts of a total of 110 C(T) test specimens with different specimen thicknesses but the same thickness-to-width ratio (B/W = 0.5), Nikishkov et al. (1999) pointed out that the shape parameter p in Eq. (2.1) is insensitive to the specimen thickness and can be assigned a fixed value of 3.0. In this study, we examined the crack fronts in eight SE(B) and nine single-edge tension (SE(T)) specimens tested and reported by Park et al. (2011) and Wang et al. (2012). Details of these specimens are summarized in Table 2.1. Although the focus of this study is plane-sided SE(B) specimens, the fatigue pre-crack fronts of both the SE(B) and SE(T) specimens were included because the fatigue pre-cracking procedure for the two types of specimen is the same. The pre-crack fronts of both the plane-sided and side-grooved specimens were considered because side grooves are fabricated after the pre-cracking and therefore have no impact on the shape of the pre-crack front. However, only the final crack fronts of plane-sided SE(B) specimens were included to examine the applicability of Eq. (2.1).

The crack fronts of the collected specimens were digitized and then curve-fitted using Eq. (2.1). It is observed that Eq. (2.1) fits the actual crack fronts fairly well for all the specimens considered. A comparison of the actual and fitted crack fronts for two selected specimens, i.e. SE(B)-1 and SE(T)-1 (the first two in Fig. 2.4), is depicted in Fig. 2.5 for illustration. The values of β and p associated with the fitted crack fronts are summarized in Table 2.1. The average value of p for all pre-crack fronts is 3.09, which is consistent with Nikishkov et al.'s (1999) suggestion that p be assigned a fixed value of 3.0. Given the above, Eq. (2.1) was adopted to characterize the curved crack front in the present study. A wide range of values of β were assumed in the study, whereas p was set to equal 3.0 for the majority of the analysis cases. Sensitivity analyses were carried out for several cases with p = 2.5. The rationale for selecting p = 2.5, as opposed to, say, p = 3.5, in the sensitivity analysis is that for a given β the central portion of the crack front becomes more curved as p decreases (see Fig. 2.6 for an illustration). A relatively small value of p was therefore selected for the sensitivity analysis.

Because we investigated the impact of the crack front curvature on the *CMOD* compliance and the evaluated crack length based on the same average crack length but different crack front curvatures, Eq. (2.1) was recast in terms of the average crack length, a_{ave}, instead of the crack length at the mid-plane, $a(0)$. Furthermore, the value of a_{ave} was calculated in accordance with the nine-point measurement method specified in ASTM E1820-11 (ASTM, 2011). The measurements should be made at nine equally spaced points centered about the mid-plane of the specimen (see Fig. 2.3). The two points farthest from the mid-plane are located at $0.005W$ from the free surfaces. The value of a_{ave} is then obtained as follows:

$$a_{ave} = \frac{1}{8}\left(\frac{a_1+a_9}{2} + \sum_{i=2}^{i=8} a_i\right) \tag{2.2}$$

where a_i (i = 1, 2, …, 9) denote the crack lengths at the nine measurement points, with a_1 and a_9 being the measured crack lengths at the two points farthest from the mid-plane (see Fig. 2.3).

If the crack front is characterized by Eq. (2.1), a_i is then given by:

$$a_i = a(0) - \beta W\left[abs(i-5)\cdot\left(0.25 - \frac{\Delta}{2B}\right)\right]^p (i = 1, 2, \ldots, 9) \tag{2.3}$$

where Δ is the distance between the outmost measure point and the specimen free surface specified in test standards. For ASTM E1820-11, $\Delta = 0.005W$.

By substituting Eq. (2.3) into Eq. (2.2) and Eq. (2.1), and then considering $a_1 = a_9$ due to symmetry, Eq. (2.1) can be recast into the following format:

$$a(x) = a_{ave} + \beta W\left\{\left(0.25 - \frac{\Delta}{2B}\right)^p \cdot \frac{1}{8}\sum_{i=1}^{i=8}[abs(i-5)]^p - \left(\frac{abs(x)}{B/2}\right)^p\right\} \tag{2.4}$$

Equation (2.4) completely defines a curved crack front given the average crack length a_{ave} obtained from the nine-point measurement method, and the two parameters β and p.

To put Eq. (2.4) in the context of the crack front straightness criterion specified in ASTM E1820-11, a parameter λ, $\lambda = \max(a_{max9} - a_{ave}, a_{ave} - a_{min9})/B$, was introduced, where a_{max9} and a_{min9} are the maximum and minimum values of the nine physical

measurements, respectively. Note that a straight crack front corresponds to λ = 0; the crack front curvature increases with λ, and λ = 0.05 corresponds to the maximum allowable crack front curvature as specified in ASTM E1820-11. For specimens with symmetric bowed crack fronts, the values of β and λ are uniquely related as follows (see Appendix A for the derivation):

$$\beta = \frac{\lambda}{\left(\frac{W}{B}\right)\left(0.25-\frac{\Delta}{2B}\right)^{p}\left[4^{p}-\frac{1}{8}\sum_{i=1}^{i=8}[abs(i-5)]^{p}\right]} \tag{2.5}$$

Then for given a_{ave}/W, B/W and p (p > 1), crack fronts with different curvatures can be generated from Eq. (2.4) and Eq. (2.5) by varying λ.

2.3 Finite Element Analyses

The commercial software package ADINA 8.7.4 (ADINA, 2012) was used to carry out 3D linear elastic finite element analyses (FEA) to evaluate the *CMOD* compliance of SE(B) specimens. All the SE(B) specimens considered in this study are plane-sided, and have the same width and the standard span-to-width ratio (S/W = 4), but three different relative average crack lengths a_{ave}/W (i.e. a_{ave}/W = 0.3, 0.5 and 0.7) and three different specimen thicknesses (i.e. B/W = 1, 0.5 and 0.25) that are consistent with the range of B/W ratios suggested in ASTM E1820-11 (ASTM, 2011). Specimens with straight and curved crack fronts were considered. For specimens with curved crack fronts, the crack front is characterized by Eq. (2.4) and Eq. (2.5) with p = 3 and λ = 0.01 to 0.10 with an increment of 0.01. In addition, specimens with curved crack fronts characterized by p = 2.5 and selected geometric configurations (i.e. B/W = 0.5, a_{ave}/W = 0.3, 0.5 and 0.7) were also considered to investigate the impact of the shape parameter p on the compliance and accuracy of the crack length predicted from the compliance.

Because of symmetry, only a quarter of the specimen was modeled. The geometric and mesh configurations for a typical specimen are shown in Fig. 2.7 together with the fixation and loading conditions. The model was divided into ten layers in the thickness direction with the mesh density increasing from the mid-plane to the free surface to capture the high stress gradients near the free surface. In the vicinity of the crack tip, the

smallest element has dimensions of about 1/3000W and 1/75B in the width and thickness directions, respectively. The aspect ratio of the elements is less than 7. There are about 11,000 20-node 3D isoparametric brick elements (ADINA, 2012) included in a typical model. Young's modulus and Poisson's ratio were set to be 200 GPa and 0.3, respectively.

The load was applied based on a displacement-controlled condition. The *CMOD* of the specimens included in FEA was obtained at the mid-plane. The calculated *CMOD* compliance, i.e. $C = CMOD/P$, for a representative specimen was observed to be independent of the magnitude of the applied displacement within the range of 0.001 to 0.1 mm. Therefore, the compliance was evaluated corresponding to the applied displacement of 0.1mm (*LLD* = 0.1mm) for all the specimens included.

2.4 Analysis and Discussions

2.4.1 Effect of the Crack Front Curvature on *CMOD* compliance

For a given specimen with a curved crack front, the *CMOD* compliance value, C_c, was compared with the compliance, C_s, of the specimen with a straight crack front and the same a_{ave}/W and B/W ratios as the specimen with the curved crack front. The values of C_c/C_s are plotted against λ for specimens with curved or straight crack fronts in Figs. 2.8(a) through 2.8(c). All the specimens with curved crack fronts shown in Fig. 2.8 have the same shape parameter $p = 3$. The figures suggest that given a_{ave}/W and B/W, as λ increases from 0 to 0.1, the ratio of C_c/C_s first increases slightly reaching a peak point at around $\lambda = 0.03$ to 0.05, and then decreases as λ further increases. After that peak point, the effect of the crack front curvature on the compliance becomes more pronounced as the crack length increases. Due to the dependence of the ASTM E1820-11 straightness criteria on the specimen thickness, i.e. λ being a function of B, for specimens with the same average crack length and λ values, the crack front curvature impacts the compliance of thick specimens more than that of thin specimens as shown in Fig. 2.8. For specimens with $B/W = 1$ and all the λ values considered in this study, the C_c/C_s ratio ranges from 0.94 to 1.01; for $B/W = 0.5$, C_c only differs from C_s by less than 2%, and for $B/W = 0.25$, C_c differs from C_s by less than 1%. The differences between C_c and C_s corresponding to

λ = 0.05 (the maximum allowable crack front curvature as specified in ASTM E1820-11) are within 1% for all the specimen configurations considered in this study. These results suggest that the crack front curvature has a negligible impact on the *CMOD* compliance for $\lambda \leq 0.05$.

2.4.2 Crack Length - *COMD* Compliance Equations

The relationship between the *CMOD* compliance, *C*, and the relative crack length *a/W* is usually derived from numerical studies (Tada et al., 1973; Wang et al., 2013). The following expression that evaluates *C* corresponding to a given *a/W* proposed by Tada et al. (1973) is widely used for SE(B) specimens:

$$\frac{4BCE'}{S/W} = f\left(\frac{a}{W}\right) = 24\left(\frac{a}{W}\right)\left[0.76 - 2.28\left(\frac{a}{W}\right) + 3.87\left(\frac{a}{W}\right)^2 - 2.04\left(\frac{a}{W}\right)^3 + \frac{0.66}{\left(1-\frac{a}{W}\right)^2}\right] \quad (2.6)$$

where *E*' is the elastic modulus corresponding to the plane strain condition, i.e. $E' = E/(1 - \nu^2)$. Equation (2.6) was reported to be accurate within 1% for all *a/W* values (Joyce, 1992).

By inverting Eq. (2.6), Wu (1984) and Joyce (1992) developed Eqs. (2.7) and (2.8), respectively, to evaluate *a/W* from the *CMOD* compliance for SE(B) specimens:

$$a/W = 0.999748 - 3.950u + 2.9821u^2 - 3.21408u^3 + 51.5156u^4 - 113.031u^5 \quad (2.7)$$

$$a/W = 1.01878 - 4.5367u + 9.0101u^2 - 27.333u^3 + 74.400u^4 - 71.489u^5 \quad (2.8)$$

where $u = \frac{1}{\left(\frac{4BCE'}{S/W}\right)^{1/2}+1}$.

Equations (2.7) and (2.8) have been adopted in ASTM E1820-11 (with *E'* replaced by *E*) to evaluate the crack length for deeply-cracked ($0.45 \leq a/W < 1$) and shallow-cracked ($0.05 \leq a/W < 0.45$) SE(B) specimens, respectively.

Because the actual stress state in the remaining ligament of a 3D specimen is neither plane stress nor plane strain (Steenkamp, 1985; Shen et al., 2012), the use of either *E* or

E' in Eqs. (2.7) and (2.8) will impact the accuracy of the calculated *a/W* values. Therefore, the following so-called effective modulus of elasticity, E_e, was proposed by Wang et al. (2013) to be used in Eqs. (2.7) and (2.8) to improve the accuracy of the calculated *a/W* values:

$$E_e = (A_0 + A_1 u + A_2 u^2 + A_3 u^3 + A_4 u^4)E \tag{2.9}$$

where A_0, A_1, A_2, A_3 and A_4 are empirical coefficients and listed in Table 2.2. It is noted that Eqs. (2.6) to (2.9) are all developed based on specimens with straight crack fronts.

2.4.3 Effect of the Crack Front Curvature on the Evaluated Crack Length

In the present study, all three above-mentioned elastic moduli, i.e. *E*, *E'* and E_e, were used in Eqs. (2.7) and (2.8) to predict the average crack length (denoted as a_p) for specimens containing curved or straight crack fronts from the *CMOD* compliance obtained from FEA. Consistent with ASTM E1820-11, Eq. (2.7) was employed for specimens with *a/W* = 0.5 and 0.7, whereas Eq. (2.8) was used for specimens with *a/W* = 0.3. Note that for specimens with curved crack fronts, the predicted crack length a_p can be considered as the equivalent crack length corresponding to a straight crack front, which is generally not the same as the nine point measured average crack length a_{ave} even if Eqs. (2.7) and (2.8) are perfectly accurate. The error in the predicted crack length, e_a, was calculated as $e_a = (a_p - a_{ave})/a_{ave}$. The values of e_a are plotted against λ in Figs. 2.9(a) to 2.9(i). It is observed that the magnitude of e_a is governed by the choice of the elastic moduli, and insensitive to the crack front curvature regardless of the a_{ave}/W and *B/W* ratios. Except for specimens with $a_{ave}/W = 0.7$ and *B/W* = 1, the use of *E* leads to more accurate predictions of a_{ave} than the use of *E*'. The magnitude of e_a corresponding to the use of *E* is within 1% for specimens with *B/W* = 0.5 and 0.25, and 3% for specimens with *B/W* = 1. The magnitude of e_a corresponding to the use of *E*' is between 1% and 7%. Furthermore, the use of E_e leads to the most accurate prediction of a_{ave} with the magnitude of e_a being less than 1% for all the specimens considered.

The impact of the shape parameter *p* involved in Eq. (2.4) on e_a was investigated based on SE(B) specimens with a_{ave}/W = 0.3, 0.5 and 0.7, *B/W* = 0.5 and λ = 0 to 0.10.

The values of e_a corresponding to p = 3 and 2.5 for the specimens considered are depicted in Figs. 2.9(d), 2.9(e) and 2.9(f). The results shown in these figures indicate that p has a negligible impact on e_a.

2.5 Summary and Concluding Remarks

Three-dimensional linear-elastic FEA was performed on plane-sided SE(B) specimens with straight and curved crack fronts to investigate the impact of the crack front curvature on the *CMOD* compliance and accuracy of the crack length predicted from the crack length-*CMOD* compliance equations proposed by Wu (1984) and Joyce (1992). The set of specimens analyzed have three a_{ave}/W values (a_{ave}/W = 0.3, 0.5 and 0.7) and three B/W ratios (B/W = 1, 0.5 and 0.25). Symmetric bowed crack fronts with different curvatures were considered in the analysis. The power-law expression proposed by Nikishkov et al. (1999) was adopted to characterize the curved crack front but was recast by introducing a crack front curvature parameter λ that is consistent with the crack front straightness criterion specified in ASTM E1820-11. The *CMOD* compliance of the specimen with a curved crack front was compared with the compliance of the specimen with a straight crack front and the same average crack length and thickness. For a given specimen with either a straight or curved crack front, the crack length predicted from Wu's or Joyce's equation was compared with its actual average crack length to quantify the error in the predicted crack length.

The numerical results show that for SE(B) specimens with curved crack fronts satisfying the straightness criterion as specified in ASTM E1820-11, i.e. $\lambda \leq 0.05$, the corresponding *CMOD* compliance differs by less than 1% compared with the compliance of the specimen with the straight crack fronts and the same average crack length. In addition, the crack front curvature has a negligible impact on the accuracy of the crack length predicted from Wu's or Joyce's equation for λ values ranging from 0.01 to 0.10 regardless of a_{ave}/W and B/W ratios.

The use of three different elastic moduli, i.e. E, E' and E_e, in the prediction of the average crack length for SE(B) specimens with curved crack fronts was investigated. It is observed that the use of E_e as proposed by Wang et al. (2013) can lead to highly

accurate prediction of the average crack length (with the maximum error of prediction of 1%) for a wide range of *a/W*, *B/W* and crack front curvatures.

References

ADINA (2012). *Theory and Modeling Guide*. ADINA R & D Inc., Watertown, MA.

ASTM (2011). *ASTM E1820-11: Standard Test Method for Measurement of Fracture Toughness*. America Society of Testing and Materials International, West Conshohocken, PA.

BSI (1991). *BS 7448: Fracture Mechanics Toughness Tests*. British Standard Institution, London.

Clarke, G. A., Andrews, W. R., Paris, P. C., Schmidt, D. W. (1976). Single Specimen Tests for JIc Determination. *Mechanics of Crack Growth*, ASTM STP 590, American Society for Testing and Materials, Philadelphia, 27-42.

Joyce J. A. (1992). J-resistance Curve Testing of Short Crack Bend Specimens Using Unloading Compliance, *Fracture Mechanics*, *Proceedings of the 22nd National Symposium*, 1, 904-924.

Nikishkov, G. P., Heerens, J., and Hellmann, D. (1999). Effect of Crack Front Curvature and Side Grooving on CTOD δ5 and J-Integral in CT and 3PB Specimens. *Journal of Testing and Evaluation*, 27(5), 312–319.

Park, D. Y., Tyson, W. R., Gianetto, J. A., Shen, G., Eagleson, R. S., Lucon, E. and Weeks, T. S.(2011). Small-Scale Low-Constraint Fracture Toughness Test Results. CANMET Report No. 2010-28(TR), CANMET Materials Technology Lab, Hamilton, Ontario, Canada.

Saxena, A. and Hudak, S. J. (1978). Review and Extension of Compliance Information for Common Crack Growth Specimens. *International Journal of Fracture,*14(5), 453-68.

Steenkamp P. (1985). JR-curve Testing of Three-point Bend Specimen by the Unloading Compliance Method. *Fracture Mechanics 18th Symposium*, ASTM STP 945, 583-610.

Shen, G., Tyson, W. R. and Gianetto, J. A. (2010). CMOD Compliance of BxB Single Edge Bend Specimens. *Proceedings of the 2012 ASME Pressure Vessel and Piping Division Conference*, Toronto, Ontario, Canada, July 15–19, ASME, New York.

Tada, H., Paris, P. C. and Irwin, G. R. (1973). *The Stress Analysis of Cracks Handbook*. Del Research Corporation, Hellertown, PA.

Towers, O. L. (1983). Fatigue Crack Front Shape and Its Effect on Fracture Toughness Measurements. *Journal of Testing and Evaluation*, 11(1), 34-45.

Wang E., Zhou, W., Shen, G., and Duan, D. (2012). An Experimental Study on J(CTOD)-R Curves of Single Edge Tension Specimens for X80 Steel. *International Pipeline Conference (IPC2012)*, Calgary, Alberta, Canada, September 24–28, Paper Number: IPC2012-90323.

Wang E., Zhou, W. and Shen, G. (2013). A Numerical Study on Effective Modulus of Elasticity in Crack Length Evaluation for Single-edge Bending Specimens. *Journal of Testing and Evaluation*, 41(5), 1-8, doi: 10.1520/JTE20120269.

Wu, S. X. (1984). Crack Length Calculation Formula for Three Point Bend Specimens. *International Journal of Fracture*, 24(1), R33-R38.

Zhou, J., and Soboyejo, W. O. (2002). An Investigation of the Effects of Crack Front Curvature on the Crack-tip Opening Displacement of A707 steel. *International Journal of Fracture*, 115(3), 287-305.

Zhu, X. K., Leis, B. N., and Joyce, J. A. (2008). Experimental Estimation of J-R Curves From Load-CMOD Record for SE(B) Specimens. *Journal of ASTM International*, 5, 231–245.

Table 2.1: Summary of the curved crack fronts of the specimens collected in this study

Specimen ID	Side surfaces[1]	Examined crack front	Fitted parameters			Source
			$a(0)$	β	p	
SE(B)-1	PS	Fatigue pre-crack front	0.50	0.06	2.80	Wang et al. (2012)
		Final crack front	0.55	0.08	3.71	
SE(B)-2	SG	Fatigue pre-crack front	0.32	0.02	2.58	Park et al. (2011)
SE(B)-3	SG		0.22	0.04	3.41	
SE(B)-4	SG		0.22	0.04	3.27	
SE(B)-5	SG		0.22	0.04	2.33	
SE(B)-6	SG		0.23	0.04	2.87	
SE(B)-7	SG		0.22	0.04	2.60	
SE(B)-8	SG		0.33	0.00	4.54	
SE(T)-1	PS		0.54	0.05	3.42	Wang et al. (2012)
SE(T)-2	PS		0.54	0.04	3.41	
SE(T)-3	SG		0.15	0.01	2.09	Park et al. (2011)
SE(T)-4	SG		0.33	0.01	2.25	
SE(T)-5	SG		0.32	0.01	3.28	
SE(T)-6	SG		0.31	0.00	3.71	
SE(T)-7	SG		0.34	0.01	3.69	
SE(T)-8	SG		0.15	0.01	2.98	
SE(T)-9	SG		0.33	0.01	3.22	

Notes:

1. PS: Plane-sided specimen; SG: Side-grooved specimen. All the specimens collected in this study have the same thickness-to-width ratio ($B/W = 1$).

Table 2.2: The coefficients used in Eq. (2.9)

B/W	A_0	A_1	A_2	A_3	A_4
1	1.0773	0.2685	-6.9063	28.9474	-32.3795
0.5	1.0698	-0.0709	-4.7352	22.4058	-24.9463
0.25	1.0414	-0.0706	-2.7256	12.2094	-12.147

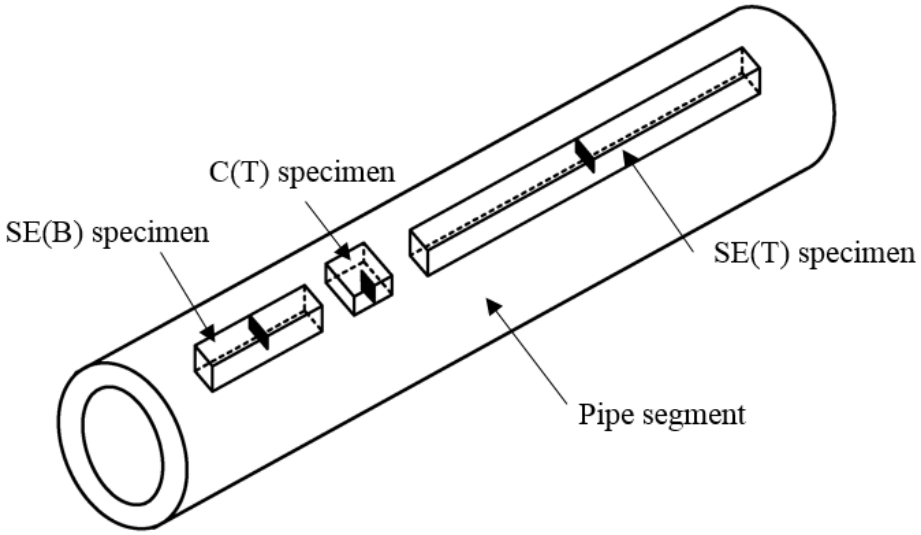

(a) Schematic of small-scale specimens

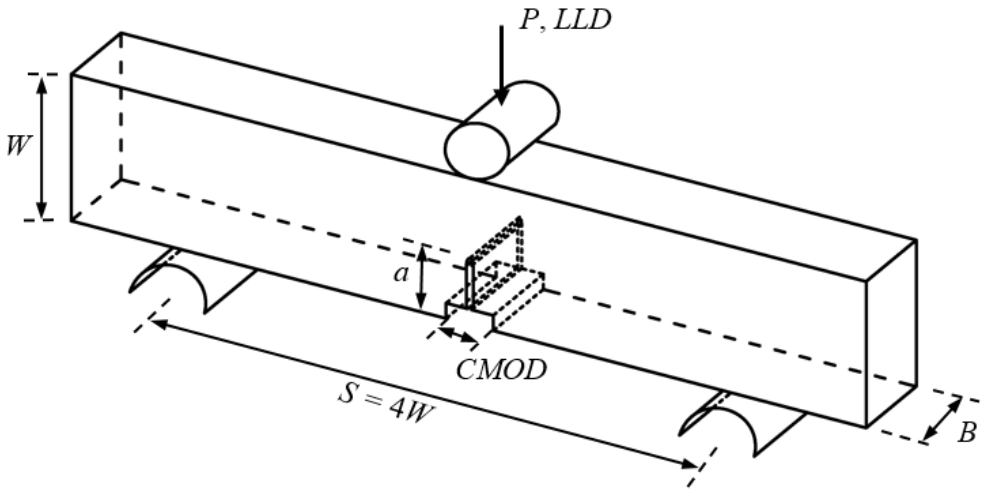

(b) Plane-sided three-point single-edge bend (SE(B)) specimen

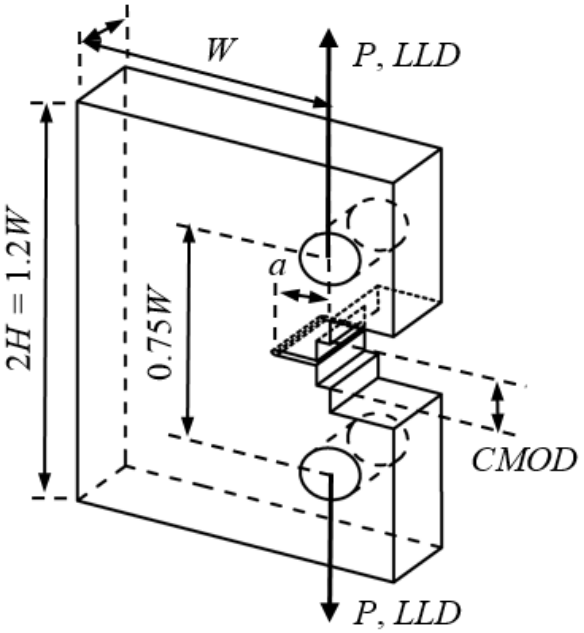

(c) Plane-sided compact tension (C(T)) specimen

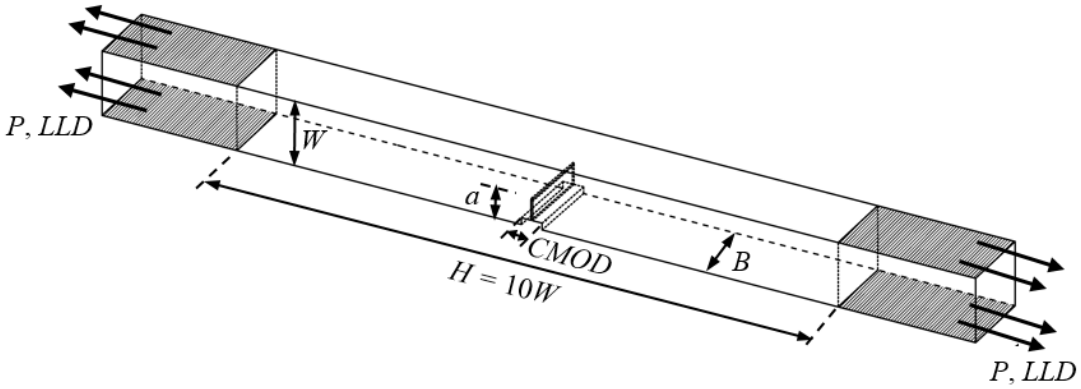

(d) Plane-sided clamped single-edge tension (SE(T)) specimen

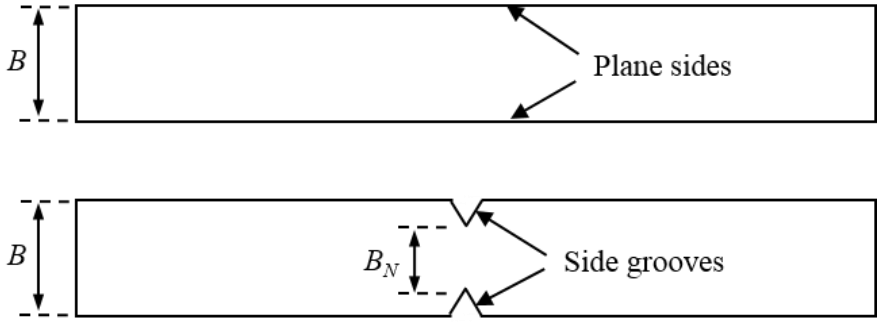

(e) Schematic of side grooves

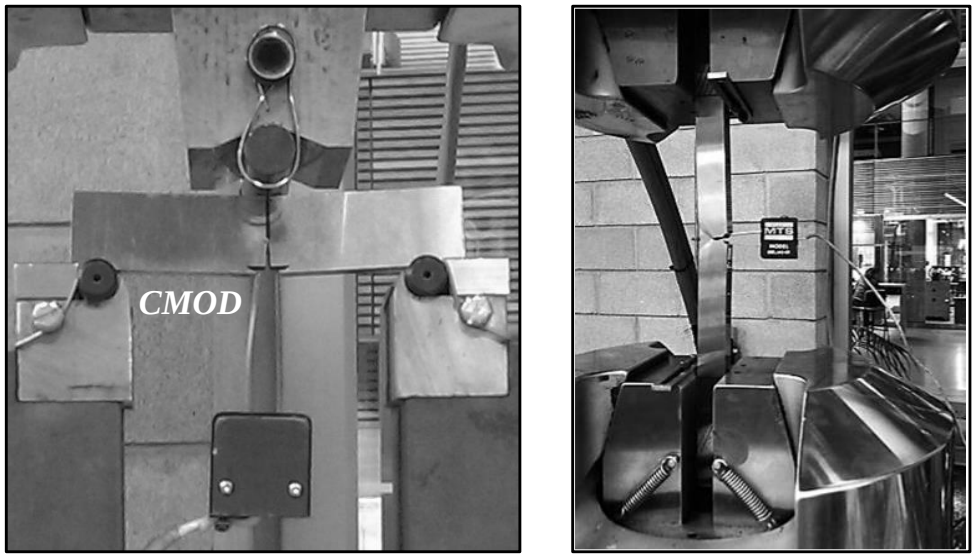

(f) Experiment set-up for the single-edge bend (SE(B)) and the clamped single-edge tension (SE(T)) specimens

Figure 2.1. Schematic and experiment set-up of small-scale specimens

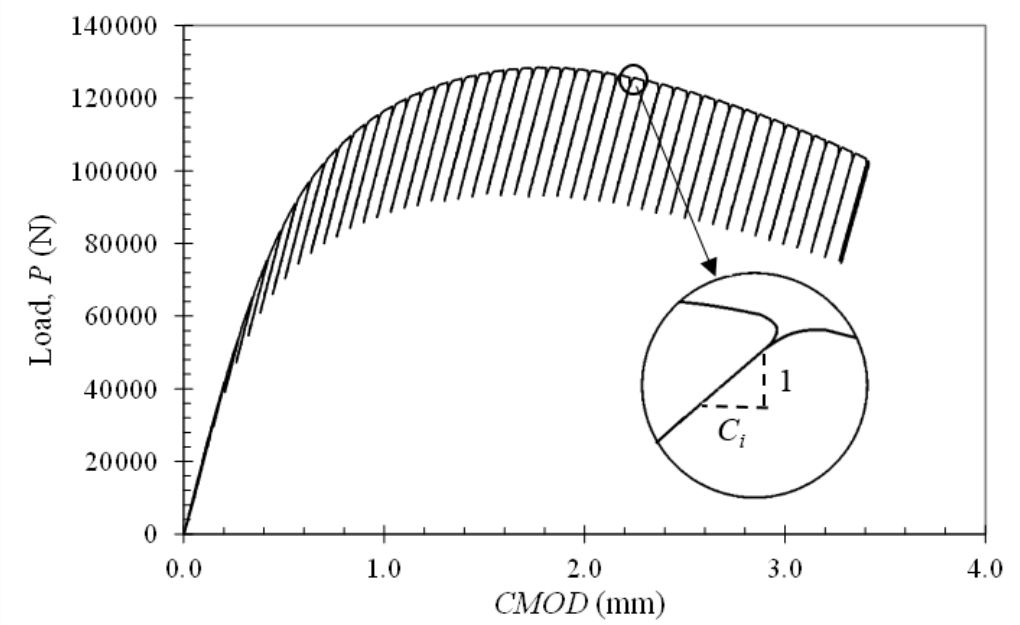

Figure 2.2. *P-CMOD* curve using elastic unloading compliance method (Wang et al. 2012)

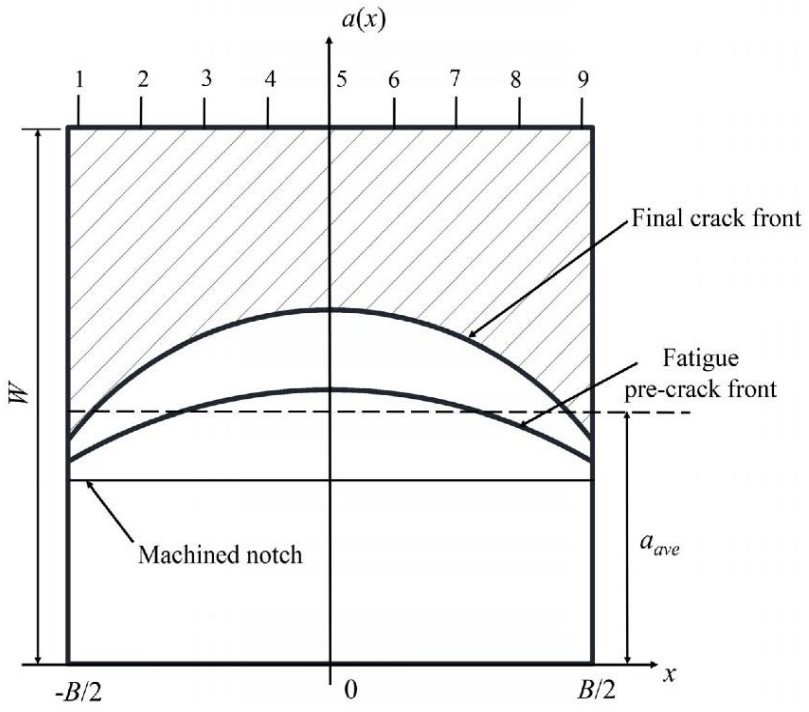

Figure 2.3. Schematic illustration of symmetric bowed crack fronts

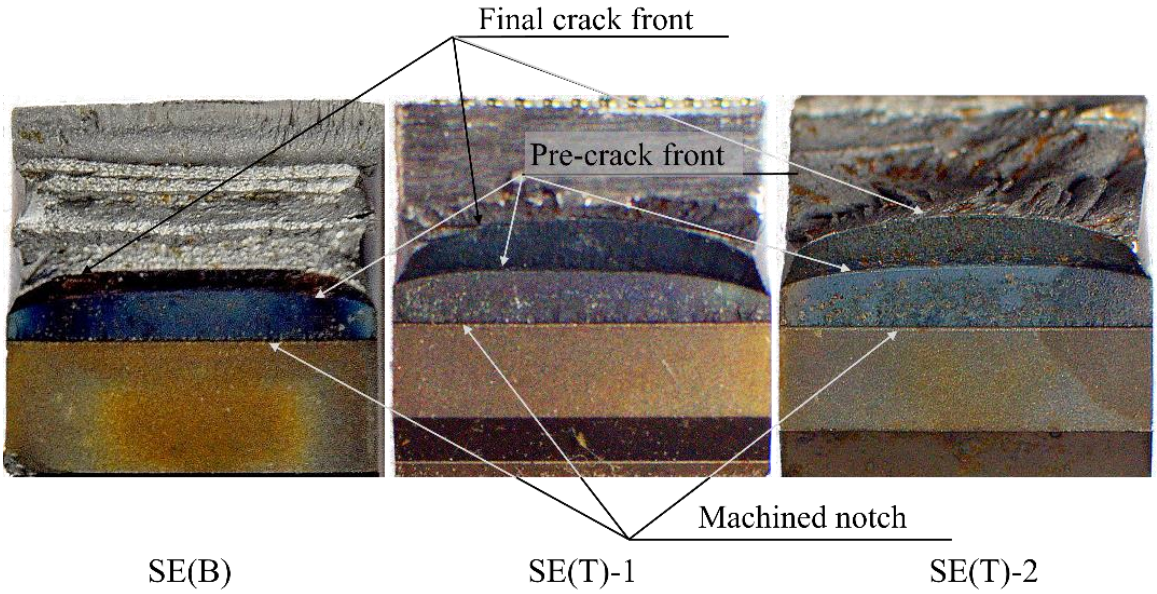

Figure 2.4. Typical crack fronts of SE(B) and SE(T) specimens

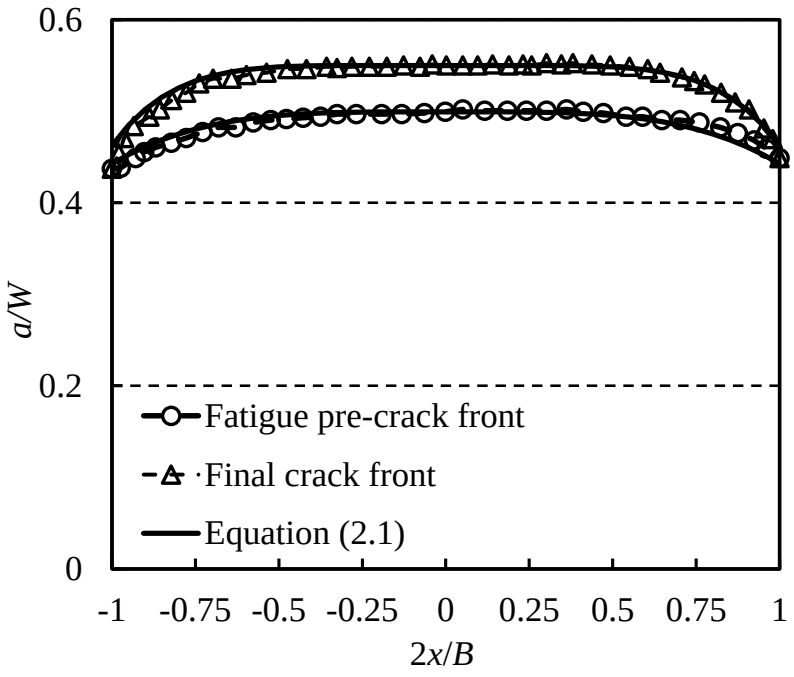

(a) SE(B) - 1

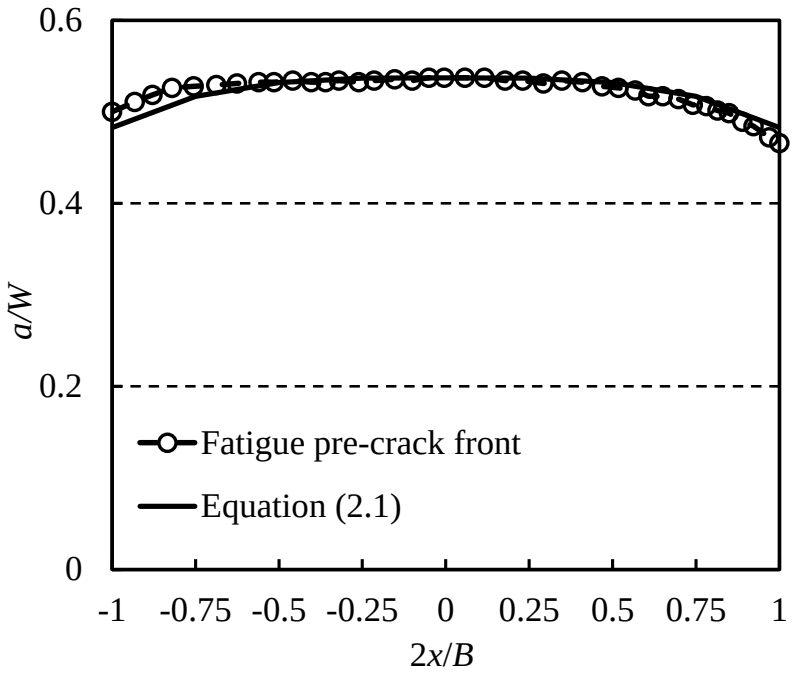

(b) SE(T) - 1

Figure 2.5. Comparison of actual and fitted crack fronts for one SE(B) specimen and one SE(T) specimen

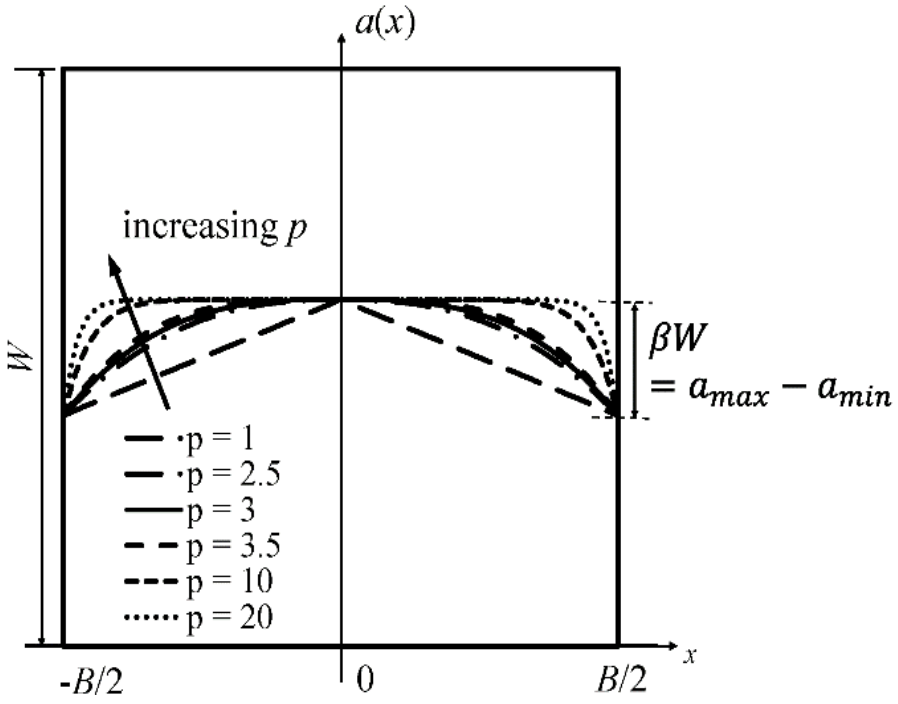

Figure 2.6. Schematic illustration of symmetric bowed crack fronts with a fixed β and varying p

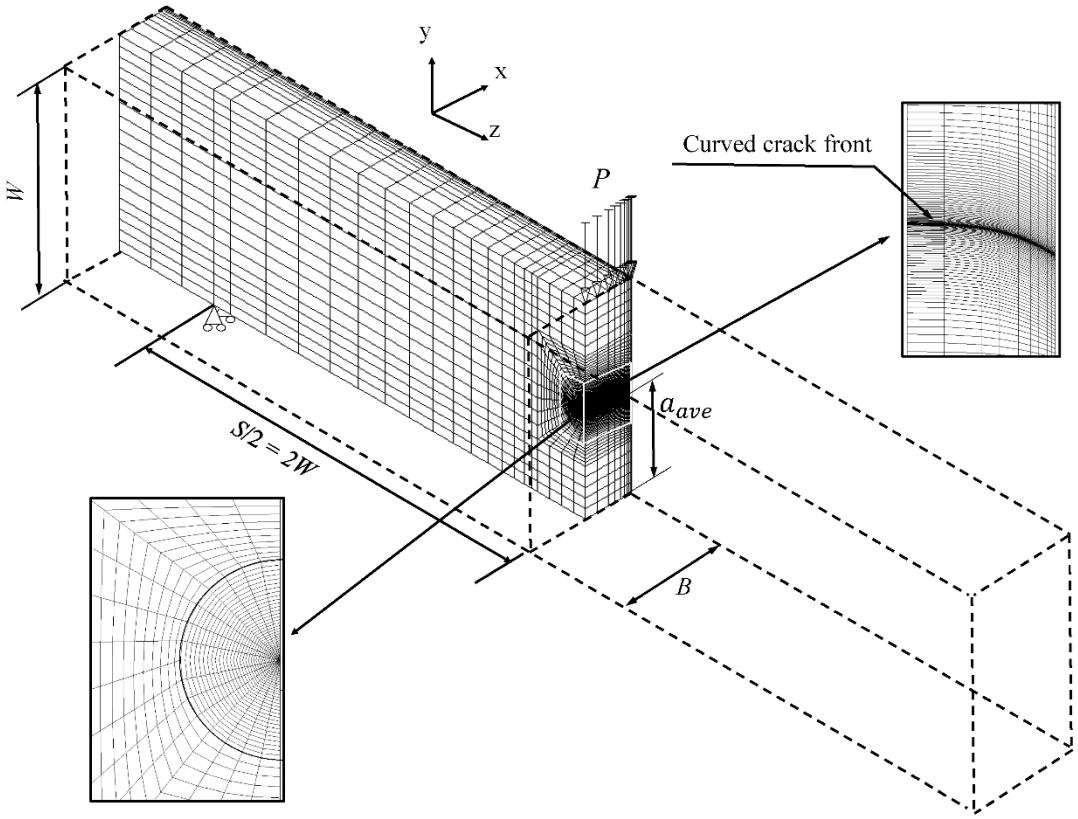

Figure 2.7. Geometric and mesh configuration of the finite element model

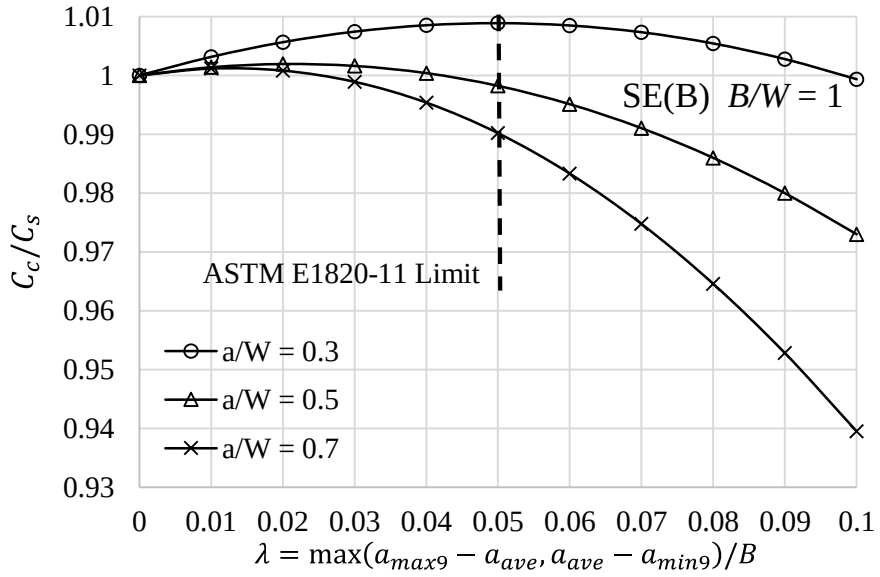
1.01
1
0.99
0.98
0.97
0.96
0.95
0.94
0.93
C_c/C_s
SE(B) B/W = 1
ASTM E1820-11 Limit
a/W = 0.3
a/W = 0.5
a/W = 0.7
0 0.01 0.02 0.03 0.04 0.05 0.06 0.07 0.08 0.09 0.1
$\lambda = \max(a_{max9} - a_{ave}, a_{ave} - a_{min9})/B$

(a) *B/W* = 1

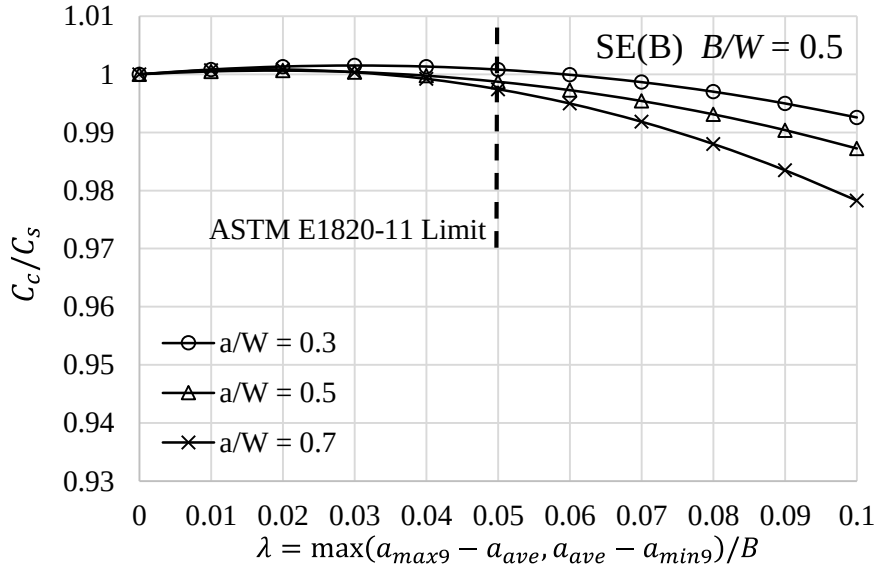
1.01
1
0.99
0.98
0.97
0.96
0.95
0.94
0.93
C_c/C_s
SE(B) B/W = 0.5
ASTM E1820-11 Limit
a/W = 0.3
a/W = 0.5
a/W = 0.7
0 0.01 0.02 0.03 0.04 0.05 0.06 0.07 0.08 0.09 0.1
$\lambda = \max(a_{max9} - a_{ave}, a_{ave} - a_{min9})/B$

(b) *B/W* = 0.5

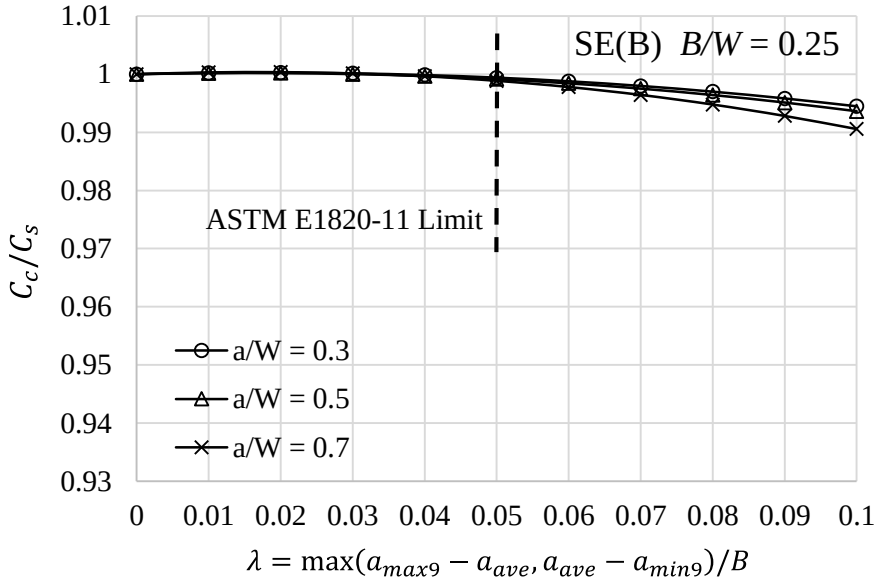

(c) *B/W* = 0.25

Figure 2.8. Variation of C_c/C_s against λ

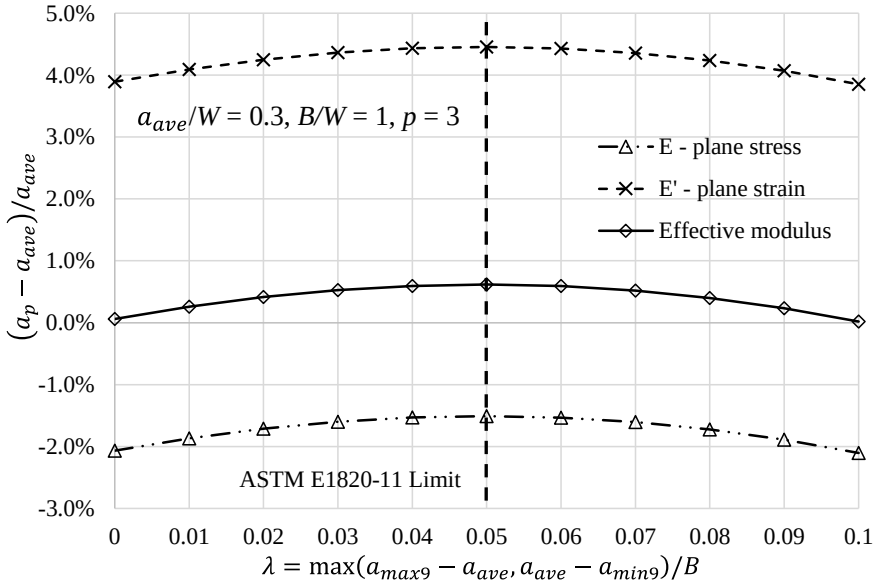

(a) a_{ave}/W = 0.3 and B/W = 1

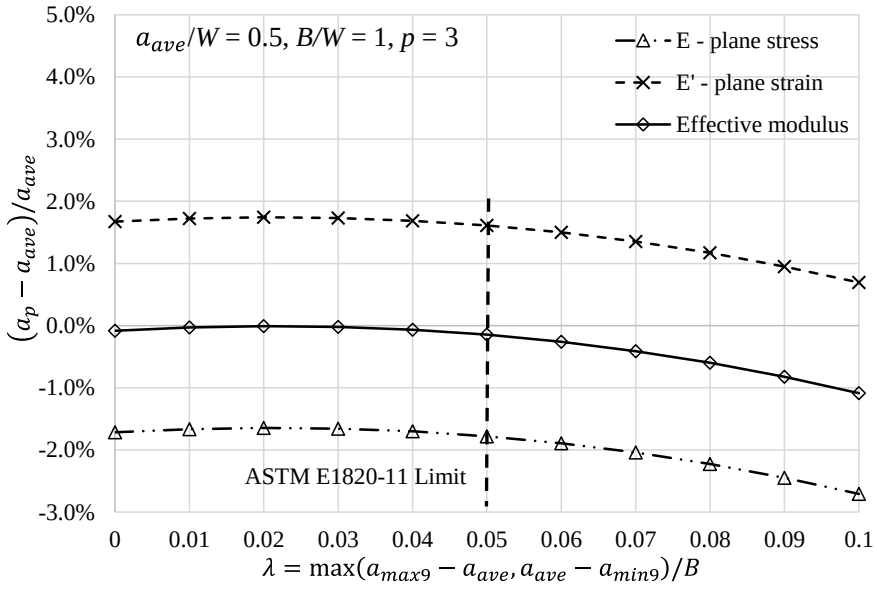

(b) a_{ave}/W = 0.5 and B/W = 1

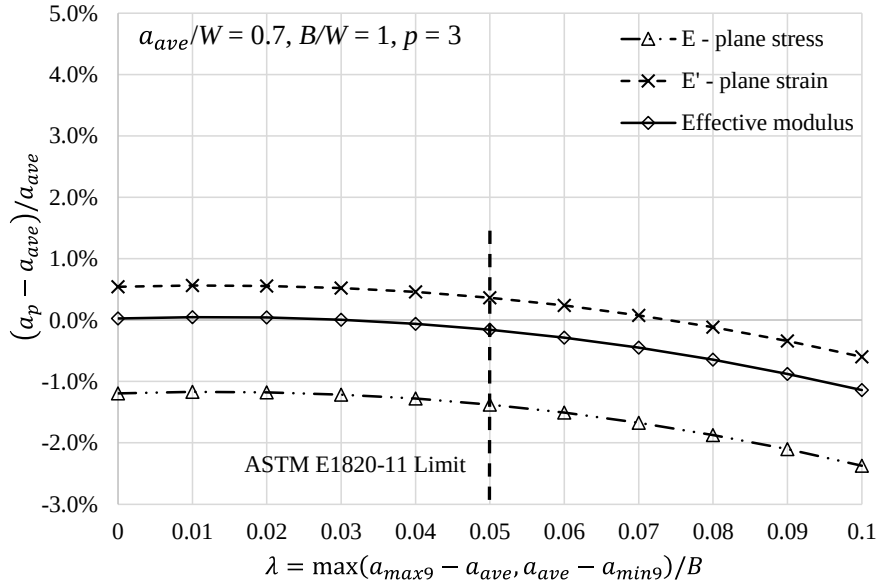

(c) a_{ave}/W = 0.7 and B/W = 1

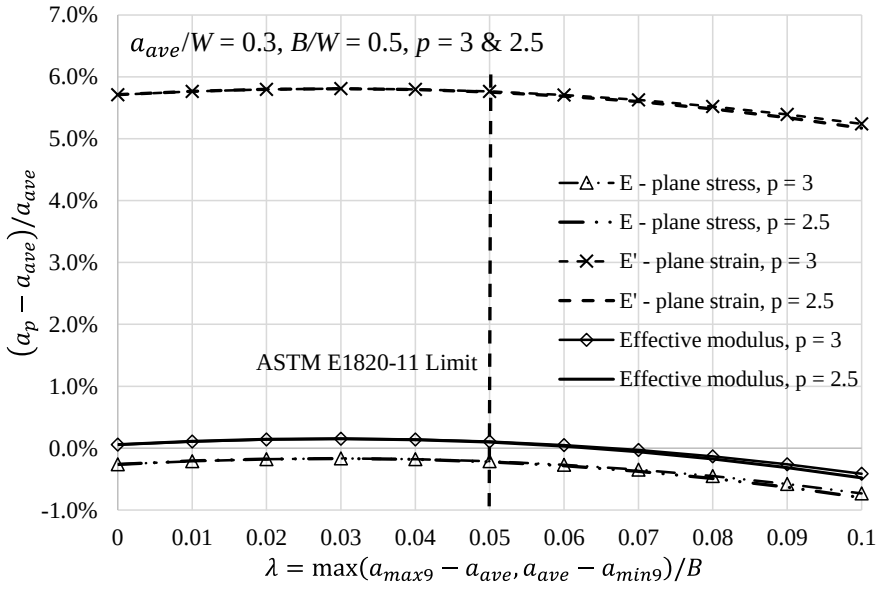

(d) a_{ave}/W = 0.3 and B/W = 0.5

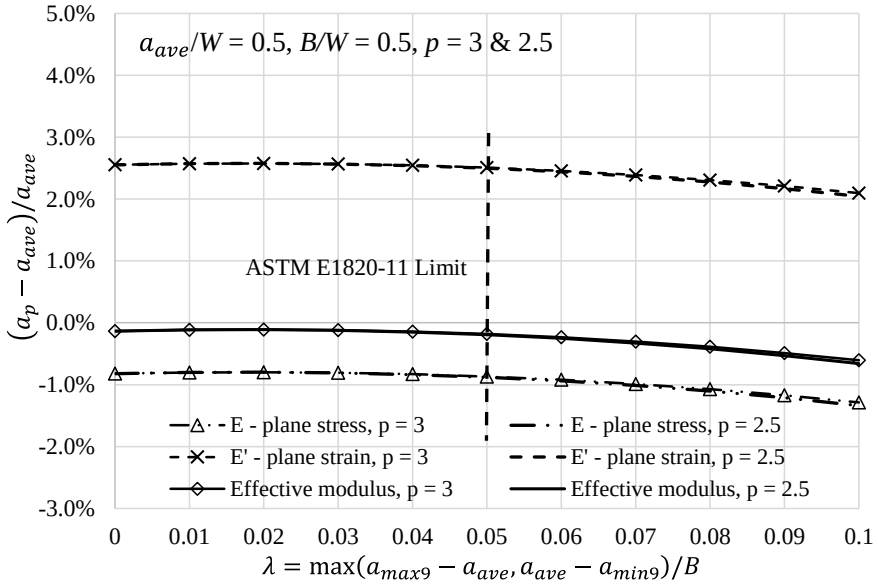

(e) a_{ave}/W = 0.5 and B/W = 0.5

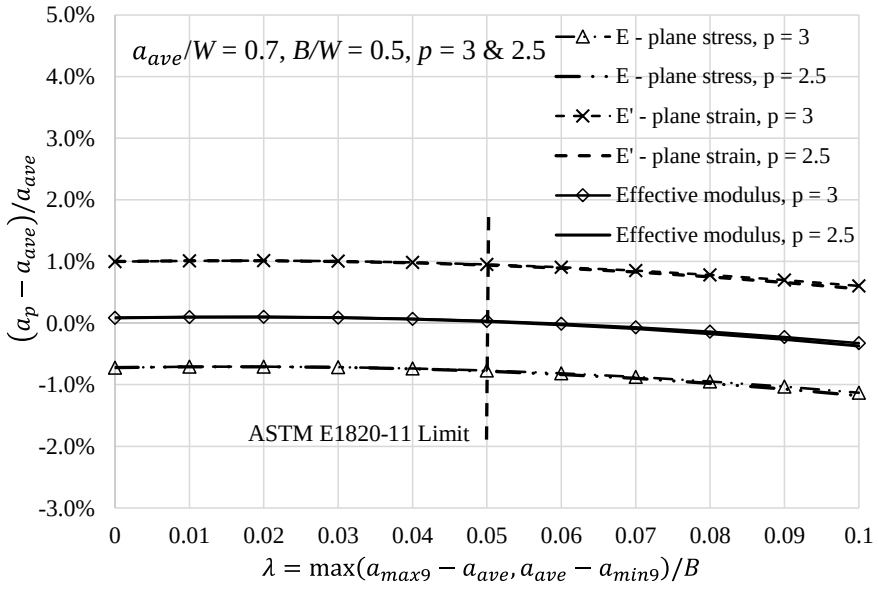

(f) a_{ave}/W = 0.7 and B/W = 0.5

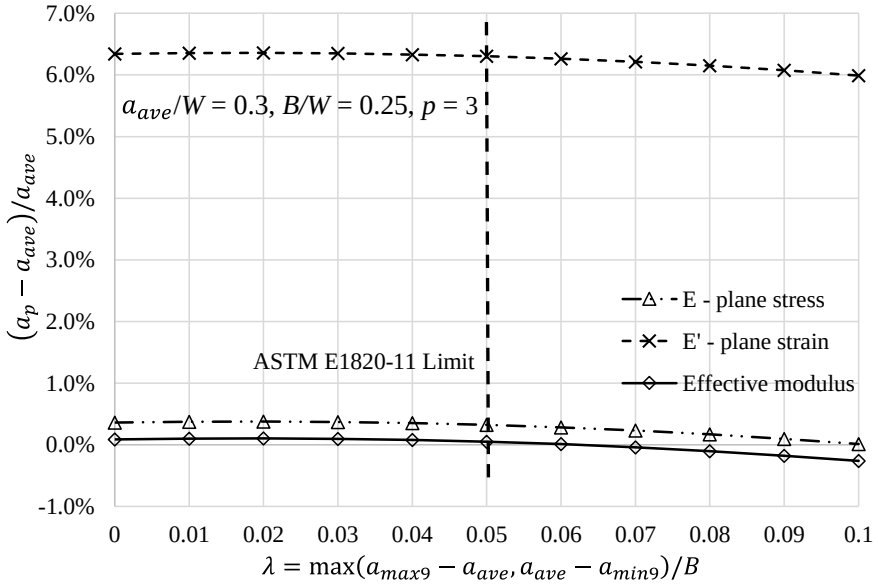

(g) a_{ave}/W = 0.3 and B/W = 0.25

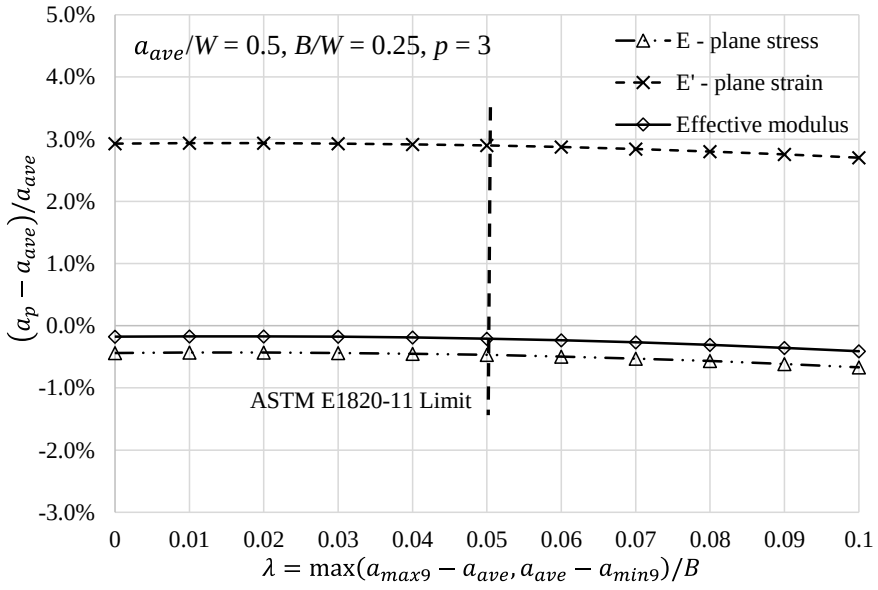

(h) a_{ave}/W = 0.5 and B/W = 0.25

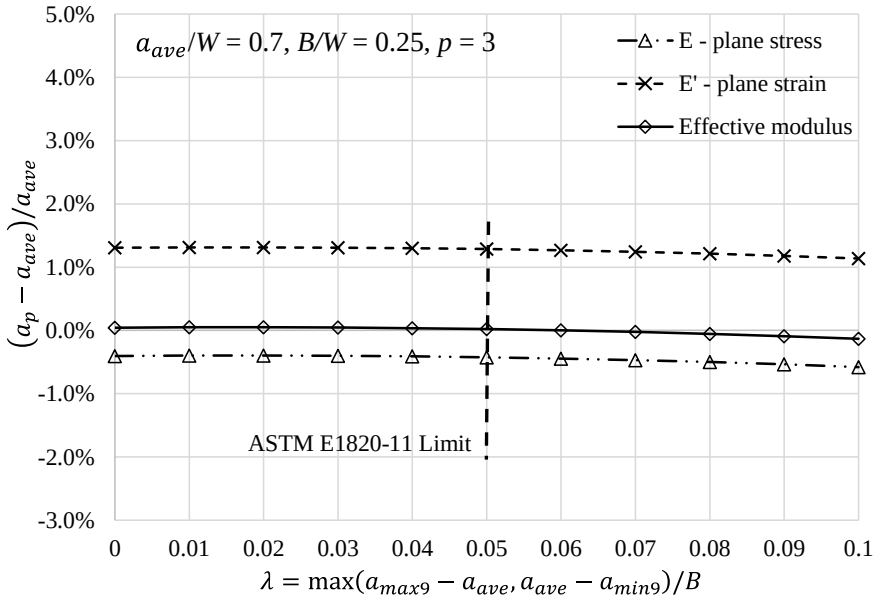

(i) a_{ave}/W = 0.7 and B/W = 0.25

Figure 2.9. Variation of the error e_a against λ

Chapter 3 Effect of Crack Front Curvature on Experimental Evaluation of J-integral for Single-edge Bend Specimens

3.1 Introduction

Single-edge bend (SE(B)) specimens are extensively used to develop the fracture toughness resistance curves such as the J-integral resistance curve (*J-R* curve), which is an important input of the strain-based design of energy pipelines with respect to planar defects. To simulate natural cracks, all the machine notched specimens need to be fatigue pre-cracked before the toughness testing. As shown in Chapter 2, the fatigue pre-cracking often introduces curved rather than straight crack fronts (see Figs. 2.3 and 2.4). There are two main components of the fracture toughness resistance curve, namely the crack growth, Δa, and the toughness value corresponding to the crack growth. The impact of the crack front curvature on the accuracy of the crack length predicted from the crack mouth opening displacement (*CMOD*) compliance has been investigated and reported in Chapter 2. This chapter focuses on the investigation of the effect of the crack front curvature on the experimentally determined J-integral (*J*).

3.1.1 Experimental Evaluation of *J*

Begley and Landes (1972) first recognized that the J-integral (*J*) can be experimentally determined from its interpretation as the energy release rate:

$$J = -\frac{dU}{Bda} \tag{3.1}$$

where *U*, *B* and *a* denote the strain energy, specimen thickness and crack length, respectively. A series of testing specimens with the same specimen thickness, initial crack lengths and material are loaded to various values of the load line displacement (*LLD*) and final crack lengths. From the measured load-displacement data, Begley and Landes (1972) determined the energy absorbed by each specimen and then calculated *J* using Eq. (3.1). Since multiple specimens need to be tested and analyzed to determine a single experimental result of *J*, this *J* testing technique is costly and time consuming (Anderson, 2005).

The work by Rice et al. (1973) introduced a more convenient way to evaluate *J* directly from the load displacement curve of a single test specimen. Either the load controlled (Eq. 3.2a) or displacement controlled (Eq. 3.2b) condition could be used to determine *J* as follows (see Fig. 3.1):

$$J = \frac{1}{B}\int_0^P \frac{\partial \Delta}{\partial a} dP \tag{3.2a}$$

or

$$J = -\frac{1}{B}\int_0^\Delta \frac{\partial P}{\partial a} d\Delta \tag{3.2b}$$

where *P* denotes the applied load; Δ is the specimen displacement, which could be either the load-line displacement (*LLD*) or *CMOD*, and *U* is defined as the area under the load-displacement curve as shown in Fig. 3.1. Based on the limit load analysis, Sumpter and Turner (1976) proposed an alternative form of Eq. (3.2b):

$$J = \frac{\eta}{(W-a)B}\int_0^\Delta P d\Delta = \frac{\eta A}{(W-a)B} \tag{3.3}$$

where *W* is the specimen width; *a* is the equivalent crack length, which can be determined from the unloading compliance method using a single specimen according to ASTM E1820-11 as discussed in Chapter 2; η is a dimensionless geometry factor relating *J* and the strain energy, and *A* represents the total area under the load versus displacement curve, which is the total work done by the external force during the test. A typical load-displacement curve is shown in Fig. 3.2. The total area, *A*, under the load-displacement curve can be separated by the elastic unloading path into an elastic component, A_{el}, and a plastic component, A_{pl}, i.e. $A = A_{el} + A_{pl}$. Similarly, this unloading path separates the total displacement Δ into an elastic component, Δ_{el}, and a plastic component, Δ_{pl}, i.e. $\Delta = \Delta_{el} + \Delta_{pl}$, and the *J* value can also be separated into two components accordingly:

$$J = J_{el} + J_{pl} \tag{3.4}$$

where J_{el} and J_{pl} are the elastic and plastic components of J, respectively. The elastic component of J can be directly calculated from the stress intensity factor K as specified in ASTM E1820-11 (ASTM, 2011):

$$J_{el} = \frac{K^2(1-\nu^2)}{E} \tag{3.5}$$

where E and ν are the Young's modulus and the Poisson's ratio, respectively; the evaluation of the stress intensity factor, K is well documented (e.g. Tada et al. 1973) for various structure configurations. The plastic component of J can be determined from Eqs. (3.2a) or (3.2b) and (3.3) as:

$$J_{pl} = \frac{1}{B}\int_0^P \frac{\partial \Delta_{pl}}{\partial a} dP = -\frac{1}{B}\int_0^{\Delta_{pl}} \frac{\partial P}{\partial a} d\Delta_{pl} = \frac{\eta_{pl} A_{pl}}{(W-a)B} \tag{3.6}$$

where η_{pl} denotes the dimensionless plastic eta factor that relates A_{pl} to J_{pl}. It is noted that both the *P-CMOD* and *P-LLD* curves can be used to evaluate J; therefore, η_{pl} have *CMOD*-based and *LLD*-based values, denoted as η_{pl}^{CMOD} and η_{pl}^{LLD}, respectively. Therefore, Eqs. (3.4), (3.5) and (3.6) can be rewritten as:

$$J = \frac{K^2(1-\nu^2)}{E} + \frac{\eta_{pl}^{CMOD} A_{pl}^{CMOD}}{(W-a)B} \tag{3.7a}$$

or

$$J = \frac{K^2(1-\nu^2)}{E} + \frac{\eta_{pl}^{LLD} A_{pl}^{LLD}}{(W-a)B} \tag{3.7b}$$

These two plastic eta factor-based equations can be employed to experimentally determine J from the obtained *P-CMOD* or *P-LLD* curves as specified in ASTM E1820-11. The following expression of η_{pl}^{CMOD} proposed by Zhu et al. (2008) was adopted in ASTM E1820-11 for both the standard deeply-cracked SE(B) specimens (i.e. the initial crack length greater than or equal to 0.45) and non-standard shallow-cracked SE(B) specimens (i.e. the initial crack length less than 0.45):

$$\eta_{pl}^{CMOD} = 3.667 - 2.199\left(\frac{a}{W}\right) + 0.437\left(\frac{a}{W}\right)^2 \tag{3.8}$$

As to η_{pl}^{LLD}, a constant value of 1.9 is used for standard SE(B) specimens, but there is no recommended value for non-standard specimens in ASTM E1820-11. For the sake of completeness of the current study, the following expression also from Zhu et al. (2008) was employed to evaluate η_{pl}^{LLD} for the shallow-cracked specimens included in this study:

$$\eta_{pl}^{LLD} = 1.620 + 0.850\left(\frac{a}{W}\right) - 0.651\left(\frac{a}{W}\right)^2 \tag{3.9}$$

3.1.2 Literature Review and Objective

Numerical and experimental studies have been performed to investigate the impact of the crack front curvature on the crack driving forces (e.g. stress intensity factor, energy release rate, *J* and crack tip opening displacement (*CTOD*)) in SE(B) specimens. For example, Crouch (1991) carried out three-dimensional (3D) linear-elastic finite element analyses (FEA) of SE(B) specimens and indicated that if the maximum and minimum crack lengths on a curved crack front differ by 30%, the maximum energy release rate along the curved crack front can be twice the maximum energy release rate on a straight crack front with the same average length. Based on 3D elastic-plastic FEA of the compact tension (CT) and SE(B) specimens containing curved crack fronts, Nikishkov et al. (1999) pointed out that the crack front curvature, as allowed in test standards ASTM E813 (1989), ASTM E1290 (1989) and ESIS P2-92 (1992), has a significant influence on the ratio between the crack tip opening displacements (*CTOD*) obtained at the mid-plane of the crack front and the surfaces of the specimen. Zhou and Soboyejo (2002) developed experimental techniques to fabricate A707 steel SE(B) specimens with controlled crack front curvatures, and reported that the critical *CTOD* experimentally determined at the mid-plane of the SE(B) specimen increases with the crack front curvature. The critical *CTOD* corresponding to a crack front curvature of approximately 0.11 mm^{-1} can be 50% higher than that corresponding to a straight crack front.

The aforementioned studies all focused on the effects of the crack front curvature on the local crack driving forces. The present study focused on the effect of the crack front curvature on the average J-integral (*J*) over the crack front, which is more relevant to the characterization of the experimentally determined *J-R* curve (Zhou and Soboyejo, 2002).

The impact of the crack front curvature on the average J evaluated using the plastic eta factor-based approach, i.e. Eqs. (3.7a) and (3.7b), for SE(B) specimens was investigated in this study. The values of the plastic eta factors, i.e. Eqs. (3.8), (3.9) or the constant value of 1.9, are obtained from specimens with straight crack fronts (Zhu et al., 2008; ASTM, 2011). Therefore, applying plastic eta factors that are based on straight crack fronts to specimens with curved crack fronts will lead to errors in the calculated J values. This investigation sheds light on the magnitudes of such errors.

ASTM E1820-11 specifies the allowable deviation of a curved crack front from a straight front based on the so-called nine-point measurement method. It requires that none of the nine physical measurements of the initial (final) crack size differ by more than $0.05B$ from the average initial (final) crack length a_{ave} obtained from the nine measurements. Test specimens that do not meet this criterion are deemed unacceptable and therefore rejected. In this regard, the other objective of the present study was to examine the adequacy of the crack front straightness criterion in ASTM E1820-11 as far as the accuracy of the average J evaluation is concerned.

3.1.3 Approach

In this study, systematic 3D finite element analyses of plane-sided SE(B) specimens with a wide range of thickness-to-width ratios, crack lengths and crack front curvatures were carried out. For a given specimen with a curved crack front, the average J values over the crack front evaluated using the virtual crack extension method (see Appendix B (ADINA, 2012)) were compared with the J values evaluated using the plastic eta factor-based approach to quantify the errors in J obtained from the latter approach. The crack front straightness criteria specified in ASTM E1820-11 were examined. Based on the analysis results, crack front straightness criteria that are in most cases less stringent than that specified in ASTM E1820-11 were proposed.

The rest of this chapter is organized as follows. The 3D FEA models and analysis procedures are described in Section 3.2; Section 3.3 presents the comparison of J values evaluated using different methods and the recommendation concerning the crack front

straightness criterion in ASTM E1820-11, and the summary and concluding remarks are presented in Section 3.4.

3.2 Finite Element Analyses

3.2.1 Finite Element Model

The 3D finite element analyses were carried out by the commercial software package ADINA 8.7.4 (ADINA, 2012). All the SE(B) specimens considered in this study are plane-sided, and have the same width and the standard span-to-width ratio (*S/W* = 4), but three different relative average crack lengths a_{ave}/W (i.e. a_{ave}/W = 0.3, 0.5 and 0.7) and three different specimen thicknesses (i.e. *B/W* = 1, 0.5 and 0.25) covering the range of *B/W* ratios suggested in ASTM E1820-11 (ASTM, 2011). Specimens with both straight and curved crack fronts were included. For specimens with curved crack fronts, the so-called nine-point measurement method was employed to evaluate the average crack length as specified in ASTM E1820-11. The bowed and symmetric crack fronts are assumed and characterized by the following two equations, which are the same as Eqs. (2.4) and (2.5), respectively (see Section 2.2 and Fig. 2.6):

$$a(x) = a_{ave} + \beta W \left\{ \left(0.25 - \frac{\Delta}{2B}\right)^p \cdot \frac{1}{8}\sum_{i=1}^{i=8}[abs(i-5)]^p - \left(\frac{abs(x)}{B/2}\right)^p \right\} \tag{3.10}$$

$$\beta = \frac{\lambda}{\left(\frac{W}{B}\right)\left(0.25-\frac{\Delta}{2B}\right)^p \left[4^p - \frac{1}{8}\sum_{i=1}^{i=8}[abs(i-5)]^p\right]} \tag{3.11}$$

where *p* is the shape parameter in the assumed power-law function; $\Delta = 0.005W$ and $\beta = a(0)/W - a(B/2)/W$. To put the equations in the context of the crack front straightness criterion specified in ASTM E1820-11, a parameter λ, $\lambda = \max(a_{max9} - a_{ave}, a_{ave} - a_{min9})/B$, was introduced, where a_{max9} and a_{min9} are the maximum and minimum values of the nine physical measurements, respectively. Note that a straight crack front corresponds to λ = 0; the crack front curvature increases with λ, and λ = 0.05 corresponds to the maximum allowable crack front curvature as specified in ASTM E1820-11.

In this study, *p* = 3 was assumed for the majority of the specimens with curved crack fronts following the study by Nikishkov et al. (1999) as well as the investigation carried

out at Western (see Section 2.2), whereas λ was assigned values of 0.05 to 0.09 with an increment of 0.01. In addition, specimens with curved crack fronts characterized by p = 2.5 and selected geometric configurations (i.e. B/W = 0.5, a_{ave}/W = 0.3 and 0.7) were also considered as sensitivity cases to investigate the impact of the shape parameter p on the evaluation of J.

The geometric and mesh configurations of the FEA model used in the present study are the same as those presented in Chapter 2 as illustrated in Fig. 2.7. A quarter of the specimen with a sharp crack tip was modeled and divided into ten layers in the thickness direction with the mesh density increasing from the mid-plane to the free surface to capture the high stress gradients near the free surface. To reduce the computation time, 8-node 3D isoparametric brick elements (as opposed to the 20-node brick elements used in Chapter 2) (ADINA, 2012) was employed to carry out this elastic-plastic J-integral analysis. The accuracy of using the 8-node isoparameteric brick elements for calculating J has been shown to be adequate (Kulka and Sherry, 2012). The total number of elements is about 11,000 in a typical specimen model. The mesh surrounding the crack tip consists of 40 concentric semicircles as shown in Fig. 2.7. In the vicinity of the crack tip, the smallest element has dimensions of about 1/3000W and 1/75B in the width and thickness directions, respectively. The aspect ratio of these elements is less than 7. Stationary cracks were assumed in all the models.

3.2.2 Material Model

The uniaxial stress-strain relationship is described by the Ramberg-Osgood law (Ramberg and Osgood, 1943) as follows:

$$\frac{\varepsilon}{\varepsilon_0} = \frac{\sigma}{\sigma_0} + \alpha \left(\frac{\sigma}{\sigma_0}\right)^n \tag{3.12}$$

where σ_0 is the reference stress; ε_0 is the reference strain, $\varepsilon_0 = \sigma_0/E$; α is a dimensionless parameter, and n denotes the strain hardening exponent. In this study, materials with $\sigma_0 = \sigma_{YS}$ = 550 MPa, E = 200 GPa, and α = 1 were selected to simulate the X80-grade pipeline steel, where σ_{YS} is the yield strength. Two values of n, namely n = 10 and 20, were

considered in this study to investigate the effect of strain hardening exponent on the *J* calculation.

3.2.3 Computational Procedure

A displacement-controlled line-load was used in all the models. The loading rate varies from about 50 - 100 steps/mm depending on the configuration of the specimen. Using more loading steps was found to have no impact on the load-displacement relationship or *J* values evaluated from FEA. The incremental theory of plasticity (Lubliner, 2008), von Mises yield criterion and isotropic hardening rule were employed in the analysis. The von Mises yield criterion indicates that yielding starts once the second invariant of the deviatoric stress tensor, J_2, reaches a critical value (i.e. $\sigma_{YS}^2/3$). The incremental theory of plasticity combined with the associate flow rule and von Mises yield criterion can be characterized by the following constitutive equation:

$$d\varepsilon_{ij}^{pl} = d\lambda \cdot s_{ij} \tag{3.13}$$

where ε_{ij}^{pl} and s_{ij} (i, j = 1, 2 and 3) are the plastic strain tensor and the deviatoric stress tensor, respectively, and $d\lambda$ is a scalar factor of proportionality. Fracture toughness tests reported in the literature (e.g. Zhu et al., 2008; Park et al., 2011; Wang et al., 2012) indicate that the maximum applied load (P) for the SE(B) specimen is usually about 1.5 to 1.6P_y, where P_y is the reference load defined as $B(W - a_{ave})^2\sigma_Y/S$ (Nevalainen and Dodds, 1990). In the current study, the finite element analyses were performed to relatively large plastic deformations corresponding to P/P_y up to 1.8 and 1.6 for n = 10 and 20, respectively. Note that σ_Y is the effective yield strength, defined as $\sigma_Y = (\sigma_{YS} + \sigma_{TS})/2$ according to ASTM E1820-11(ASTM, 2011), where σ_{TS} is the ultimate tensile strength. Ignoring the elastic strain in Eq. (3.12) and applying Considere's necking criterion (Soboyejo, 2003), one can derive the following equation to evaluate σ_{TS}:

$$\sigma_{TS} = \left(\frac{E{\sigma_0}^{n-1}}{ane}\right)^{1/n} \tag{3.14}$$

where e = 2.71828 is the base of the natural logarithm.

The sparse matrix solver was employed for its high efficiency in the numerical analysis (ADINA, 2012). The full Newton-Raphson iteration method was selected to find the solution of nonlinear equations with the maximum number of iterations for each step being 15. The displacement convergence criterion was selected, in which the displacement tolerance equal to 0.001 corresponding to a reference displacement of 1 mm (ADINA, 2012). Convergence studies on mesh density and loading rate were conducted and showed good convergence in the elastic-plastic analyses: Dividing the specimen into 20 as opposed to ten layers along the thickness direction, or using 500 as opposed to 50-100 steps/mm, was found to have nearly no impact on the obtained J-integral.

For a given specimen containing either a straight or curved crack, two average J values over the crack front were evaluated in this study, denoted by J^{FEA} and J^{η}, respectively. To calculate J^{FEA}, the local J values corresponding to the ten layers along the thickness direction in the FEA model were evaluated first using the virtual crack extension method (Anderson, 2005; see Appendix B for a brief illustration of the virtual crack extension method) as implemented in ADINA (ADINA, 2012), whereby virtual shifts were defined by the two outermost semicircular rings surrounding the crack tip, i.e. the 40^{th} ring (see Fig. 2.7). To ensure the path-independence of the calculated J values, the J values obtained from the use of other rings were compared with those obtained from using the 40^{th} ring. The difference was found to be less than 0.5% for all the load steps. J^{FEA} was then evaluated as the weighted average of the local J values, with the weighting factor for each layer equal to the thickness of the layer divided by the half-thickness of the specimen. Note that J^{FEA} was considered the true average J over the crack front. On the other hand, J^{η} was calculated using the plastic eta factor-based approach as specified in ASTM E1820-11, i.e. Eqs. (3.7) through (3.9). To compute J^{η}, *CMOD*, *LLD* and P corresponding to each loading step were retrieved from the FEA results. It should be noted that for a curved crack front the equivalent crack length a obtained from the unloading compliance method in general does not equal the nine-point measured average crack length a_{ave} as discussed in Chapter 2. However, the results presented in Chapter 2 suggest that the crack front curvature has a negligible impact on the crack length

evaluated from the elastic compliance of SE(B) specimens (see Section 2.4); therefore, it is assumed in this study that a equals a_{ave} for curved crack fronts.

3.3 Results and Discussions

Let $e_J = (J^{\eta} - J^{FEA})/J^{FEA}$ denote the error in J^{η}. Positive and negative values of e_J mean that J^{η} overestimates and underestimates the actual J, J^{FEA}, respectively. The values of e_J are plotted against P/P_y for specimens with curved or straight crack fronts in Figs. 3.3 through 3.6. The specimens shown in Figs. 3.3 and 3.4 have $n = 10$, and $n = 20$ cases are shown in Figs. 3.5 and 3.6. All the specimens shown in these figures with curved crack fronts have the same shape parameter $p = 3$. The errors in the *CMOD*-based J^{η} are shown in Figs. 3.3 and 3.5, whereas the errors in the *LLD*-based J^{η} are shown in Figs. 3.4 and 3.6.

The five dashed lines in the same subfigure correspond to specimens with the same B/W and a_{ave}/W but different crack front curvatures characterized by λ varying from 0.05 to 0.09, whereas the solid line in the subfigure corresponds to the specimen with a straight crack front and the same B/W and a_{ave}/W. The solid line reflects the inherent error associated with the equation (i.e. Eq. (3.8), Eq. (3.9) or the constant value of 1.9) used to evaluate the plastic eta factor. For the *CMOD*-based analysis, this inherent error ranges from -9% to -2% for shallow-cracked specimens (i.e. $a_{ave}/W = 0.3$), and from -5% to 3% for deeply-cracked specimens (i.e. $a_{ave}/W = 0.5$ and 0.7). For the *LLD*-based analysis, the inherent error is between -4% and 4% for specimens with $a_{ave}/W = 0.3$ and $B/W = 1$ and 0.5, between -4% and 15% for specimens with $a_{ave}/W = 0.3$ and $B/W = 0.25$, and between -7% and 0% for specimens with $a_{ave}/W = 0.5$ and 0.7. Figures 3.3 to 3.6 suggest that the plastic eta factors for the SE(B) specimen could be computed as a function of B/W, n and P/P_y, in addition to a_{ave}/W, such that the accuracy of J^{η} is improved and more consistent for different loading levels, the stain hardening exponents and B/W ratios. However, the improvement of the formulas for the plastic eta factors is beyond the scope of the current study.

Figures 3.3 to 3.6 show that variations of e_J with respect to P/P_y for specimens with the same a_{ave}/W, B/W and n but different λ are to a large extent similar. Given a_{ave}/W, B/W, n and P/P_y, e_J consistently increases as λ increases from 0 to 0.09, which indicates that J^η becomes less conservative and tends to overestimate the actual J as the crack front curvature increases. Figures 3.3 to 3.6 also suggest that n has a negligible impact on e_J for specimens with $B/W = 1$, $a_{ave}/W = 0.5$ and 0.7, regardless of the crack front curvature. The impact of n on e_J is somewhat more significant for specimens with all the other a_{ave}/W and B/W ratios, especially for $B/W = 0.25$. At $\lambda = 0.05$, which is the maximum allowable crack front curvature according to ASTM E1820-11, the errors in the *CMOD*- and *LLD*-based J^η are generally between -7% and 6% for $n = 10$ and 20. However, the *LLD*-based J^η overestimates the actual J by up to 17% for the specimen with $a_{ave}/W = 0.3$, $B/W = 0.25$, $n = 20$ and $\lambda = 0.05$.

Figures 3.3(a), 3.3(d), 3.5(a) and 3.5(d) indicate that for specimens with $a_{ave}/W = 0.3$ and $B/W = 1$ and 0.5, $|e_J|$ corresponding to $\lambda = 0.09$ is in general less than that corresponding to $\lambda = 0$ (i.e. straight crack front) for given P/P_y and n. These observations suggest that for such specimens, the error in J^η attributed to the crack front curvature is opposite to and less than the inherent error in η_{pl}^{CMOD} calculated from Eq. (3.8). Figures 3.3(a), 3.3(d), 3.5(a) and 3.5(d) further suggest that the crack front straightness criterion as specified in ASTM E1820-11, i.e. $\lambda \leq 0.05$, can be relaxed to $\lambda \leq 0.09$ for plane-sided SE(B) specimens with $a_{ave}/W = 0.3$ and $B/W = 1$ and 0.5, if J^η is evaluated from the *P-CMOD* curve and no more than 5% overestimation of J is considered acceptable. Consider the *CMOD*-based J^η for the other specimens and let $e_J \leq 5\%$ be satisfied at all P/P_y values. Figures 3.3(b), 3.3(e), 3.5(b) and 3.5(e) suggest that the crack front straightness criterion could be relaxed to $\lambda \leq 0.09$ and 0.07 from $\lambda \leq 0.05$, respectively, for specimens with $a_{ave}/W = 0.5$, $B/W = 1$ and 0.5; Figures 3.3(c), 3.3(f), 3.5(c) and 3.5(f) suggest that $\lambda \leq 0.06$ is acceptable for specimens with $a_{ave}/W = 0.7$, $B/W = 1$ and 0.5, regardless of n. On the other hand, Figs. 3.3(i) and 3.5(i) indicate that the crack front straightness criterion of $\lambda \leq 0.05$ may remain as is or be slightly tightened for the specimen with $a_{ave}/W = 0.7$ and $B/W = 0.25$, because e_J corresponding to $\lambda = 0.05$ marginally exceeds 5%. However, Figs. 3.3(g), 3.3(h), 3.5(g) and 3.5(h) suggest that for

specimens with a_{ave}/W = 0.3 and 0.5, and B/W = 0.25, the crack front straightness criterion is sensitive to the n values and that the criterion corresponding to n = 20 should be more stringent than that corresponding to n = 10.

New crack front straightness criteria were also suggested by considering the *LLD*-based J^{η} and the corresponding e_J shown in Figs. 3.4 and 3.6. Table 3.1 summarizes the suggested crack front straightness criteria based on considerations of *CMOD*- and *LLD*-based J^{η} and specimens with n = 10 and 20. The suggested straightness criteria for n = 20 are always equally or more stringent than those for n = 10. It is noteworthy that e_J corresponding to *LLD*-based J^{η} for the SE(B) specimen with a_{ave}/W = 0.3, B/W = 0.25 and λ = 0.05 is up to 10% and 17%, respectively, for specimens with n = 10 and 20. For this particular specimen, tightening the crack front straightness criterion with the aim of improving the accuracy of J^{η} is considered unfruitful without first improving the accuracy of the corresponding η_{pl}^{LLD}.

The impact of the shape parameter p in Eq. (2.4) on e_J was investigated based on SE(B) specimens with a_{ave}/W = 0.3 and 0.7, B/W = 0.5, n =10 and λ = 0.05 to 0.09. The values of e_J corresponding to p = 3 and 2.5 for the specimens considered are depicted in Fig. 3.7. Only the results corresponding to the straight crack front (λ = 0) and curved crack front with λ = 0.05 and 0.09 are plotted, and results corresponding to λ = 0.06 to 0.08 are not shown to reduce clutter. Figure 3.7 indicates that p has a negligible impact on e_J.

3.4 Summary and Concluding Remarks

Three-dimensional elastic-plastic FEA of plane-sided X80-steel SE(B) specimens with straight and curved crack fronts were performed to investigate the impact of the crack front curvature on the accuracy of the average J over the crack front, J^{η}, evaluated using the plastic eta factor-based approach as specified in ASTM E1820-11. The models analyzed contain stationary cracks with sharp crack tips, and have three average crack lengths (a_{ave}/W = 0.3, 0.5 and 0.7) and three B/W ratios (B/W = 1, 0.5 and 0.25). Symmetric bowed crack fronts with different curvatures were considered in the analysis.

The curved crack front was characterized by a power-law expression. For specimens with given a_{ave}/W, B/W and p ($p > 1$), the crack fronts with different levels of curvature can be generated from Eq. (2.4) and Eq. (2.5) by varying λ.

The eta factors recommended in ASTM E1820-11 were employed to evaluate the *CMOD*- and *LLD*-based J^{η} for all the specimens considered, except for the *LLD*-based J^{η} for the specimens with $a_{ave}/W = 0.3$, in which case the eta factors proposed by Zhu et al. (2008) were adopted.

The numerical results show that given a_{ave}/W, J^{η} becomes less conservative and tends to overestimate the actual average J, which was evaluated using the virtual crack extension method, as the crack front curvature increases. For specimens that have curved crack fronts with the crack front curvature equal to the maximum allowable value ($\lambda = 0.05$) specified in ASTM E1820-11, the errors in J^{η} are between -7% and 6% for almost all the specimens considered. For the specimen with $a_{ave}/W = 0.3$, $B/W = 0.25$ and $\lambda = 0.05$, the *LLD*-based J^{η} overestimates the actual J by up to 10% and 17%, respectively, for $n = 10$ and 20. Results of the sensitivity analysis indicate that the value of the shape parameter of the power-law expression for the curved crack front has a negligible impact on the accuracy of J^{η}. Based on the analysis results and the consideration that J^{η} overestimates the actual J by no more than 5%, new crack front straightness criteria for the SE(B) specimen were recommended. The suggested criteria vary with a_{ave}/W, B/W and n, and are in most cases less stringent than that specified in ASTM E1820-11. This could potentially lead to a decrease in the specimen rejection rate and cost savings.

Reference

ADINA (2012). *Theory and Modeling Guide*. ADINA R & D Inc., Watertown, MA.

Anderson, T. L. (2005). *Fracture Mechanics-Fundamentals and Applications, Third edition*. CRC Press, Boca Raton.

ASTM (1989). *ASTM E813-89: Standard Test Method for JIc, a Measure of Fracture Toughness, Annual Book of ASTM Standards*, America Society of Testing and Materials International, West Conshohocken, PA.

ASTM (1989). *ASTM E1290-89: Standard Test Method for Crack-tip Opening Displacement (CTOD) Fracture Toughness Measurement, Annual Book of ASTM Standards*, America Society of Testing and Materials International, West Conshohocken, PA.

ASTM (2011). *ASTM E1820-11: Standard Test Method for Measurement of Fracture Toughness*. America Society of Testing and Materials International, West Conshohocken, PA.

Begley, J. A. and Landes, J. D. (1972). The *J*-integral as a Fracture Criterion. *Fracture Mechanics*, ASTM STP 514, ASTM International, West Conshohocken, PA, 515, 1-23.

Clarke, G. A., Andrews, W. R., Paris, P. C., Schmidt, D. W. (1976). Single Specimen Tests for JIc Determination. *Mechanics of Crack Growth*, ASTM STP 590, American Society for Testing and Materials, Philadelphia, 27-42.

Crouch, B. A. (1991). The Effect of Crack Front Curvature and Side-Grooving on Three Point Bend Specimen Fracture Toughness Measurements. *International Journal of Fracture*, 52, 275–292.

ESIS (1992). *ESIS P2-92: ESIS Procedure for Determining the Fracture Behavior of Materials*. European Structural Integrity Society, Delft, Netherlands.

Kulka, R. S. and Sherry, A. H. (2012). Fracture Toughness Evaluation in C(T) Specimens with Reduced Out-of-plane Constraint. *Proceedings of the 2012 ASME Pressure Vessel and Piping Division Conference*, Toronto, Ontario, Canada, July 15–19, ASME, New York.

Lubliner, J. (2008). *Plasticity Theory*. Courier Dover Publications, Mineola, NY.

Nevalainen, M. and Dodds, R. H. (1990). Numerical Investigation of 3-D Constraint Effects in Brittle Fracture in SE(B) and C(T) Specimens. *International Journal of Fracture*, 74(2), 131–161.

Nikishkov, G. P., Heerens, J. and Hellmann, D. (1999). Effect of Crack Front Curvature and Side Grooving on CTOD δ5 and J-Integral in CT and 3PB Specimens. *Journal of Testing and Evaluation*, 27(5), 312–319.

Park, D. Y., Tyson, W. R., Gianetto, J. A., Shen, G., Eagleson, R. S., Lucon, E. and Weeks, T. S.(2011). Small-Scale Low-Constraint Fracture Toughness Test Results. CANMET Report No. 2010-28(TR), CANMET Materials Technology Lab, Hamilton, Ontario, Canada.

Ramberg, W. and Osgood, W. R. (1943). Description of Stress-strain Curves by Three Parameters. *Technical Note No. 902*, National Advisory Committee For Aeronautics, Washington DC.

Rice, J. R., Paris, P. C. and Merkle, J. G. (1973). Some Further Results of *J*-integral Analysis and Estimates. *Progress in flaws growth and fracture toughness testing*, ASTM STP 536. ASTM, 231-45.

Soboyejo, W. O. (2003). *Mechanical Properties of Engineered Materials*. Marcel Dekker, Inc., New York.

Sumpter, J. D. G., and Turner, C. E. (1976). Method for Laboratory Determination of Jc. *Cracks and Fracture*, 3-18.

Tada, H., Paris, P. C. and Irwin, G. R. (1973). *The Stress Analysis of Cracks Handbook*. Del Research Corporation, Hellertown, PA.

Wang E., Zhou, W., Shen, G., and Duan, D. (2012). An Experimental Study on J(CTOD)-R Curves of Single Edge Tension Specimens for X80 Steel. *International Pipeline Conference (IPC2012)*, Calgary, Alberta, Canada, September 24–28, Paper Number: IPC2012-90323.

Zhou, J. and Soboyejo, W. O. (2002). An Investigation of the Effects of Crack Front Curvature on the Crack-Tip Opening Displacement of A707 Steel. *International Journal of Fracture*, 115(3), 287-305.

Zhu, X. K., Leis, B. N. and Joyce, J. A. (2008). Experimental Estimation of J-R Curves From Load-CMOD Record for SE(B) Specimens. *Journal of ASTM International*, 5, 231–245.

Table 3.1: Recommended crack front straightness criteria for SE(B) specimens[1]

	a_{ave}/W	*B*/*W* = 1		*B*/*W* = 0.5		*B*/*W* = 0.25	
		n = 10	*n* = 20	*n* = 10	*n* = 20	*n* = 10	*n* = 20
CMOD-based evaluation	0.3	0.09[2]	0.09[2]	0.09[2]	0.09[2]	0.09[2]	0.07
	0.5	0.09	0.09	0.07	0.07	0.06	0.05[3]
	0.7	0.06	0.06	0.06	0.06	0.05[3]	0.05[3]
LLD-based evaluation	0.3	0.08	0.07	0.07	0.05[3]	-[4]	-[4]
	0.5	0.09[2]	0.09[2]	0.09[2]	0.08	0.08	0.06
	0.7	0.06	0.06	0.09[2]	0.09[2]	0.09	0.09

Notes:

1. The criteria are based on the maximum allowable λ (λ = max(a_{max9} - a_{ave}, a_{ave} - a_{min9})/B) consistent with that of ASTM E1820-11, and the overestimation of J being no more than 5%.

2. Based on the results shown in Figs. 3.3 to 3.6, the value could be further increased with the overestimation of J still within 5%.

3. J^{η} corresponding to λ = 0.05 (the maximum allowable crack front curvature in ASTM E1820-11) overestimates the actual J by slightly higher than 5%.

4. J^{η} corresponding to λ = 0.05 calculated based on the non-standard η_{pl}^{LLD} from Eq. (3.9) significantly overestimates the actual J.

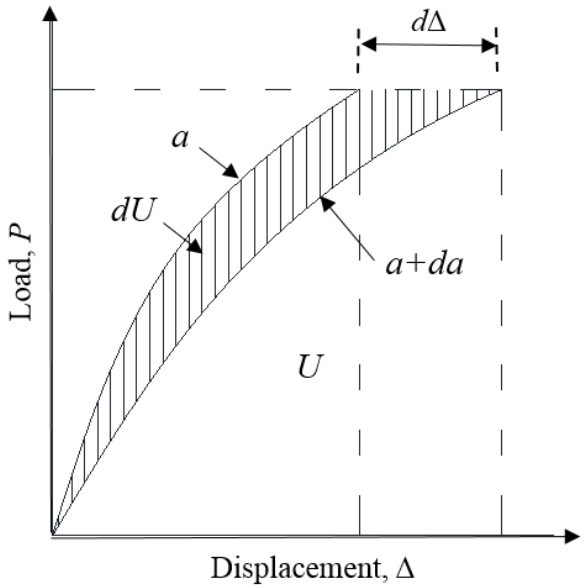

(a) Load-controled condition

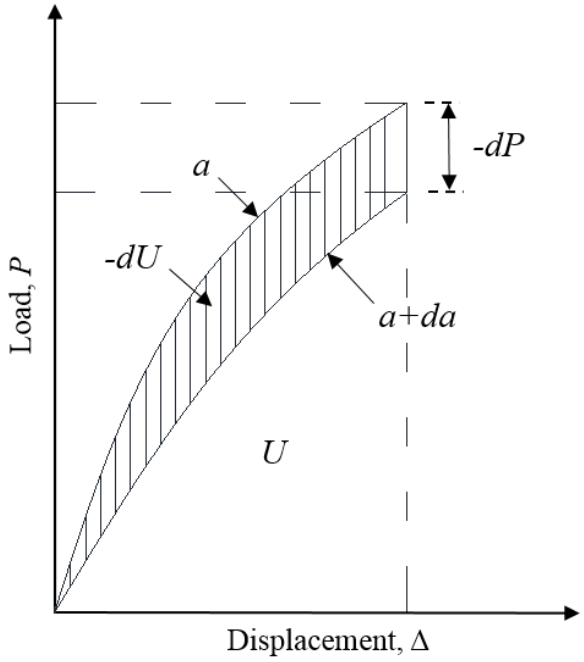

(b) Displacement-controled condition

Figure 3.1. Determination of the potential energy

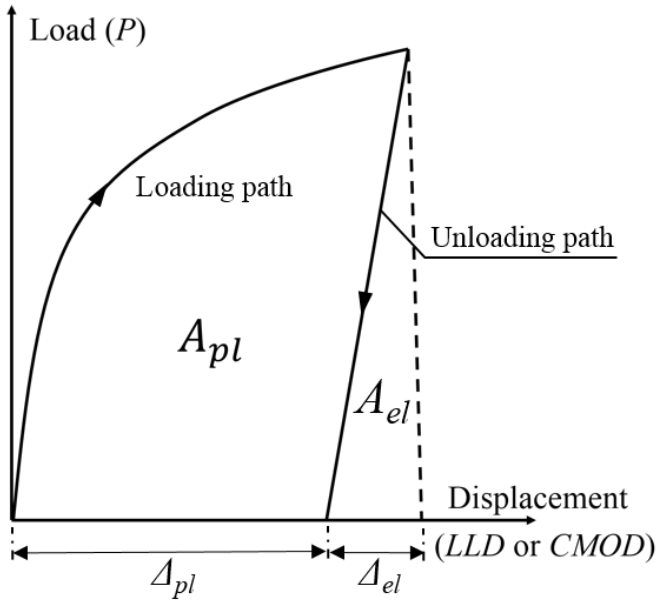

Figure 3.2. Plastic area under the load-displacement curve

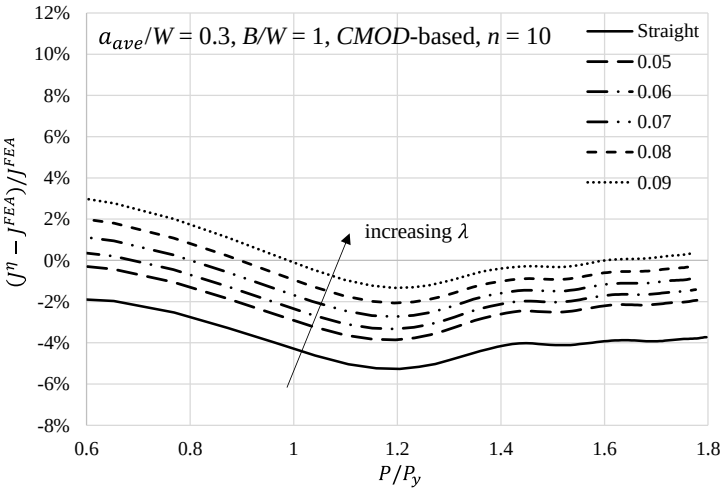
a_{ave}/W = 0.3, B/W = 1, *CMOD*-based, n = 10
Straight
0.05
0.06
0.07
0.08
0.09
increasing λ
$(J^n - J^{FEA})/J^{FEA}$
P/P_y

(a)

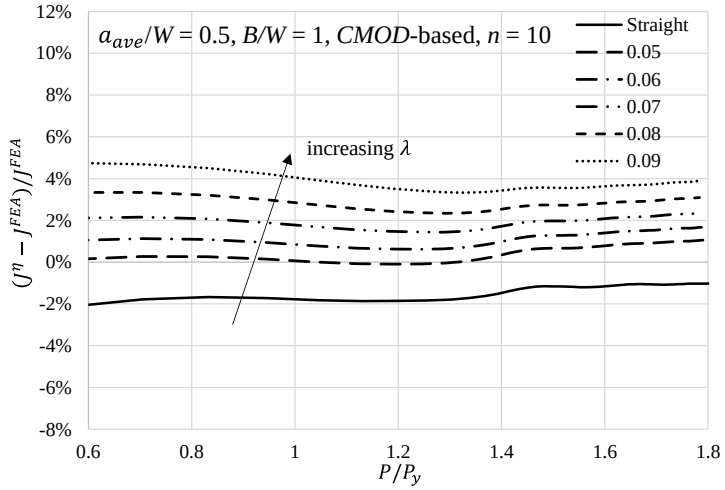
a_{ave}/W = 0.5, B/W = 1, *CMOD*-based, n = 10
Straight
0.05
0.06
0.07
0.08
0.09
increasing λ
$(J^n - J^{FEA})/J^{FEA}$
P/P_y

(b)

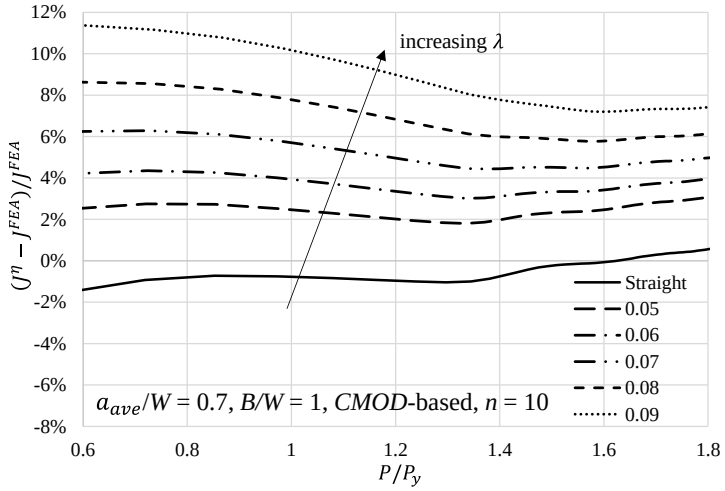
a_{ave}/W = 0.7, B/W = 1, *CMOD*-based, n = 10
Straight
0.05
0.06
0.07
0.08
0.09
increasing λ
$(J^n - J^{FEA})/J^{FEA}$
P/P_y

(c)

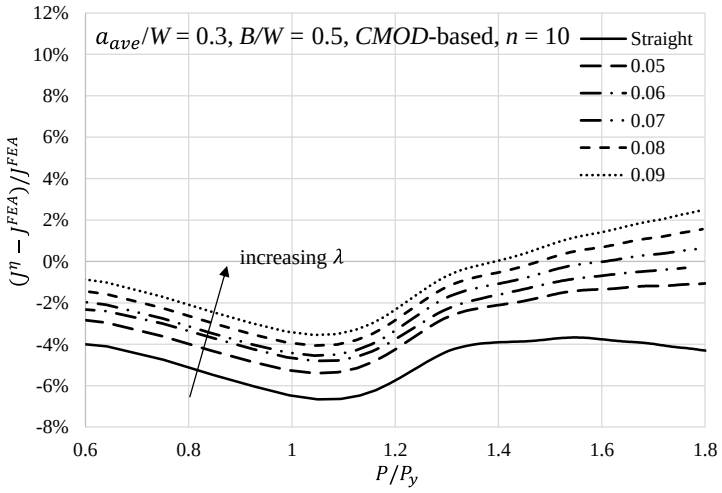
a_{ave}/W = 0.3, B/W = 0.5, *CMOD*-based, n = 10
Straight
0.05
0.06
0.07
0.08
0.09
increasing λ
$(J^n - J^{FEA})/J^{FEA}$
P/P_y
12%
10%
8%
6%
4%
2%
0%
-2%
-4%
-6%
-8%
0.6
0.8
1
1.2
1.4
1.6
1.8

(d)

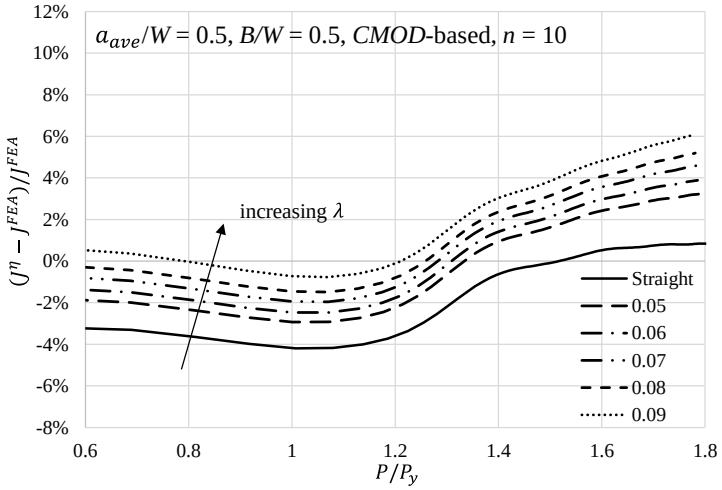
a_{ave}/W = 0.5, B/W = 0.5, *CMOD*-based, n = 10
increasing λ
Straight
0.05
0.06
0.07
0.08
0.09
$(J^n - J^{FEA})/J^{FEA}$
P/P_y
12%
10%
8%
6%
4%
2%
0%
-2%
-4%
-6%
-8%
0.6
0.8
1
1.2
1.4
1.6
1.8

(e)

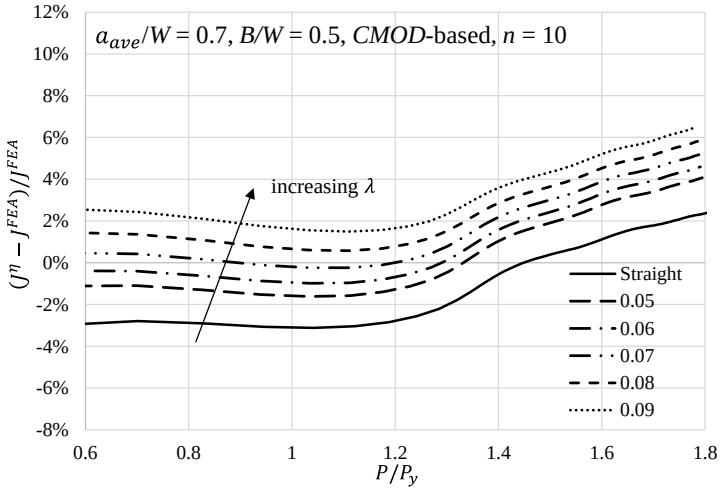
a_{ave}/W = 0.7, B/W = 0.5, *CMOD*-based, n = 10
increasing λ
Straight
0.05
0.06
0.07
0.08
0.09
$(J^n - J^{FEA})/J^{FEA}$
P/P_y
12%
10%
8%
6%
4%
2%
0%
-2%
-4%
-6%
-8%
0.6
0.8
1
1.2
1.4
1.6
1.8

(f)

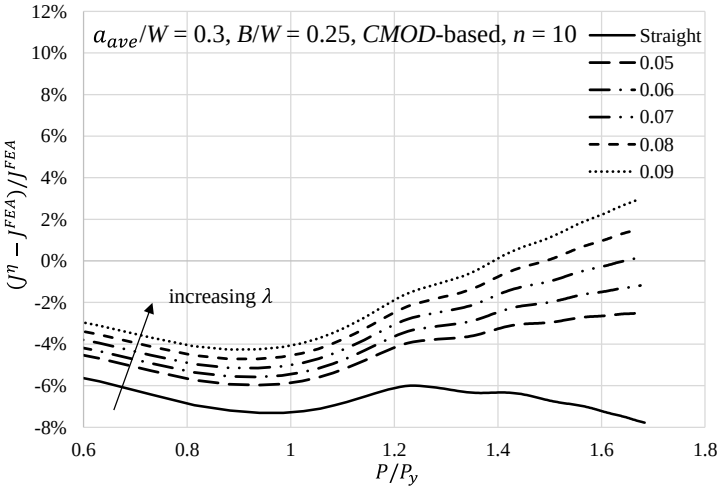
a_{ave}/W = 0.3, B/W = 0.25, *CMOD*-based, n = 10
Straight
0.05
0.06
0.07
0.08
0.09
increasing λ
$(J^n - J^{FEA})/J^{FEA}$
P/P_y
12%
10%
8%
6%
4%
2%
0%
-2%
-4%
-6%
-8%
0.6
0.8
1
1.2
1.4
1.6
1.8

(g)

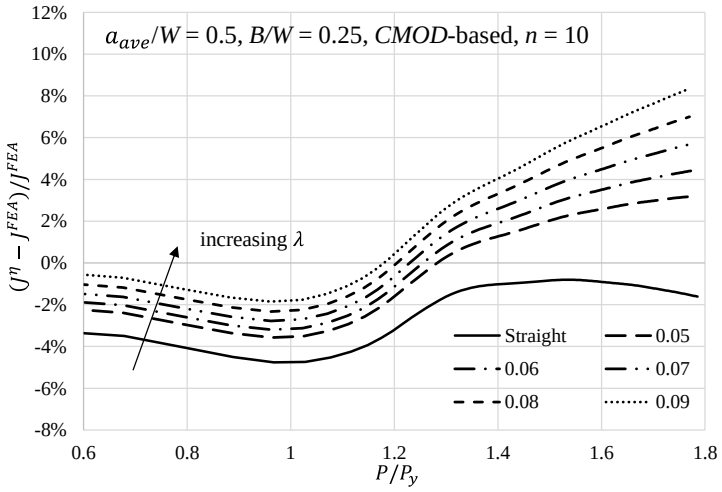
a_{ave}/W = 0.5, B/W = 0.25, *CMOD*-based, n = 10
increasing λ
Straight
0.05
0.06
0.07
0.08
0.09
$(J^n - J^{FEA})/J^{FEA}$
P/P_y
12%
10%
8%
6%
4%
2%
0%
-2%
-4%
-6%
-8%
0.6
0.8
1
1.2
1.4
1.6
1.8

(h)

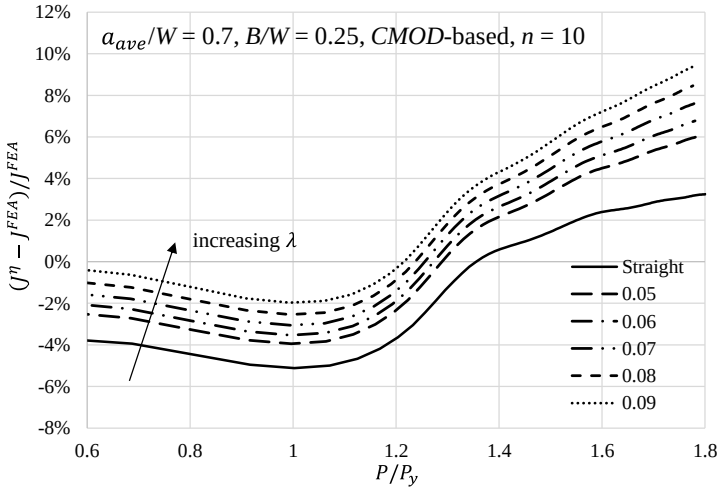

(i)

Figure 3.3. Variation of the error $e_J = (J^{\eta} - J^{FEA})/J^{FEA}$ against P/P_y for specimens with different values of a_{ave}/W, B/W and crack fronts curvature λ (*CMOD*-based analysis, p = 3 and n = 10)

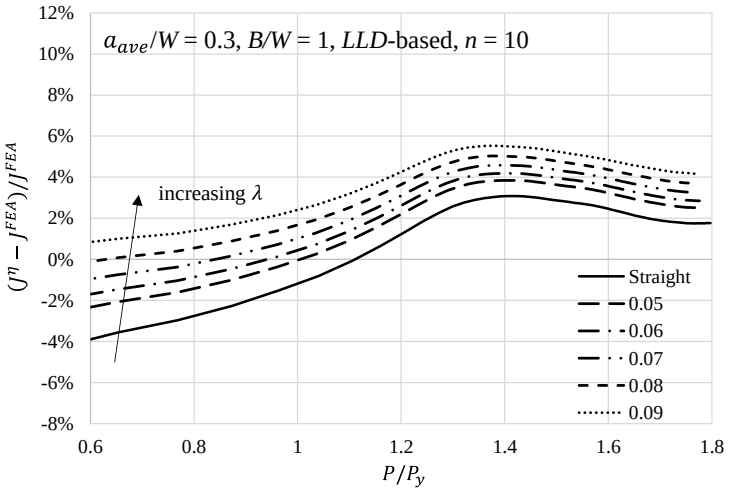
a_{ave}/W = 0.3, B/W = 1, *LLD*-based, n = 10
increasing λ
Straight
0.05
0.06
0.07
0.08
0.09
$(J^{\eta} - J^{FEA})/J^{FEA}$
P/P_y

(a)

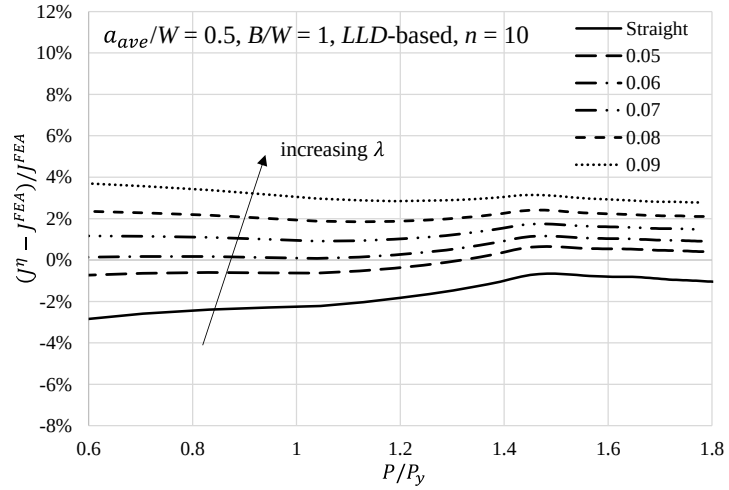
a_{ave}/W = 0.5, B/W = 1, *LLD*-based, n = 10
increasing λ
Straight
0.05
0.06
0.07
0.08
0.09
$(J^{\eta} - J^{FEA})/J^{FEA}$
P/P_y

(b)

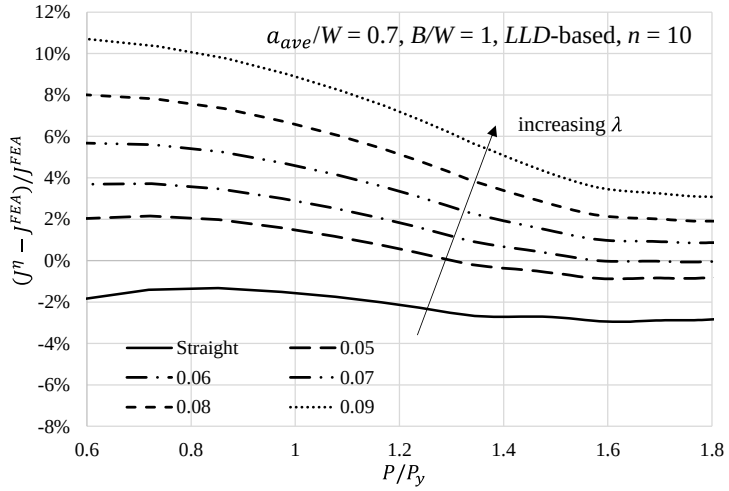
a_{ave}/W = 0.7, B/W = 1, *LLD*-based, n = 10
increasing λ
Straight
0.05
0.06
0.07
0.08
0.09
$(J^{\eta} - J^{FEA})/J^{FEA}$
P/P_y

(c)

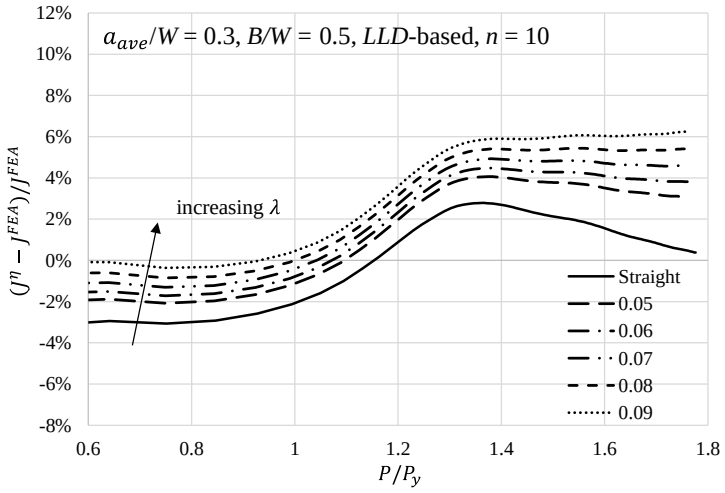
a_{ave}/W = 0.3, B/W = 0.5, *LLD*-based, n = 10
increasing λ
Straight
0.05
0.06
0.07
0.08
0.09
$(J^n - J^{FEA})/J^{FEA}$
P/P_y

(d)

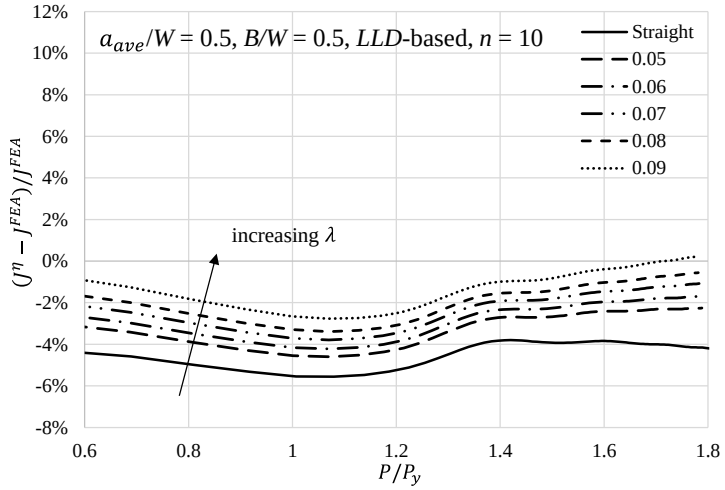
a_{ave}/W = 0.5, B/W = 0.5, *LLD*-based, n = 10
increasing λ
Straight
0.05
0.06
0.07
0.08
0.09
$(J^n - J^{FEA})/J^{FEA}$
P/P_y

(e)

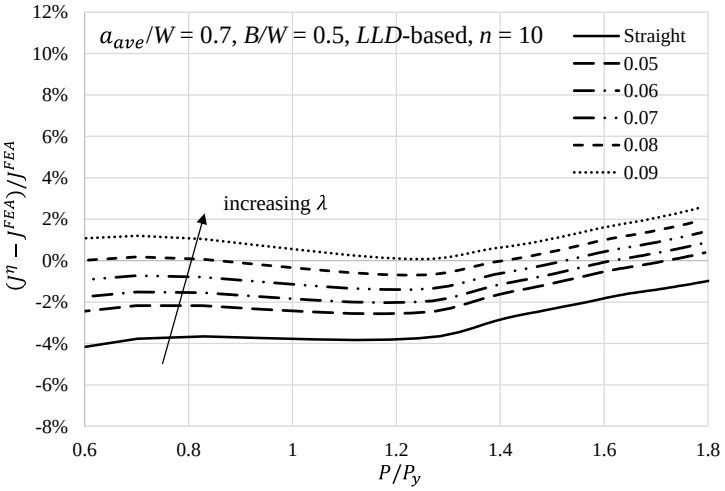
a_{ave}/W = 0.7, B/W = 0.5, *LLD*-based, n = 10
increasing λ
Straight
0.05
0.06
0.07
0.08
0.09
$(J^n - J^{FEA})/J^{FEA}$
P/P_y

(f)

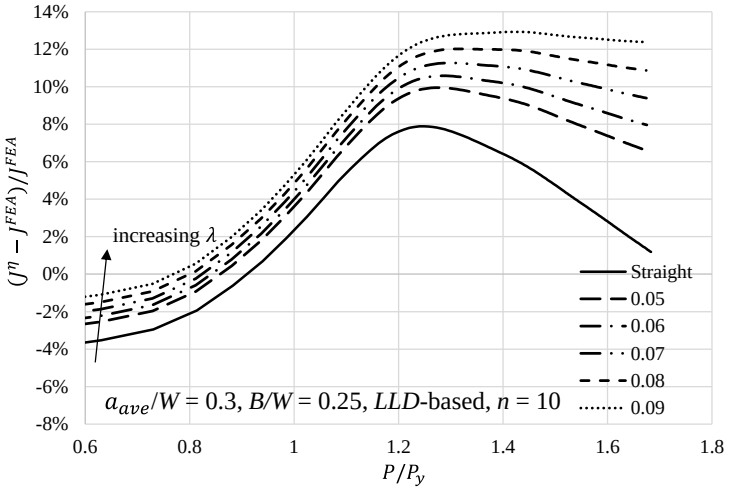
14%
12%
10%
8%
6%
4%
2%
0%
-2%
-4%
-6%
-8%
0.6
0.8
1
1.2
1.4
1.6
1.8
P/P_y
$(J^n - J^{FEA})/J^{FEA}$
increasing λ
a_{ave}/W = 0.3, B/W = 0.25, *LLD*-based, n = 10
Straight
0.05
0.06
0.07
0.08
0.09

(g)

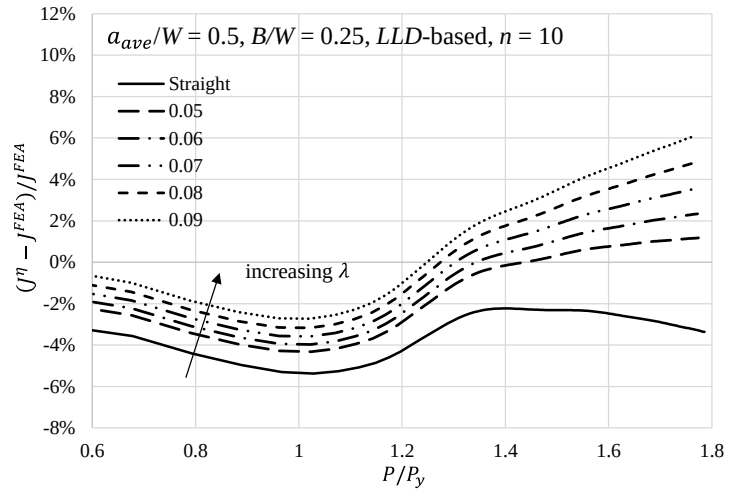
12%
10%
8%
6%
4%
2%
0%
-2%
-4%
-6%
-8%
0.6
0.8
1
1.2
1.4
1.6
1.8
P/P_y
$(J^n - J^{FEA})/J^{FEA}$
a_{ave}/W = 0.5, B/W = 0.25, *LLD*-based, n = 10
Straight
0.05
0.06
0.07
0.08
0.09
increasing λ

(h)

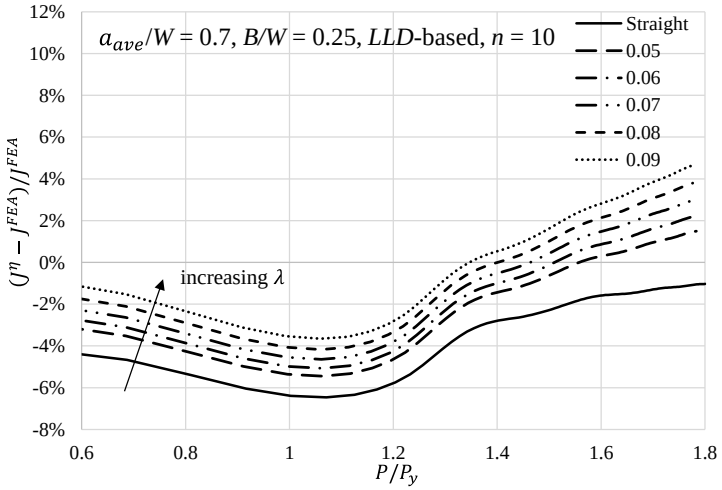

(i)

Figure 3.4. Variation of the error $e_J = (J^{\eta} - J^{FEA})/J^{FEA}$ against P/P_y for specimens with different values of a_{ave}/W, B/W and crack fronts curvature λ (*LLD*-based analysis, p = 3 and n = 10)

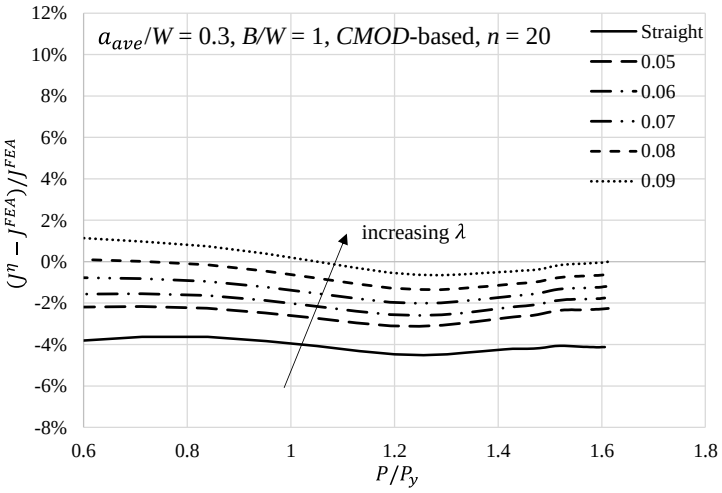
a_{ave}/W = 0.3, B/W = 1, *CMOD*-based, n = 20
Straight
0.05
0.06
0.07
0.08
0.09
increasing λ
$(J^n - J^{FEA})/J^{FEA}$
P/P_y

(a)

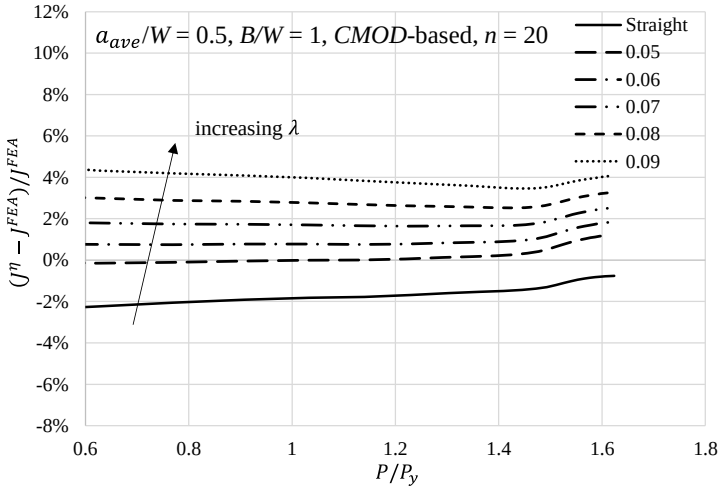
a_{ave}/W = 0.5, B/W = 1, *CMOD*-based, n = 20
Straight
0.05
0.06
0.07
0.08
0.09
increasing λ
$(J^n - J^{FEA})/J^{FEA}$
P/P_y

(b)

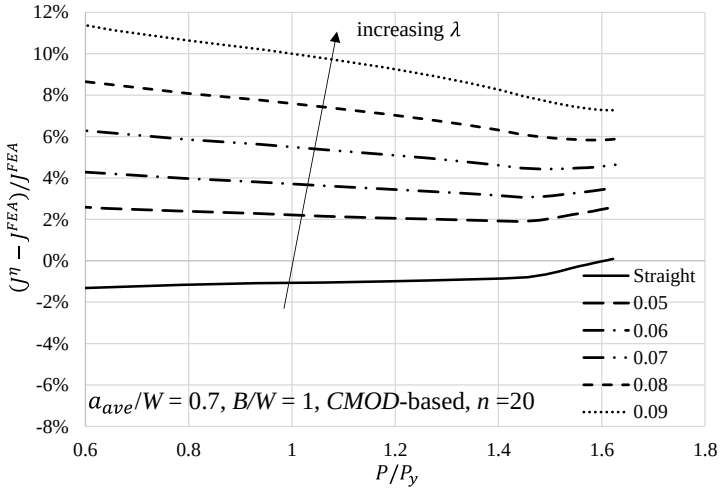
a_{ave}/W = 0.7, B/W = 1, *CMOD*-based, n =20
Straight
0.05
0.06
0.07
0.08
0.09
increasing λ
$(J^n - J^{FEA})/J^{FEA}$
P/P_y

(c)

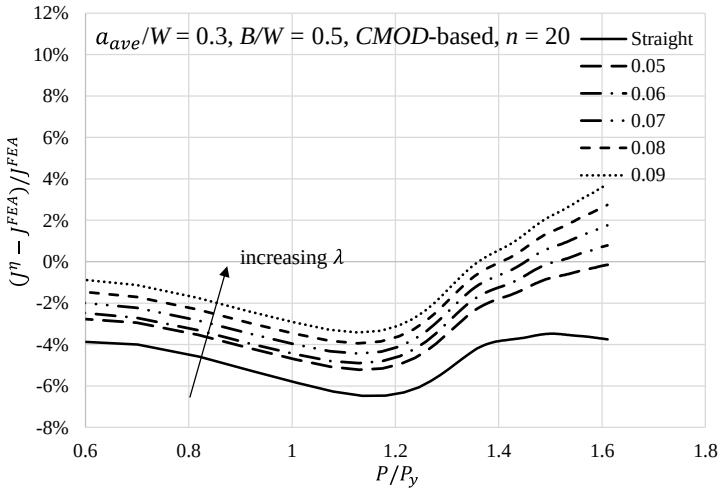
a_{ave}/W = 0.3, B/W = 0.5, *CMOD*-based, n = 20
Straight
0.05
0.06
0.07
0.08
0.09
increasing λ
$(J^n - J^{FEA})/J^{FEA}$
P/P_y
12%
10%
8%
6%
4%
2%
0%
-2%
-4%
-6%
-8%
0.6
0.8
1
1.2
1.4
1.6
1.8

(d)

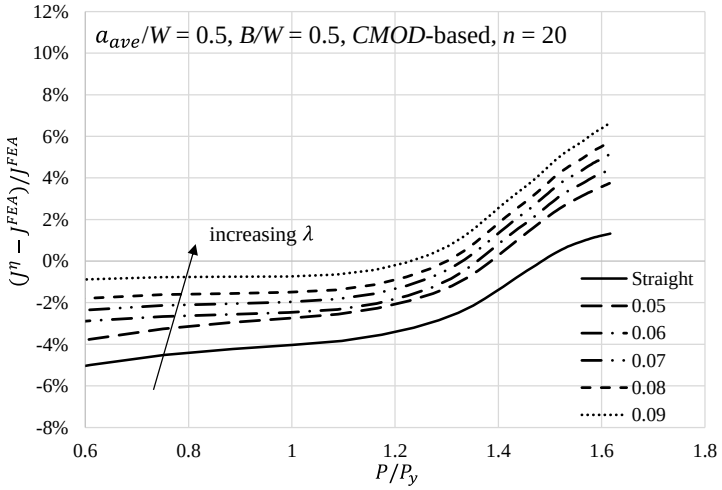
a_{ave}/W = 0.5, B/W = 0.5, *CMOD*-based, n = 20
increasing λ
Straight
0.05
0.06
0.07
0.08
0.09
$(J^n - J^{FEA})/J^{FEA}$
P/P_y
12%
10%
8%
6%
4%
2%
0%
-2%
-4%
-6%
-8%
0.6
0.8
1
1.2
1.4
1.6
1.8

(e)

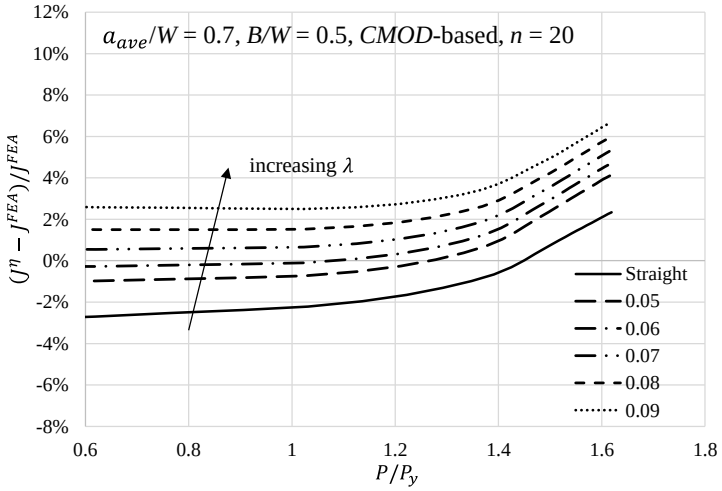
a_{ave}/W = 0.7, B/W = 0.5, *CMOD*-based, n = 20
increasing λ
Straight
0.05
0.06
0.07
0.08
0.09
$(J^n - J^{FEA})/J^{FEA}$
P/P_y
12%
10%
8%
6%
4%
2%
0%
-2%
-4%
-6%
-8%
0.6
0.8
1
1.2
1.4
1.6
1.8

(f)

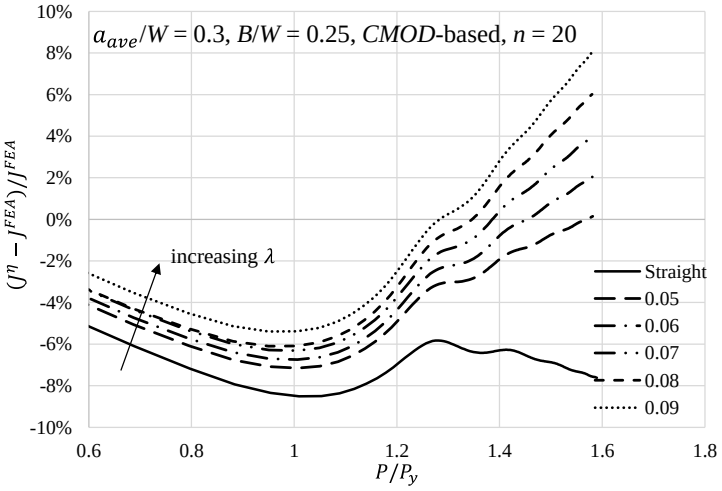
a_{ave}/W = 0.3, B/W = 0.25, *CMOD*-based, n = 20
increasing λ
Straight
0.05
0.06
0.07
0.08
0.09
$(J^n - J^{FEA})/J^{FEA}$
P/P_y

(g)

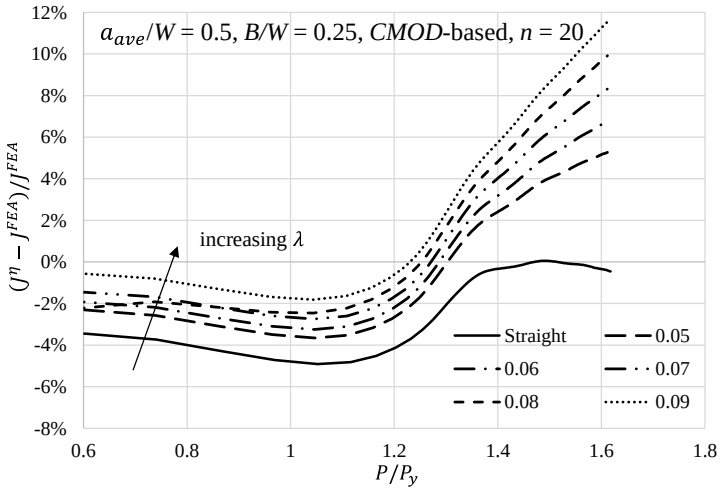
a_{ave}/W = 0.5, B/W = 0.25, *CMOD*-based, n = 20
increasing λ
Straight
0.05
0.06
0.07
0.08
0.09
$(J^n - J^{FEA})/J^{FEA}$
P/P_y

(h)

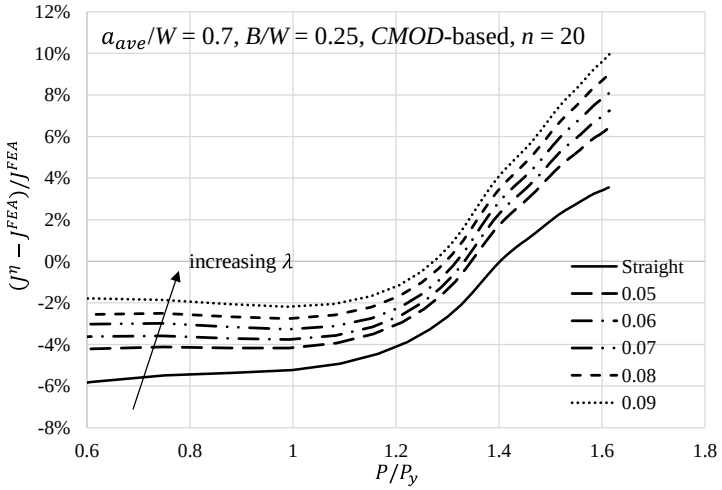

(i)

Figure 3.5. Variation of the error $e_J = (J^{\eta} - J^{FEA})/J^{FEA}$ against P/P_y for specimens with different values of a_{ave}/W, B/W and crack fronts curvature λ (*CMOD*-based analysis, p = 3 and n = 20)

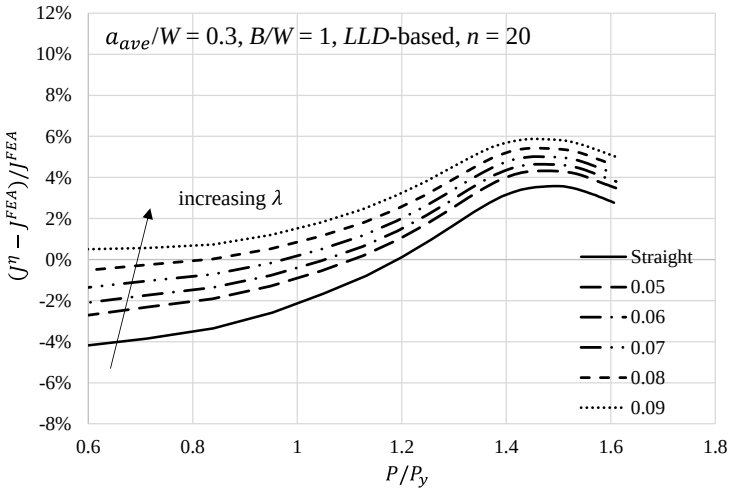
a_{ave}/W = 0.3, B/W = 1, *LLD*-based, n = 20
increasing λ
Straight
0.05
0.06
0.07
0.08
0.09
$(J^n - J^{FEA})/J^{FEA}$
P/P_y
12%
10%
8%
6%
4%
2%
0%
-2%
-4%
-6%
-8%
0.6
0.8
1
1.2
1.4
1.6
1.8

(a)

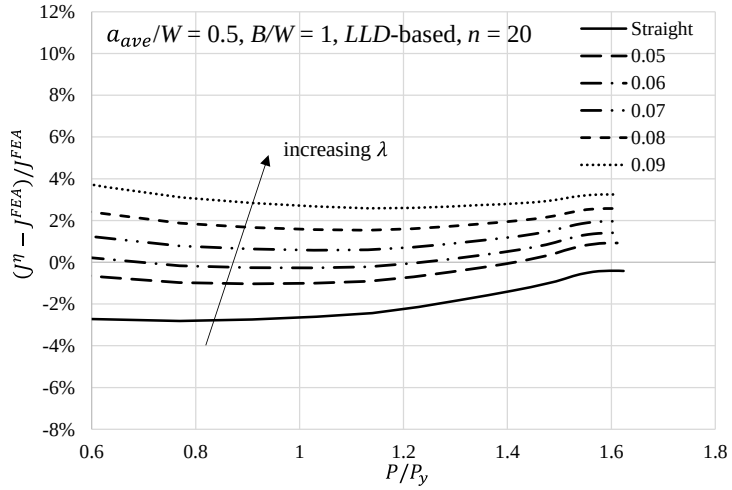
a_{ave}/W = 0.5, B/W = 1, *LLD*-based, n = 20
increasing λ
Straight
0.05
0.06
0.07
0.08
0.09
$(J^n - J^{FEA})/J^{FEA}$
P/P_y
12%
10%
8%
6%
4%
2%
0%
-2%
-4%
-6%
-8%
0.6
0.8
1
1.2
1.4
1.6
1.8

(b)

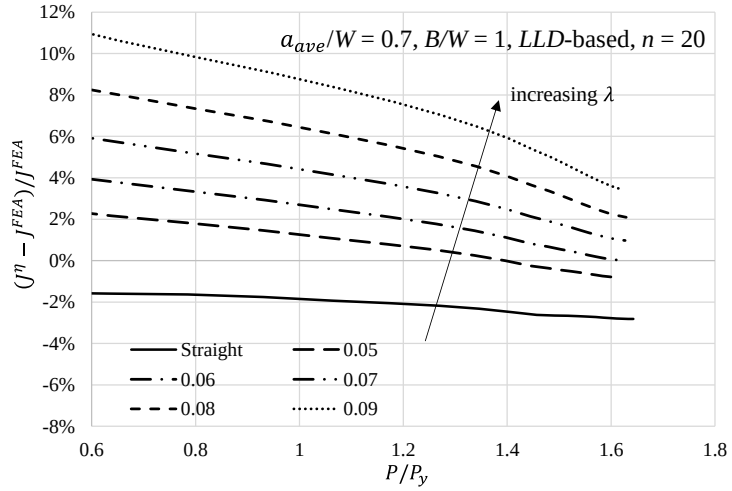
a_{ave}/W = 0.7, B/W = 1, *LLD*-based, n = 20
increasing λ
Straight
0.05
0.06
0.07
0.08
0.09
$(J^n - J^{FEA})/J^{FEA}$
P/P_y
12%
10%
8%
6%
4%
2%
0%
-2%
-4%
-6%
-8%
0.6
0.8
1
1.2
1.4
1.6
1.8

(c)

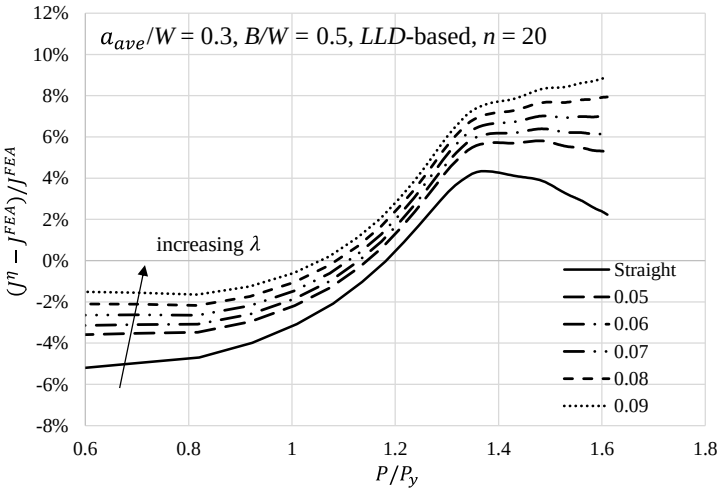
a_{ave}/W = 0.3, B/W = 0.5, *LLD*-based, n = 20
increasing λ
Straight
0.05
0.06
0.07
0.08
0.09
$(J^n - J^{FEA})/J^{FEA}$
P/P_y

(d)

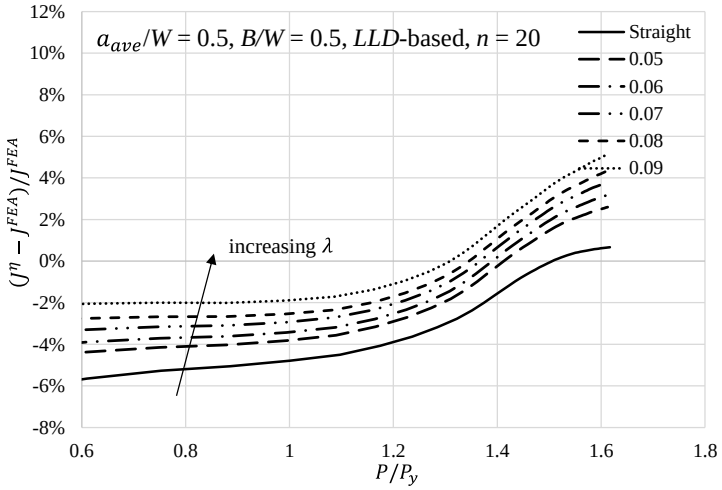
a_{ave}/W = 0.5, B/W = 0.5, *LLD*-based, n = 20
increasing λ
Straight
0.05
0.06
0.07
0.08
0.09
$(J^n - J^{FEA})/J^{FEA}$
P/P_y

(e)

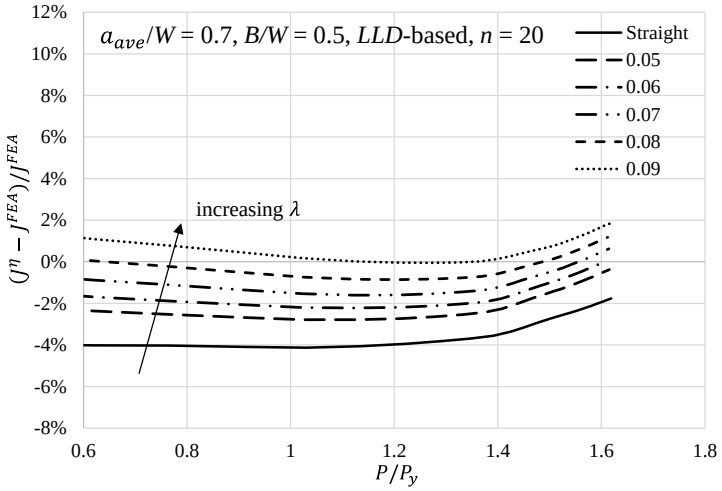
a_{ave}/W = 0.7, B/W = 0.5, *LLD*-based, n = 20
increasing λ
Straight
0.05
0.06
0.07
0.08
0.09
$(J^n - J^{FEA})/J^{FEA}$
P/P_y

(f)

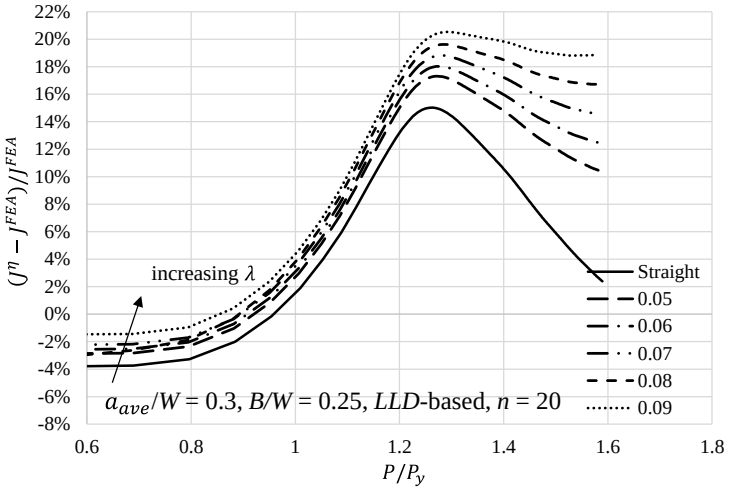
22%
20%
18%
16%
14%
12%
10%
8%
6%
4%
2%
0%
-2%
-4%
-6%
-8%
0.6
0.8
1
1.2
1.4
1.6
1.8
P/P_y
$(J^n - J^{FEA})/J^{FEA}$
increasing λ
a_{ave}/W = 0.3, B/W = 0.25, *LLD*-based, n = 20
Straight
0.05
0.06
0.07
0.08
0.09

(g)

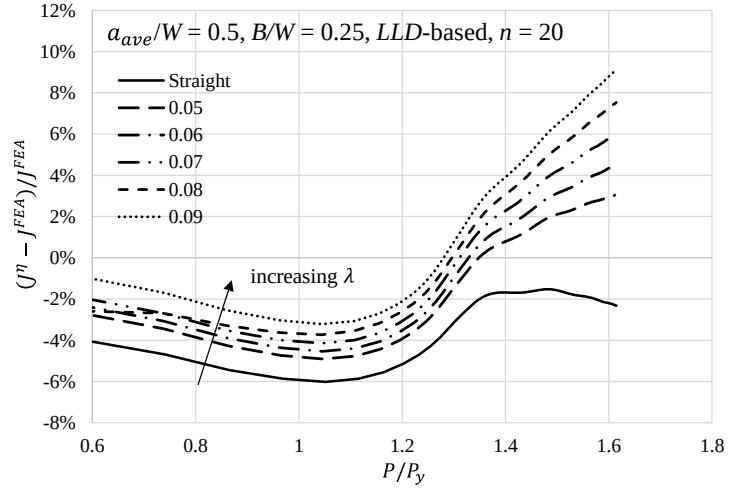
12%
10%
8%
6%
4%
2%
0%
-2%
-4%
-6%
-8%
0.6
0.8
1
1.2
1.4
1.6
1.8
P/P_y
$(J^n - J^{FEA})/J^{FEA}$
a_{ave}/W = 0.5, B/W = 0.25, *LLD*-based, n = 20
Straight
0.05
0.06
0.07
0.08
0.09
increasing λ

(h)

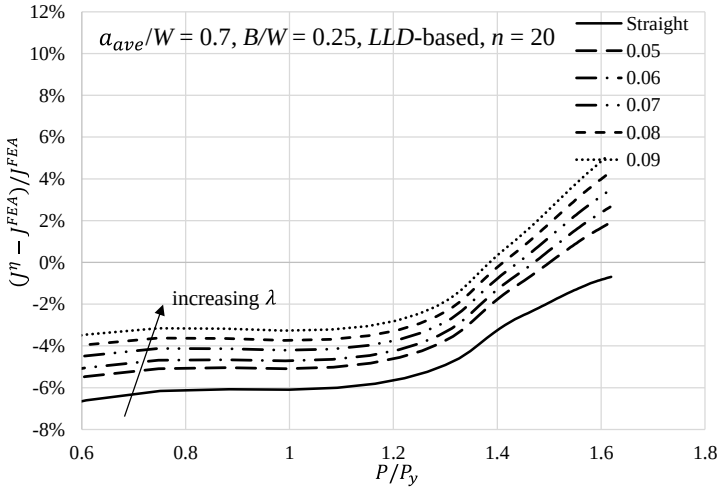

(i)

Figure 3.6. Variation of the error $e_J = (J^{\eta} - J^{FEA})/J^{FEA}$ against P/P_y for specimens with different values of a_{ave}/W, B/W and crack fronts curvature λ (*LLD*-based analysis, p = 3 and n = 20)

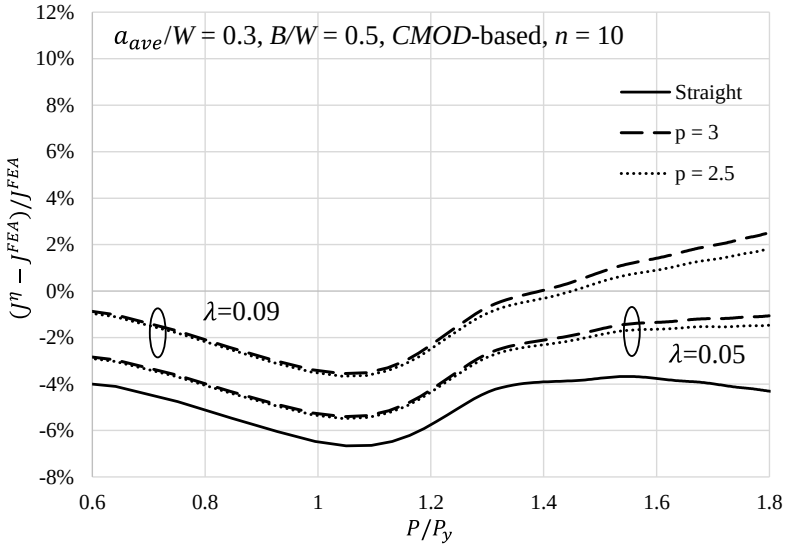
a_{ave}/W = 0.3, *B/W* = 0.5, *CMOD*-based, *n* = 10
Straight
p = 3
p = 2.5
λ=0.09
λ=0.05
12%
10%
8%
6%
4%
2%
0%
-2%
-4%
-6%
-8%
0.6
0.8
1
1.2
1.4
1.6
1.8
$(J^n - J^{FEA})/J^{FEA}$
P/P_y

(a)

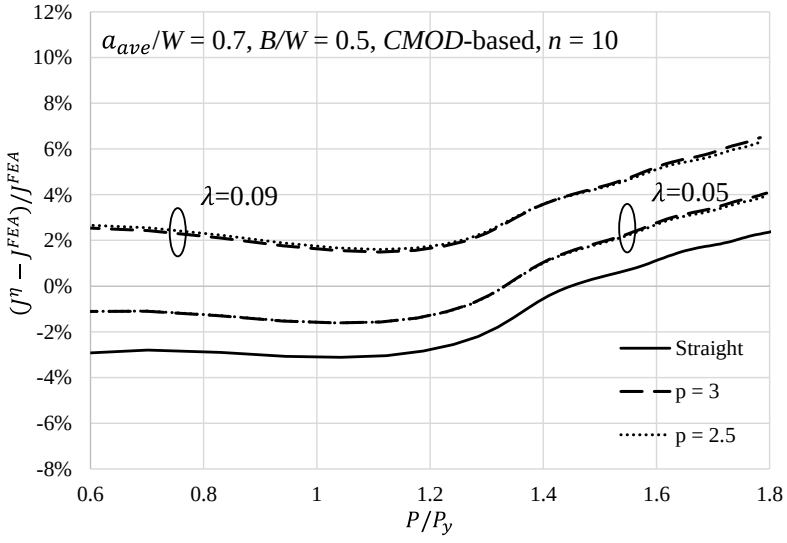
a_{ave}/W = 0.7, *B/W* = 0.5, *CMOD*-based, *n* = 10
λ=0.09
λ=0.05
Straight
p = 3
p = 2.5
12%
10%
8%
6%
4%
2%
0%
-2%
-4%
-6%
-8%
0.6
0.8
1
1.2
1.4
1.6
1.8
$(J^n - J^{FEA})/J^{FEA}$
P/P_y

(b)

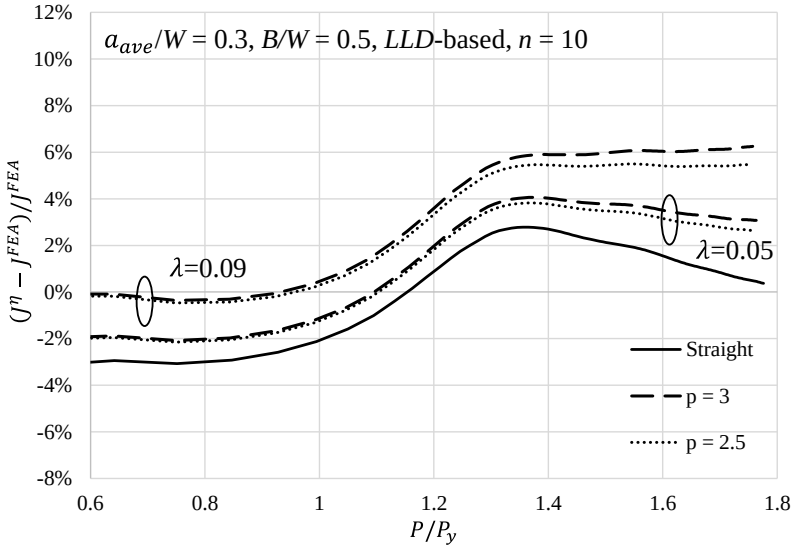

(c)

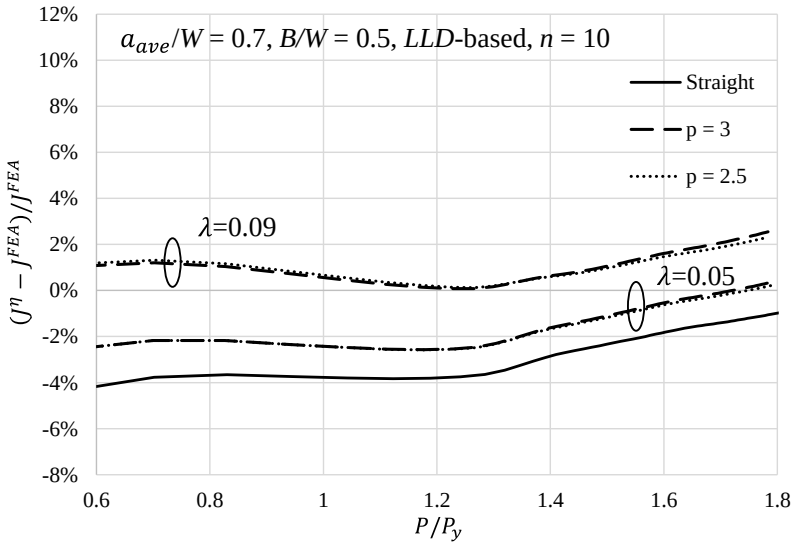

(d)

Figure 3.7. Impact of the shape parameter p (p = 3 and p = 2.5) on e_J

Chapter 4 Accuracy of the Double Clip-on Gauge Method for Evaluating *CTOD* from Single-edge Tension Specimens

4.1 Introduction

4.1.1 Experimental Determination of *CTOD*

The crack tip opening displacement (*CTOD*) is a widely used parameter for characterizing the fracture toughness of ductile materials and a key input in the integrity assessment of structures containing flaws. For instance, the *CTOD* concept could be used directly to calculate the tolerable flaw sizes or as a *CTOD* design curve to determine the allowable crack sizes in welded structures (Burdekin and Dawes, 1971; BSI, 2005). In the strain-based design of energy pipelines, *CTOD* can be employed to evaluate the tensile strain capacity of the pipeline (Fairchild et al., 2012).

There are currently two main approaches to determine *CTOD* experimentally from small-scale specimens. The first approach is based on the fact that *CTOD* (δ) can be uniquely related to the J-integral (J) (Shih, 1981; Anderson, 2005) as $\delta = J/m\sigma_0$, where m is the so-called (dimensionless) constraint parameter (Shih, 1981; Kirk and Dodds, 1993), and σ_0 is a reference stress (e.g. yield strength) of the material. The above *J-CTOD* is widely used to determine *CTOD* indirectly from J using both the standard single-edge bend (SE(B) and compact tension (C(T))) specimens (ASTM, 2008; ASTM, 2011) as well as the non-standard single-edge tension (SE(T)) specimens (Shen and Tyson, 2009a; Ruggieri, 2012). The value of J can be evaluated from the experimentally measured load-displacement curve through a plastic geometry factor, η_{pl} (see Section 3.1.1). It follows that by adopting this method the accuracy of the determined *CTOD* is largely governed by the accuracy of the two dimensionless parameters, i.e. m and η_{pl}, both of which are functions of the specimen geometry and material properties (ASTM, 2008; Shen and Tyson, 2009a; Moreira and Donato, 2010; ASTM, 2011; Ruggieri, 2012; DNV, 2013).

Compared with the indirect method, the plastic component of *CTOD* can be determined directly from the measured crack mouth opening displacement (*CMOD*) by

employing a plastic hinge model assuming two halves of the specimen rotate rigidly about a rotational center (i.e. plastic hinge) during tests (see Fig. 4.1), as specified in BS 7448 (BSI, 1991) and ISO 12135 (ISO, 2002) for bend specimens. The *CTOD* values can then be determined from the following equation:

$$\delta_{BS} = \delta_{el} + \delta_{pl} = \frac{K^2(1-\nu^2)}{2E\sigma_{YS}} + \frac{r_p(W-a_0)V_{pl}}{r_p(W-a_0)+a_0+z} \tag{4.1}$$

where δ_{BS} is *CTOD* determined according to BS 7448; δ_{el} is the elastic component of *CTOD*, which can be calculated from the stress intensity factor, *K*; δ_{pl} denotes the plastic component of *CTOD* and is evaluated from the plastic component of the measured *CMOD*, V_{pl}, by assuming a plastic hinge model as illustrated in Fig. 4.1, and *W*, a_0, *v*, *E* and σ_{YS} are the specimen width, original crack length, Poisson's ratio, Young's modulus and the yield strength of the material, respectively. The parameter r_p in Fig. 4.1 is a dimensionless rotation factor. Wu et al. (1988a; 1988b) employed the limit load analysis to derive $r_p \approx 0.44$ for deeply-cracked SE(B) specimens and $r_p \approx 0.46$ for C(T) specimens. The values of r_p adopted by BS 7448 for SE(B) and C(T) specimens with $a_0/W = 0.45 - 0.55$ are 0.4 and 0.46, respectively. However, similar to *m* and η_{pl}, r_p is usually load-, geometry- and material-dependent (Donato and Ruggieri, 2006; Cravero and Ruggieri, 2007).

The double clip-on gauge (DCG) method (Deng et al., 1980; Willoughby and Garwood, 1983) was first proposed in the 1980s as an alternative method to experimentally determine *CTOD*. As shown in Fig. 4.2, a pair of specially-designed knife edges are used to adapt two clip-on gauges at different heights above the specimen surface, which can simultaneously measure two values of *CMOD* at the two heights. Based on certain simplifying assumptions, *CTOD* can then be related to the two directly measured *CMOD* values through a simple geometric relationship, and the details will be presented in Section 4.2. The advantage of the DCG method is that it is based on the physical deformation of the crack tip and simple geometric relationship, and does not involve the evaluation of *J* or assumption of the location of the plastic hinge as required in the plastic hinge model.

4.1.2 Single-edge Tension Specimen

Previous studies (e.g. Brocks and Schmitt, 1995) have shown that the fracture toughness resistance curve (i.e. *J-R* and *CTOD-R* curves) determined from small-scale test specimens are dependent on the specimen geometric configurations and/or the type of loading (e.g. bending or tension) applied to the specimen. This phenomenon is largely due to the so-called crack-tip constraint effect, which is a measure of the resistance to the plastic flow (Brocks and Schmitt, 1995). Generally, a high level of the crack-tip constraint results in a low resistance curve because a high level of constraint restricts the plastic deformation and associated energy dissipation in the vicinity of the crack tip and therefore lowers the resistance to fracture (Brocks and Schmitt, 1995; Kim et al., 2004). The standard fracture toughness test specimens such as those specified in ASTM E1820-11 and BS 7448 are deeply-cracked, predominantly bend-loaded specimens with high crack-tip constraint levels such that conservative measurements of fracture toughness are obtained from such specimens.

Figure 4.3 schematically shows four typical toughness resistance curves obtained from different types of test specimens including C(T), deeply- (i.e. $a/W \geq 0.45$) and shallow-cracked (i.e. $a/W < 0.45$) SE(B) and SE(T) specimens, where a and W are the crack length and specimen width, respectively. Due to the similar loading conditions and crack-tip constraint levels between the SE(T) specimen and the full-scale pipeline containing surface cracks under longitudinal tension (Chiesa et al., 2001; Kibey et al., 2009; Shen and Tyson, 2009a; Kibey et al., 2010; Moore and Pisarski, 2012), there are increasing interests in using the non-standard SE(T) specimen to determine the toughness resistance curve in the pipeline industry over the last decade. The growing interests in the SE(T) specimen are the main motivation for the present study. There are two types of SE(T) specimens: pin-ended and clamp-ended specimens. The latter is considered more relevant than the former to the full-scale pipe in terms of the crack-tip stress and strain fields (Shen et al., 2008).

4.1.3 Literature Review

Tang et al. (2010) examined the applicability of the DCG method for SE(T) specimens by carrying out two-dimensional (2D) plane strain finite element analyses (FEA). The crack propagation was simulated in the analysis. They reported that the *CTOD* values obtained from the DCG method agree well with the corresponding values directly obtained from FEA. Moore and Pisarski (2012) investigated the accuracy of the DCG method experimentally by comparing the *CTOD* values obtained from DCG with those measured from the specimen notch replicas. They reported that the *CTOD* values measured using DCG agree well with the physical measurements taken from the notch replicas with errors being less than 10% if a/W is in the range of 0.3 to 0.5. Note that in Moore and Pisarski's study only the *CTOD* values corresponding to the last loading step in the experiment were examined. Note further that in the aforementioned two studies, *CTOD* was defined as the opening length of the original crack tip before blunting, which is different from the commonly used 90 º intersect definition of *CTOD* (Shih, 1981). These two *CTOD* definitions are schematically illustrated in Fig. 4.4.

4.1.4 Objective and Approach

In the study reported in this chapter, we aimed to investigate the impact of the specimen thickness-to-width ratio, crack length, side-grooving, stain hardening characteristics of the material and loading level on the accuracy of the DCG method for the clamped SE(T) specimen. To this end, systematic three-dimensional (3D) finite element analyses of clamped SE(T) specimens with wide ranges of the crack length and thickness-to-width ratio were carried out. The commonly used 90 ºintersect definition of *CTOD* was adopted in this study and is denoted by $CTOD_{90}$ or δ_{90}. The geometric relationship in the vicinity of the deformed crack tip that is key to the DCG method was examined. Based on the analysis results, the existing equation for evaluating *CTOD* based on the DCG method was slightly modified to improve the accuracy of the *CTOD* evaluation. This study will facilitate the application of the fracture toughness determined from the SE(T) specimen in the strain-based design of pipelines.

The rest of this chapter is organized as follows. A brief illustration of the DCG method for evaluating $CTOD_{90}$ is included in Section 4.2; the 3D FEA models and analysis procedures are described in Section 4.3; Section 4.4 shows the analysis results and modification of the existing DCG-based equation for evaluating $CTOD_{90}$, and the summary and concluding remarks are presented in Section 4.5.

4.2 *CTOD* Measured from Double Clip-on Gauge Method

A detailed geometry near the crack tip in the context of the double clip-on gauge method was developed and shown in Fig. 4.5, where point *O* is the deformed crack tip and *OB* is the 45° interception line used to determine $CTOD_{90}$. The following equation can be derived from the geometric relationships shown in Fig. 4.5 to evaluate *CTOD* considering similar triangles between *BEF* and *FHG*:

$$\begin{cases} \delta_{DC90} = \frac{V_1 - 2(a_0 + z_1)\sin\theta}{1 - \sqrt{2}\sin\theta\cos(45^\circ - \theta)} \\ \sin\theta = \frac{V_2 - V_1}{2(z_2 - z_1)} \end{cases} \tag{4.2}$$

where V_1 and V_2 are the two measured crack mouth opening displacements corresponding to two different knife edge heights z_1 and z_2, respectively (see Figs. 4.2 and 4.5); a_0 is the initial crack length, and δ_{DC90} denotes the *CTOD* value obtained from the double clip-on gauge method here. Generally the angle θ is small such that Eq. (4.2) can be simplified as:

$$\delta_{DC90} = V_1 - \frac{(a_0 + z_1)(V_2 - V_1)}{z_2 - z_1} \tag{4.3}$$

Equation (4.3) is the same as that used by Tang et al. (2010), although they adopted a different definition of *CTOD*.

In a previous (2000) version of DNV-OS-F101 (2000), δ_{DC90} is separated into an elastic component and a plastic component as follows:

$$\delta_{DC90} = \frac{(1 - \nu^2)K^2}{2E\sigma_{YS}} + V_{pl1} - \frac{(a_0 + z_1)(V_{pl2} - V_{pl1})}{z_2 - z_1} \tag{4.4}$$

where the first term on the right hand side of Eq. (4.4) is the elastic component of δ_{DC90} and evaluated from the stress intensity factor, K; the evaluation of K is well documented for SE(T) specimens (e.g. Tada et al., 1973; Shen and Tyson, 2009b); the second and third terms on the right hand side of Eq. (4.4) are the plastic component of δ_{DC90}, and V_{pl1} and V_{pl2} are the plastic components of the two measured *CMOD* values. The accuracy of both Eqs. (4.2) and (4.4) was examined in this study.

4.3 Finite Element Analyses

4.3.1 Finite Element Model

The commercial software package ADINA 8.7.4 (ADINA, 2012) was used to carry out the 3D finite element analyses. Both plane-sided and side-grooved clamped SE(T) specimens were modeled in this study. The plane-sided specimens were considered as baseline cases, whereas the side-grooved specimens were employed to investigate the impact of the side grooves on the analysis. All the specimens considered in this study have the same width (W = 20 mm) and daylight length ($H = 10W$) (see Fig. 2.1d) (DNV, 2006; Shen et al., 2008; Shen and Tyson, 2009a), but five different relative crack lengths, i.e. a/W = 0.3 to 0.7 with an increment of 0.1, and three different thickness-to-width ratios, i.e. B/W = 0.5, 1 and 2, where B is the specimen thickness. For side-grooved specimens, the depth of the side groove on each side was selected to be 7.5%B (Shen et al. 2010).

Because of symmetry, only a quarter of the specimen was modeled using 8-node 3D isoparametric brick elements (ADINA, 2012). The model was divided into 17 and 25 layers in the thickness direction for plane-sided and side-grooved models, respectively, with the mesh density increasing from the mid-plane to the free surface to capture the high stress gradients near the free surface. The side groove is modelled as a sharp V-notch with an opening angle of 45 °. The geometric and mesh configurations for a typical specimen are shown in Fig. 4.6, and a side-grooved model with a/W = 0.5 and B/W = 1 is schematically shown in Fig. 4.7.

The J_2 incremental theory of plasticity (Lubliner, 2008) and large-displacement large (finite) strain formulation (Anderson, 2005; ADINA, 2012) were employed in FEA. In ADINA, the large-displacement large-strain formulation requires input of the Cauchy (true) stress-logarithmic (true) strain relationship and outputs the Cauchy stress and deformation gradient. A blunt crack tip with initial radii (ρ_0) of 2.5, 5 and 10 μm was incorporated in the model to simulate the crack-tip blunting during the loading process and facilitate convergence of the large-displacement large (finite) strain analysis (McMeeking and Parks, 1979; Dodds, 2009; ADINA, 2012). The first value of ρ_0 is the baseline case that applies to all the specimens considered, whereas the latter two values were employed for selected geometric configurations only (i.e. $B/W = 1$ and $a/W = 0.5$) to investigate the impact of the initial crack tip radius on the accuracy of the DCG method. Note that for the side-grooved specimens, the blunt crack tip is also prepared through the thickness of the side groove as shown in Fig. 4.7 to mitigate the impact of the singularity caused by the 45° sharp V-notch under tension on the finite strain analysis. The mesh surrounding the crack tip consists of 40 concentric semicircles. In the vicinity of the crack tip, the minimum in-plane size of the elements closest to the crack tip is about 1/10 of the crack-tip radius (Qian and Dodds, 2006; Graba and Galkiewicz, 2007), whereas the in-plane size of the elements in the outermost ring (i.e. 40th ring) is about 2,000 times that of the element closest to the crack tip (Dodds, 2009). The aspect ratio of these elements is less than 7. The total number of elements is approximately 32,000 for a typical plane-sided model and 50,000 for a side-grooved model. Stationary cracks were assumed in the present analysis. Convergence studies on mesh density, e.g. refine the mesh surrounding the crack tip or separate the specimen into more layers, were conducted and showed good convergence in this elastic-plastic analyses.

4.3.2 Material Model

The uniaxial stress-strain relationship of the material is described using an elastic-power-law plastic expression as follows:

$$\frac{\varepsilon}{\varepsilon_0} = \begin{cases} \frac{\sigma}{\sigma_0}, & \varepsilon \le \varepsilon_0 \\ \left(\frac{\sigma}{\sigma_0}\right)^n, & \varepsilon > \varepsilon_0 \end{cases} \tag{4.5}$$

where σ_0 is the reference stress; ε_0 is the reference strain, $\varepsilon_0 = \sigma_0/E$; n denotes the strain hardening exponent of the material. In this study $\sigma_0 = \sigma_{YS}$ = 520 MPa, E = 200 GPa was selected. Three values of n, namely n = 10, 15 and 20, were considered in this study to investigate the effect of strain hardening exponent on the evaluated *CTOD*. The isotropic hardening rule and associated flow rule were employed in the analysis.

4.3.3 Computational Procedure

All the specimens were loaded by a displacement-controlled load up to the level corresponding to large plastic deformations, i.e. P/P_y = 1.3 (Shen et al., 2009; Wang et al., 2012), through about 5,000 steps, where P is the applied load, and P_y is the reference load defined as $B(W - a)\sigma_Y$ (Shen and Tyson, 2009a). Note that σ_Y is the effective yield strength, defined as $\sigma_Y = (\sigma_{YS} + \sigma_{TS})/2$, where σ_{TS} is the ultimate tensile strength. Applying Considere's necking criterion (Soboyejo, 2003) to Eq. (4.5), one can derive the following equation to evaluate σ_{TS}:

$$\sigma_{TS} = \left(\frac{E{\sigma_0}^{n-1}}{ne}\right)^{1/n} \tag{4.6}$$

where e = 2.71828 is the base of the natural logarithm. Equation (4.6) implies that the yield-to-tensile ratio of the material could be expressed as follows assuming $\sigma_0 = \sigma_{YS}$:

$$\frac{\sigma_{YS}}{\sigma_{TS}} = \left(\frac{ne\sigma_{YS}}{E}\right)^{1/n} \tag{4.7}$$

For material with n = 10, 15 and 20, the corresponding yield-to-tensile ratios are 0.77, 0.86 and 0.91, respectively. The sparse matrix solver was employed for its high efficiency in the numerical analysis (ADINA, 2012). The full Newton-Raphson iteration method was selected to find the solution of nonlinear equations with the maximum number of iterations for each step being 15. The displacement convergence criterion was selected, in which the displacement tolerance equaled 0.001 corresponding to a reference displacement of 1 mm (ADINA, 2012).

As illustrated in Fig. 4.8, due to symmetry, $CTOD_{90}/2$ was evaluated based on the intercept between a straight line at 45° originating from the crack tip in the deformed

position and the deformed crack flank at the mid-plane of the specimen. The interception point was captured using a linear interpolation between two nearest deformed nodes on the deformed flank given the corresponding nodal displacements (Tracey, 1976; Shen and Tyson, 2009a; Ruggieri, 2012). The value of $CTOD_{90}$ obtained from FEA based on this approach is denoted by δ_{FE90} and considered as the true value of *CTOD* in this study.

As shown in Fig. 4.9, the two measured *CMOD*s, i.e. V_1 and V_2, are calculated from the nodal displacements of the two outermost nodes on the deformed crack flank at the mid-plane of the specimen in FEA, i.e. points *M* and *N*, which are corresponding to the two knife edge heights of zero and $-z_2$. Therefore, Eqs. (4.2) and (4.4) can be employed to calculate the double clip-on gauge measured *CTOD*, δ_{DC90}, according to the FEA results. Several other positions of point *N* (shown in Fig. 4.9 as N_i, i = 2, 3, 4, 5) have been analyzed to investigate the impact of the position of point *N* on the value of δ_{DC90}. The analysis results indicate that δ_{DC90} is insensitive to the position of point *N*.

4.4 Results and Discussions

Let $e_1 = (\delta_{DC90} - \delta_{FE90})/\delta_{FE90}$ denote the error of δ_{DC90} evaluated using Eq. (4.4). The values of e_1 are plotted against *P/Py* for plane-sided specimens with the same *B/W* ratio but different *a/W* ratios in Fig. 4.10 and for plane-sided specimens with the same *a/W* ratio but different *B/W* ratios in Fig. 4.11. The figures suggest that once *P/Py* exceeds 0.3, δ_{DC90} can markedly overestimate δ_{FE90}, and when the applied load reaches around 0.9*Py*, the error reaches a peak value of up to 40%. The specimen *B/W* ratio has a negligible impact on e_1. The values of e_1 for specimens with the same *a/W* and *B/W* but different *n* values are shown in Fig. 4.12, which suggests that *n* has a large impact on e_1. Given *a/W*, *B/W* and P/P_y, e_1 decreases as *n* increases from 10 to 20. The errors associated with δ_{DC90} evaluated using Eq. (4.2) (i.e. without separating *CTOD* into the elastic and plastic components) are also evaluated and it is observed that the error is significantly higher than that associated with δ_{DC90} evaluated using Eq. (4.4), with the peak value of e_1 reaching as high as 100%.

The geometric relationship in the vicinity of the deformed crack tip was examined. The main reason attributing to the error in δ_{DC90} is that the idealized geometric

relationship as shown in Fig. 4.5 does not always hold in real situations. Figure 4.13(a) schematically illustrates the geometric relationship in the vicinity of the blunt crack tip according to the FEA results, which indicates that the intersection point between the 45° line from the crack tip and deformed crack flank, i.e. point *D*, is not on the extension of the straight line that connects the two outermost nodes on the deformed crack flank in FEA, i.e. points *M* and *N*. In other words, the assumption that the intersection point *D* is collinear with points *M* and *N* as involved in the DCG method (see Fig. 4.5) does not hold in real conditions. Figure 4.13(a) also clearly shows the relationship between the true $CTOD_{90}$, δ_{FE90}, and the *CTOD* value evaluated using the DCG method. The above observation suggests that although the DCG method is more advantageous than the single clip-on gauge method by avoiding the assumption of the plastic hinge location, the accuracy of the DCG method can be further improved. The relatively large errors associated with the DCG method as reflected in Figs. 4.10 through 4.12 are in contrast to the results reported by Moore and Pisarski (2012), which indicates that the accuracy of the DCG method is within ±10%. Note that the *CTOD* definitions adopted in this study and by Moore and Pisarski (2012) are different; therefore, the difference between the accuracy of the DCG method reported in the two studies suggests that the accuracy is sensitive to the definition of *CTOD*.

To improve the accuracy of *CTOD* measured using the DCG method, a correction factor, μ, as defined in Fig. 4.13(b) by setting $MC' = \mu a_0$, was introduced to modify the initial crack length a_0 used in Eq. (4.2). Equation (4.2) can then be revised as follows by considering similar triangles between *D'EM* and *NFM*:

$$\begin{cases} \delta_{DC90} = \dfrac{V_1 - 2(\mu a_0 + z_1)\sin\theta}{1 - \sqrt{2}\sin\theta\cos(45^\circ - \theta)} \\ \sin\theta = \dfrac{V_2 - V_1}{2(z_2 - z_1)} \end{cases} \tag{4.8}$$

where the correction factor μ can be uniquely determined by setting $\delta_{DC90} = \delta_{FE90}$. The values of μ are plotted against P/P_y for clamped plane-sided SE(T) specimens with ranges of *B/W* and *a/W* ratios in Fig. 4.14. It is observed that μ generally decreases towards unity as P/P_y or *a/W* increases, which means that for deeply-cracked specimens, i.e. point *D* in Fig. 4.13 being far away from points *M* and *N*, the required correction factor, μ is

close to unity. For specimens with *a/W* = 0.5, 0.6 and 0.7, the *B/W* ratio has a negligible impact on μ, and for specimens with *a/W* = 0.3 and 0.4, the maximum difference between μ values corresponding to different *B/W* ratios is about 4%. The values of μ for side-grooved SE(T) specimens with ranges of *B/W* and *a/W* ratios are compared with the results for plane-sided specimens in Fig. 4.15, which indicates that the presence of side grooves has a negligible impact on μ since the *CTOD* values are all measured at the mid-plane.

The impact of the initial blunt crack tip radius in the FEA mesh, ρ_0, on the proposed correction factor μ is also investigated. Based on clamped SE(T) specimens with *a/W* = 0.5 and *B/W* = 1, the values of μ corresponding to three different ρ_0 are depicted in Fig. 4.16, which shows that μ is insensitive to ρ_0. The impact of the strain hardening exponent *n* on the proposed correction factor μ is investigated based on the plane-sided specimens with *a/W* = 0.3 to 0.7 and *B/W* = 1. The values of μ corresponding to *n* = 10, 15 and 20, *a/W* = 0.3 and 0.7 are depicted in Fig. 4.17. The results corresponding to *a/W* = 0.4 to 0.6 are not shown to reduce clutter. Figure 4.17 suggests that μ depends on *n*, especially for shallow-cracked specimens.

In summary, the correction factor is a function of the crack length, applied load level and the yield-to-tensile ratios of the material, and insensitive to the specimen thickness-to-width ratio, side-grooving and initial blunt crack tip radius in the FEA mesh. To facilitate the practical application of μ, the following empirical expression of μ was developed based on the results obtained in this study:

$$\mu = q_0 + q_1\left(P/P_y\right) + q_2\left(P/P_y\right)^2 \tag{4.9}$$

where the fitting coefficients q_0, q_1 and q_2 are functions of *a/W* and σ_{YS}/σ_{TS} given as follows:

$$\begin{cases} q_0 = \left[1.8847 - 0.0147\left(\frac{\sigma_{YS}}{\sigma_{TS}}\right)\right] + \left[-0.9516 + 0.1054\left(\frac{\sigma_{YS}}{\sigma_{TS}}\right)\right]\left(\frac{a}{W}\right) \\ q_1 = \left[-0.2328 - 0.0388\left(\frac{\sigma_{YS}}{\sigma_{TS}}\right)\right] + \left[0.5702 - 0.7958\left(\frac{\sigma_{YS}}{\sigma_{TS}}\right)\right]\left(\frac{a}{W}\right) \\ q_2 = \left[1.1733 - 1.5117\left(\frac{\sigma_{YS}}{\sigma_{TS}}\right)\right] + \left[-1.7971 + 2.5704\left(\frac{\sigma_{YS}}{\sigma_{TS}}\right)\right]\left(\frac{a}{W}\right) \end{cases} \tag{4.10}$$

The fitting error of the equations is generally less than 3%. The error of the DCG method by employing the modified equations, i.e. Eqs. (4.8), (4.9) and (4.10), denoted as e_c, is plotted against P/P_y for specimens with various *a/W*, *B/W* and *n* in Figs. 4.18 through 4.21. These figures indicate that the modified equations can significantly improve the accuracy of *CTOD* evaluated from the DCG method, with e_c being generally within ±10%. It should be noted that Equations (4.9) and (4.10) are applicable for SE(T) specimens with *a/W* values between 0.3 to 0.7 and the yield-to-tensile ratios of the material larger than 0.77.

4.5 Summary and Concluding Remarks

The double clip-on gauge method used to experimentally measure *CTOD* for clamped SE(T) specimen was reviewed, and the accuracy of this method was systematically investigated by carrying out three-dimensional finite element analyses of clamped SE(T) specimens with a wide range of specimen dimensions (*a/W* = 0.3 to 0.7 with an increment of 0.1, and *B/W* = 0.5, 1 and 2). Side-grooved clamped SE(T) specimens were also modeled in this study as sensitivity cases to investigate the impact of the side grooves on the measured *CTOD* values. The commonly-used 90 degree intersection definition of *CTOD* (Shih, 1981) was adopted in this study as opposed to the definition used by Tang et al. (2010) and Moore and Pisarski (2012).

It is observed that the *CTOD* values evaluated using the existing equations based on the *CMOD* measurements obtained from the double clip-on gauges can involve significant errors. This error primarily depends on *a/W*, the material straining hardening characteristic (i.e. *n* or equivalently σ_{YS}/σ_{TS}) and loading level characterized by *P/Py*, and can be as large as 40 - 100%. The specimen *B/W* ratio and side-grooving have a negligible impact on the error. Based on the FEA results obtained in this study, the geometric relationship surrounding the blunt crack tip was investigated and the existing DCG-based equations were modified by introducing a correction factor to the original crack length included in the equation. This correction factor was then fitted as a polynomial function of *a/W*, σ_{YS}/σ_{TS} and P/P_y. The modified equation can significantly improve the accuracy of the *CTOD* evaluated from the double clip-on gauges, with the

error in the estimated *CTOD* values being generally within ±10%. The results will facilitate the application of the *CTOD* values determined from the SE(T) specimen in the strain-based design of pipelines.

Reference

ADINA (2012). *Theory and Modeling Guide*. ADINA R & D Inc., Watertown, MA

Anderson, T. L. (2005). *Fracture Mechanics—Fundamentals and Applications, Third edition*. CRC Press, Boca Raton.

ASTM (2008). *ASTM E1290-08: Standard test method for crack-tip opening displacement (CTOD) fracture toughness measurement*. America Society of Testing and Materials International, West Conshohocken, PA.

ASTM (2011). *ASTM E1820-11: Standard Test Method for Measurement of Fracture Toughness*. America Society of Testing and Materials International, West Conshohocken, PA.

Brocks, W. and Schmitt, W. (1995). The Second Parameter in *J-R* curves: Constraint or Triaxiality. *Constraint Effects in Fracture Theory and Applications: Second Volume*, *ASTM STP 1244*, 209-31.

BSI (1991). *BS 7448: Fracture Mechanics Toughness Tests*. British Standard Institution, London.

BSI (2005). *BS 7910: Guide to methods for assessing the acceptability of flaws in metallic structures*. British Standard Institution, London.

Burdekin, F. M. and Dawes, M. G. (1971). Practical Use of Linear Elastic and Yielding Fracture Mechanics with Particular Reference to Pressure Vessels. *In proceedings, Institution of Mechanical Engineers Conference on Practical Application of Fracture Mechanics to Pressure Vessel Technology*, London, April 3-5, 28-37.

Chiesa, M., Nyhus, B., Skallerud, B. and Thaulow, C. (2001). Efficient Fracture Assessment of Pipelines. A constraint-corrected SENT specimen approach. *Engineering Fracture Mechanics*, 68(5), 527-547.

Cravero, S. and Ruggieri, C. (2007). Estimation Procedure of J Resistance Curves for SE (T) Fracture Specimens Using Unloading Compliance. *Engineering Fracture Mechanics*, 74(17), 2735-2757.

Deng, Z., Chang, C., and Wang, T. (1980). Measuring and Calculating CTOD and the J-integral with a Double Clip Gauge. *Strain*, 16(2), 63-67.

Dodds, R. H. (2009). *WARP3D: Notes on Solution & Convergence Parameters for a Shallow-Notch SE(B) Model*. University of Illinois at Urbana-Champaign, IL.

Donato, G. H. B. and Ruggieri, C. (2006). Estimation Procedure for J and CTOD Fracture Parameters Using Three-point Bend Specimens. *Proceedings of 6th International Pipeline Conference (IPC2006)*, Calgary, Alberta, Canada, September 25-29, Paper Number: IPC2006- 10165.

DNV (2000). *Offshore Standard DNV-OS-F101: Submarine Pipeline Systems*. Det Norske Veritas (superseded).

DNV (2006). *Recommended Practice DNV-RP-F108: Fracture Control for Pipeline Installation Methods Introducing Cyclic Plastic Strain*. Det Norske Veritas.

DNV (2013). *Offshore Standard DNV-OS-F101: Submarine Pipeline Systems*. Det Norske Veritas.

Fairchild, D. P., Kibey, S. A., Tang, H., Krishnan, V. R., Wang, X., Macia, M. L., and Cheng, W. (2012). Continued Advancements Regarding Capacity Prediction of Strain-based Pipelines. *Proceedings of 9th International Pipeline Conference (IPC2012)*, Calgary, Alberta, Canada, September 24–28.

Graba, M. and Galkiewicz, J. (2007) Influence of The Crack Tip Model on Results of The Finite Element Method. *Journal of Theoretical and Applied Mechanics*, 45, 225-237.

Hutchinson, J. W. (1968). Singular Behavior at the End of a Tensile Crack in a Hardening Material. *Journal of the Mechanics of Physics and Solids*, 16, 13-31.

ISO (2002). *ISO 12135: Metallic materials - Unified Method of Tests for Determination of Quasistatic Fracture Toughness*. Geneva, International Organization for Standardization.

Kibey, S. A., Minnaar, K., Cheng, W. and Wang, X. (2009). Development of a Physics-based Approach for the Prediction of Strain Capacity of Welded Pipelines. In *Proceedings of the 19th International Offshore and Polar Engineering (ISOPE) Conference*, Osaka, Japan, 21-26.

Kibey, S., Wang, X., Minnaar, K., Macia, M. L., Fairchild, D. P., Kan, W. C. and Newbury, B. (2010). Tensile Strain Capacity Equations for Strain-based Design of Welded Pipelines. *Proceedings of 8th International Pipeline Conference (IPC2010)*, Calgary, Alberta, Canada, 355-363.

Kim, Y. J., Kim, J. S., Cho, S. M. and Kim, Y.J. (2004). 3-D Constraint Effects on *J* Testing and Crack Tip Constraint in M(T), SE(B), SE(T) and C(T) Specimens: Numerical Study. *Engineering Fracture Mechanics*, 71, 1203-1218.

Kirk, M. T. and Dodds, R. H. (1993). *J* and *CTOD* Estimation Equations for Shallow Cracks in Single Edge Notch Bend Specimens. *Journal of Testing and Evaluation*, 21(4), 228-38.

Lubliner, J. (2008). *Plasticity Theory*. Courier Dover Publications, Mineola, NY.

McMeeking, R. M. and Parks, D. M. (1979). On Criteria for J-dominance of Crack-tip Fields in Large-scale Yielding. *Elastic-Plastic Fracture, ASTM STP 668*, 175-194.

Moore, P. L. and Pisarski, H. G. (2012). Validation of Methods to Determine CTOD from SENT Specimens. *Proceedings of International offshore and polar engineering conference*, Rhodes, Greece, 577-82.

Moreira, F. and Donato, G. (2010). Estimation Procedures for J and CTOD Fracture Parameters Experimental Evaluation Using Homogeneous and Mismatched Clamped SE(T) Specimens. *Proceedings of ASME 2010 Pressure Vessels and Piping Conference, PVP2010*, Bellevue, Washington, USA, July 18-22.

Qian, X. and Dodds, R. H. (2006). *WARP3D: Effect of Mesh Refinement on the Crack-tip Stress Field for SSY Models*. University of Illinois at Urbana-Champaign, IL.

Rice, J. R., Rosengren, G. F. (1968). Plane Strain Deformation Near a Crack Tip in a Power Law Hardening Material. *Journal of the Mechanics of Physics and Solids*, 16, 1-12.

Ruggieri, C. (2012). Further Results in J and CTOD Estimation Procedures for SE (T) Fracture Specimens–Part I: Homogeneous Materials. *Engineering Fracture Mechanics*, 79, 245-265.

Shen, G., Bouchard, R., Gianetto, J. A., and Tyson, W. R. (2008). Fracture Toughness Evaluation of High Strength Steel Pipe. *Proceedings of PVP 2008, ASME Pressure Vessel and Piping Division Conference*, Chicago, Illinois, USA, July 27-31.

Shen, G., Gianetto, J. A., and Tyson, W. R. (2009). Measurement of J-R Curves Using Single-Specimen Technique on Clamped SE(T) Specimens. *Proceedings of Nineteenth International Offshore and Polar Engineering Conference*, the International Society of Offshore and Polar Engineers (ISOPE), Osaka, Japan, 92-99.

Shen, G., and Tyson, W. R. (2009a). Evaluation of CTOD from J-integral for SE(T) specimens. *Pipeline Technology Conference*, Ostend, Belgium, October 12-14.

Shen, G., and Tyson, W. R. (2009b). Crack Size Evaluation Using Unloading Compliance in Single-Specimen Single-Edge-Notched Tension Fracture Toughness Testing. *Journal of Testing and Evaluation*, 37(4), Paper ID JTE102368.

Shen, G., Tyson, W. R., Gianetto, J. A., Park, D-Y. (2010). Effect of Side Grooves on Compliance, J-Integral and Constraint of a Clamped SE(T) Specimen. *ASME Conference Proceedings 2010*, 81-9.

Shih, C. F. (1981). Relationships between the J-integral and the Crack Opening Displacement for Stationary and Extending Cracks. *Journal of the Mechanics and Physics of Solids*, 29(4), 305-326.

Soboyejo, W. O. (2003). *Mechanical Properties of Engineered Materials*. Marcel Dekker, Inc., New York.

Tada, H., Paris, P. C. and Irwin, G. R. (1973). *The Stress Analysis of Cracks Handbook*. Del Research Corporation, Hellertown, PA.

Tang, H., Macia, M., Minnaar, K., Gioielli, P., Kibey, S., and Fairchild, D. (2010). Development of the SENT Test for Strain-Based Design of Welded Pipelines. *Proceedings of 8th International Pipeline Conference (IPC2010)*, Calgary, Alberta, Canada, September 27–October 1.

Tracey, D. M. (1976). Finite Element Solutions for Crack-Tip Behavior in Small-Scale Yielding. *Journal of Engineering Materials and Technology*, 98(2), 146-151.

Verstraete, M. A., Denys, R. M., Van Minnebruggen, K., Hertelé, S., and De Waele, W. (2013). Determination of CTOD Resistance Curves in Side-grooved Single-Edge Notched Tensile Specimens Using Full Field Deformation Measurements. *Engineering Fracture Mechanics*, 110, 12-22.

Wang, E., Zhou, W., Shen, G. and Duan. D. (2012). An Experimental Study on J(CTOD)-R Curves of Single Edge Tension Specimens for X80 Steel. *Proceedings of 9th International Pipeline Conference (IPC2012)*, Calgary, Alberta, Canada, September 24–28, Paper Number: IPC2012-90323.

Willoughby, A. A. and Garwood, S. J. (1983). On the Unloading Compliance Method of Deriving Single-Specimen R-Curves in Three-Point Bending. *Elastic Plastic Fracture Second Symposium, Volume II: Fracture Curves and Engineering Applications*, ASTM STP 803, II-372-II-397.

Wu, S. X., Mai, Y. W. and Cotterell, B. (1988a). Plastic Rotation Factors of Three-point Bend and Compact Tension Specimens. *Journal of Test Evaluation*, 16, 555 – 7.

Wu, S. X., Cotterell, B. and Mai, Y. W. (1988b). Slip-line Field Solutions for Three-point Notch-bend Specimens. *International Journal of Fracture*, 37(1), 13-29.

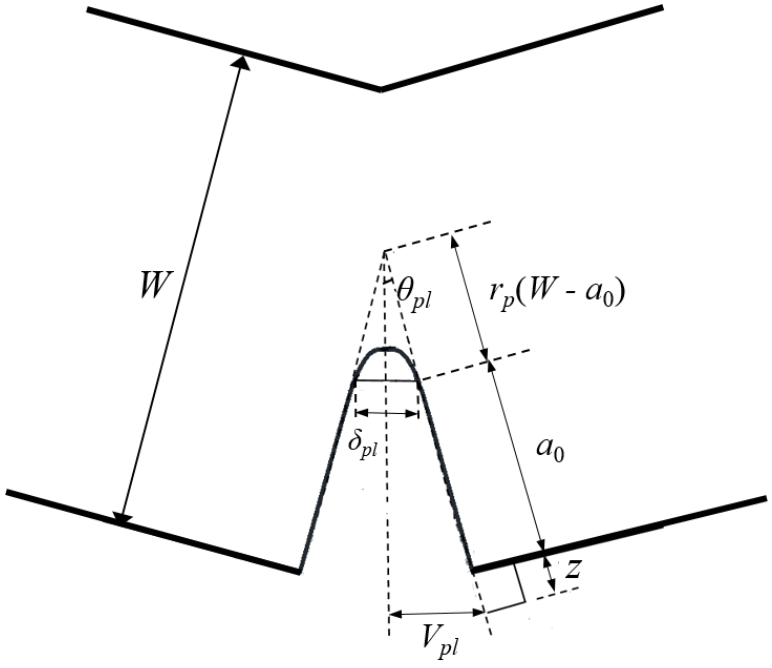

Figure 4.1. Schematically illustration of the geometric relationship for the evaluation of *CTOD* using single clip-on gauge plastic hinge model

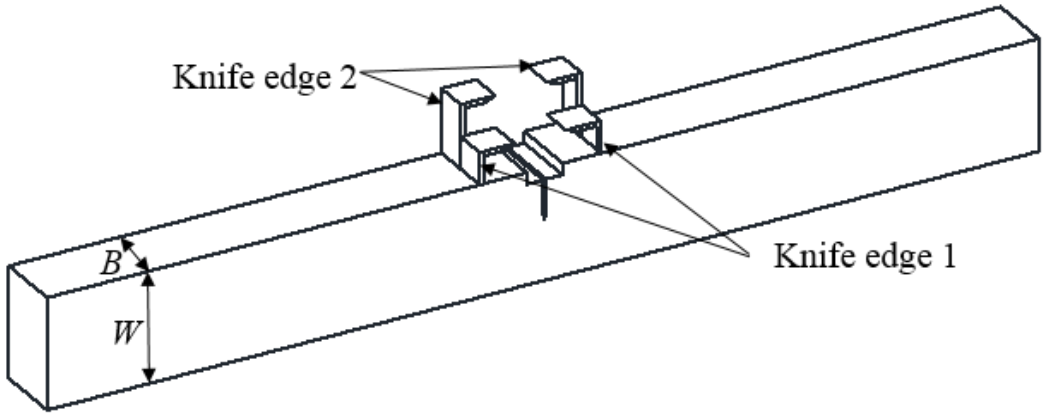

(a)

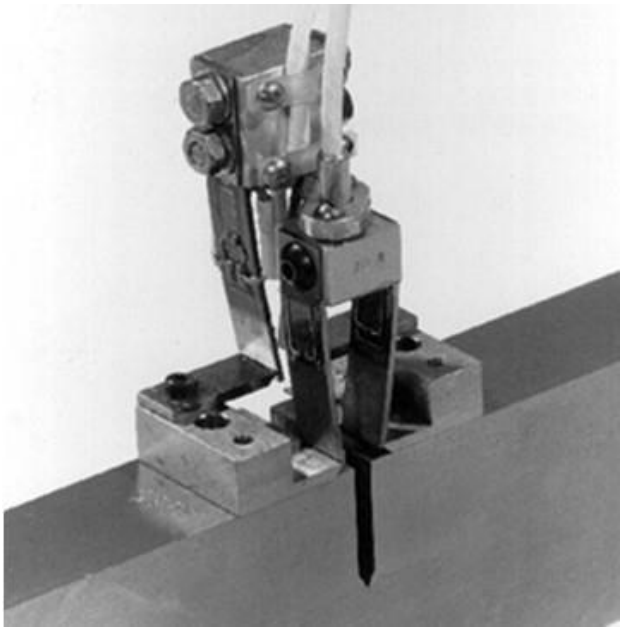

(b)

Figure 4.2. Illustration of the installation of knife edges for the double clip-on gauge method

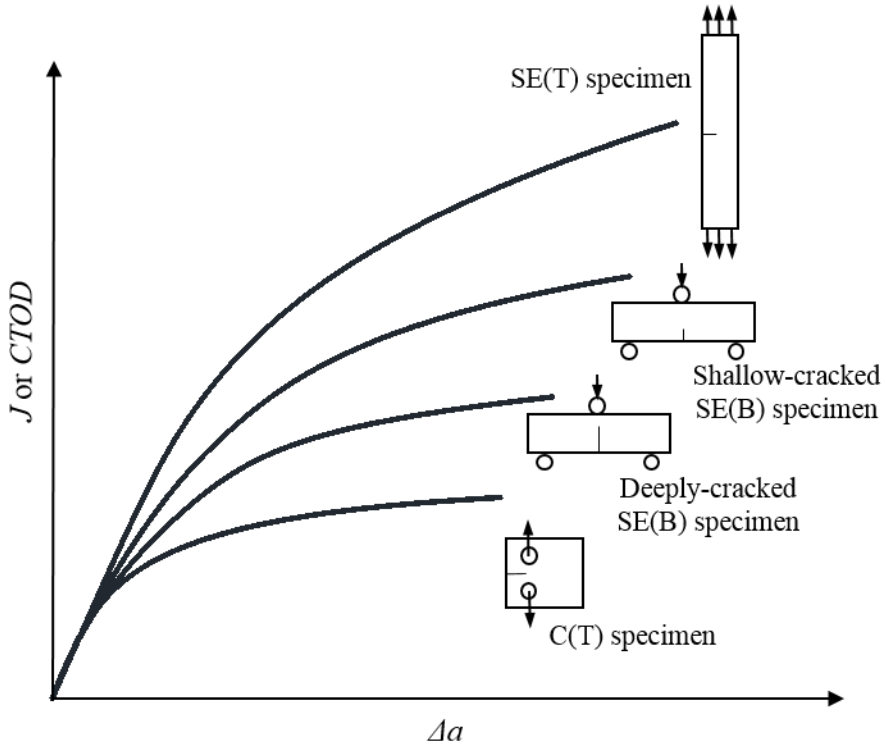

Figure 4.3. Typical toughness resistance curves for various types of small-scale specimens

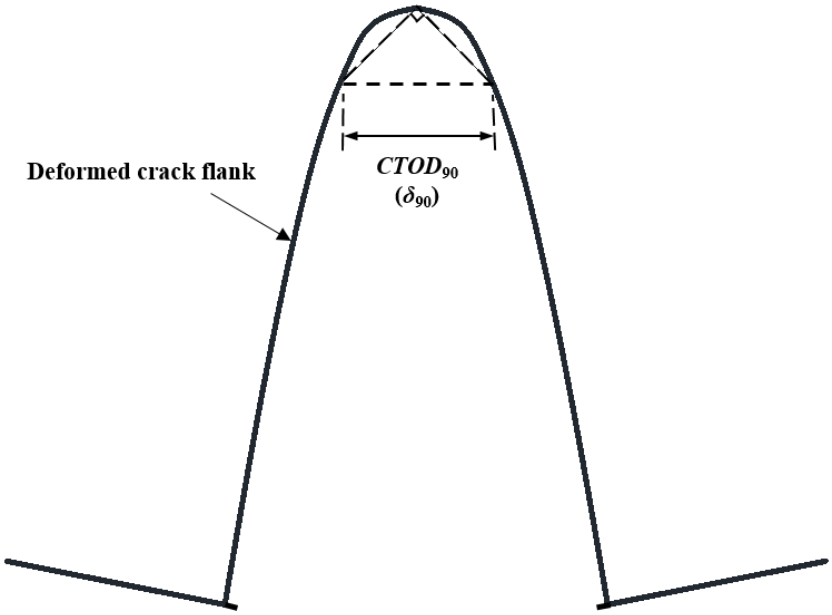

(a) Displacement at the intersection of a 90 degree vertex with the crack flanks

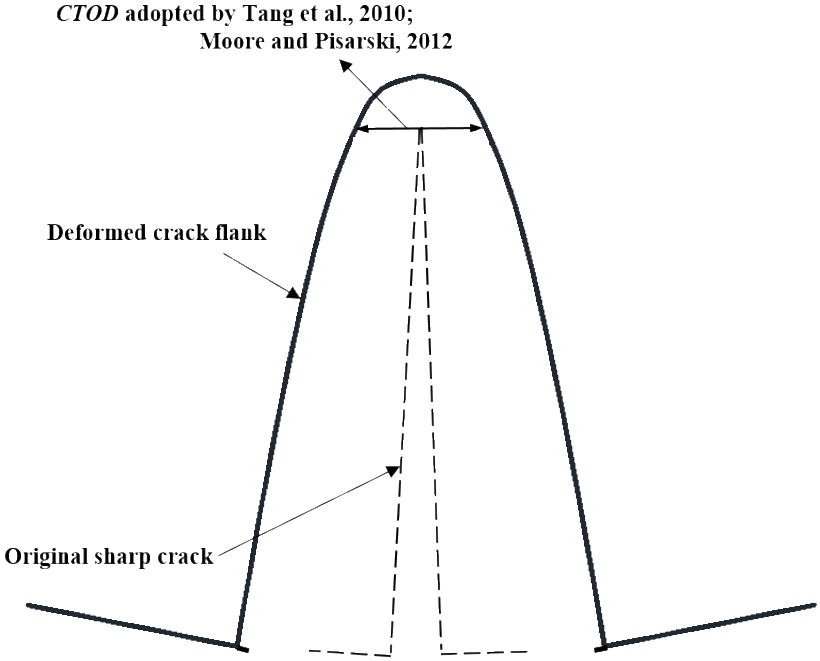

(a) Opening displacement of the deformed crack at the original crack tip

Figure 4.4. Schematically illustration of *CTOD* definitions

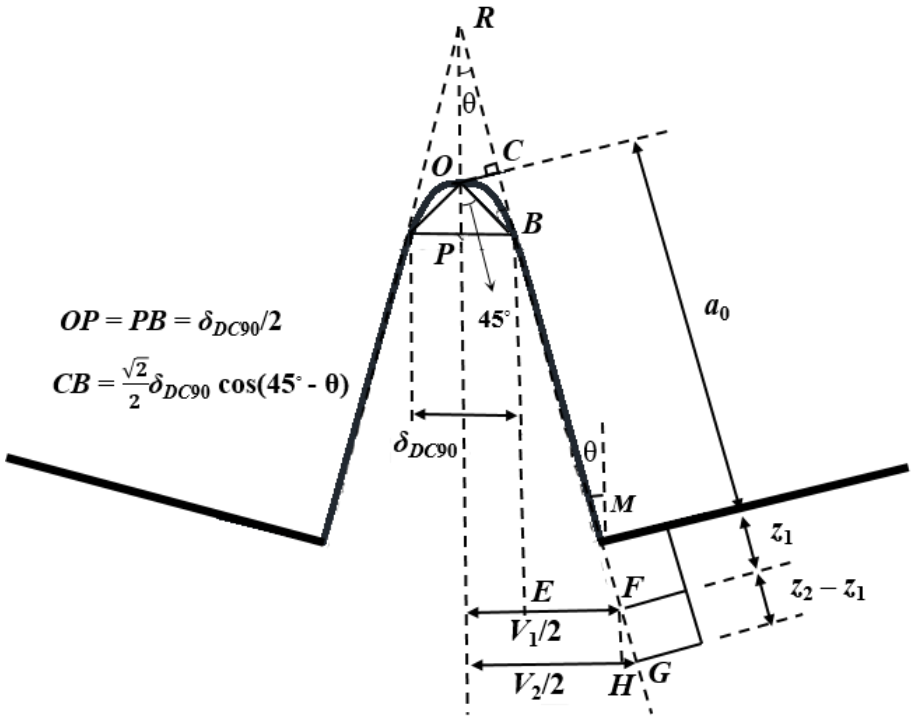

Figure 4.5. Schematically illustration of the geometric relationship for the evaluation of *CTOD*

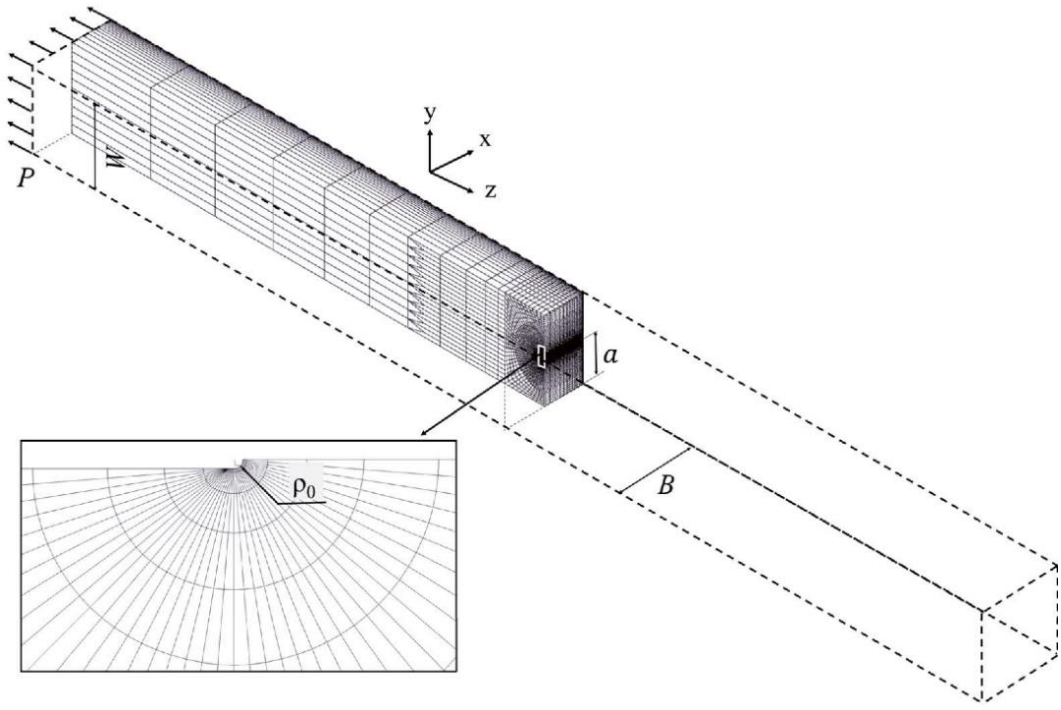

Figure 4.6. Geometric and mesh configuration of the finite element model with a blunt crack tip

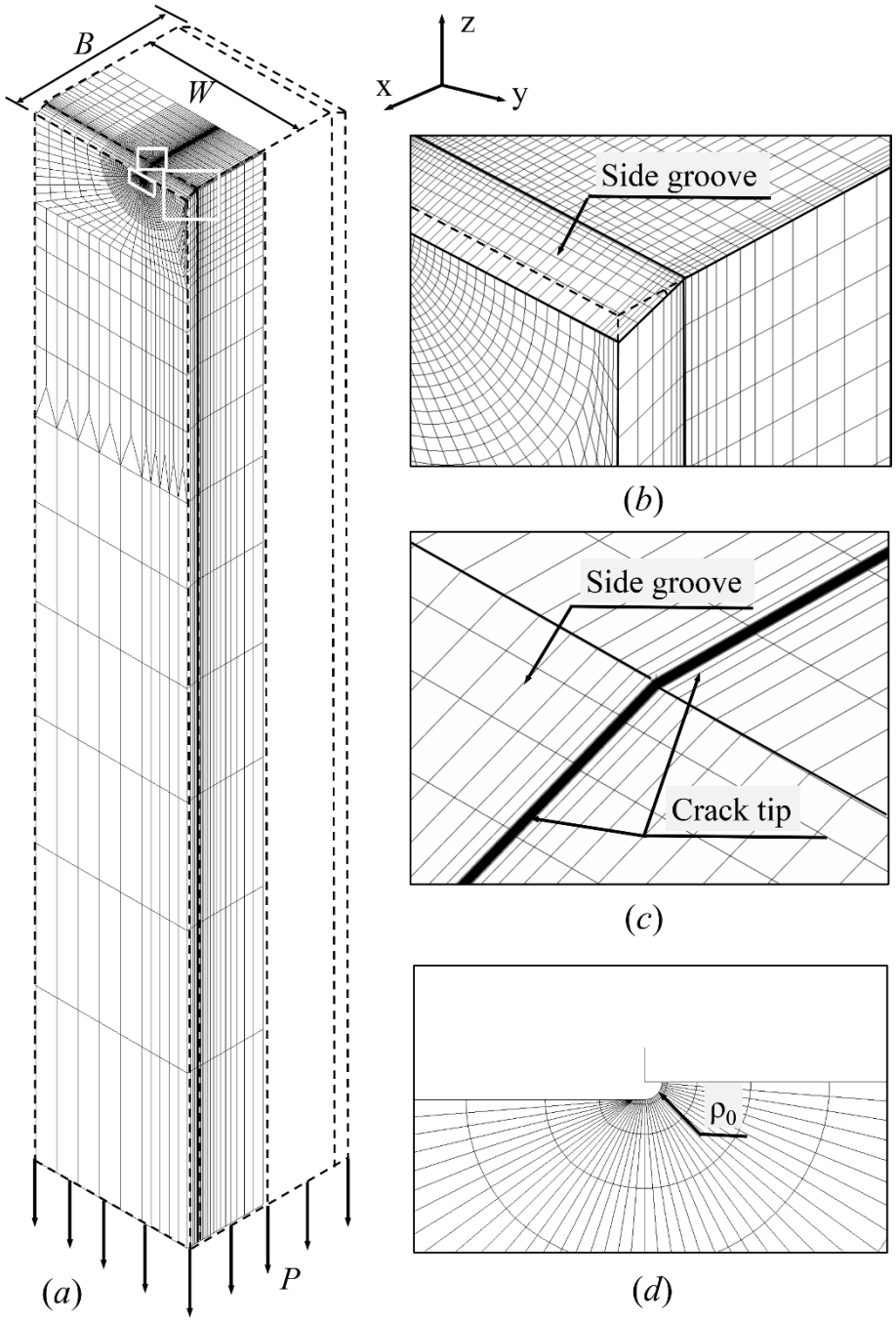

Figure 4.7. A typical side-grooved finite element model for clamped SE(T) specimen

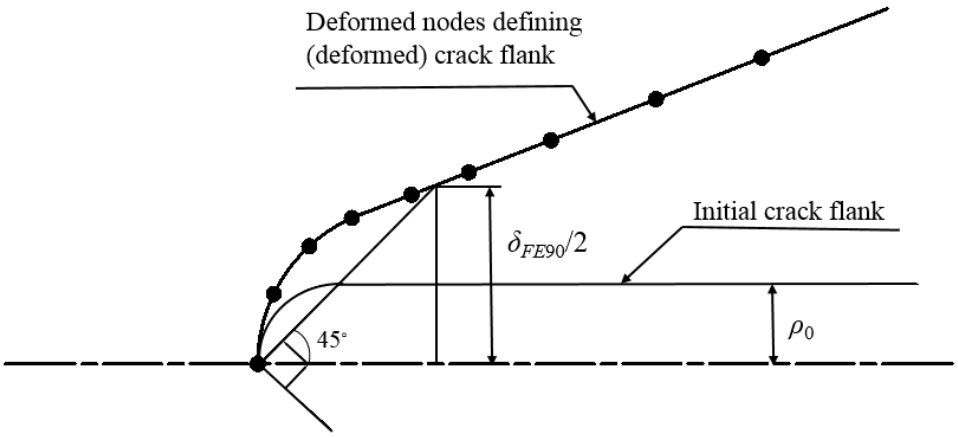

Figure 4.8. Schematically illustration of the determination of *CTOD* in FEA

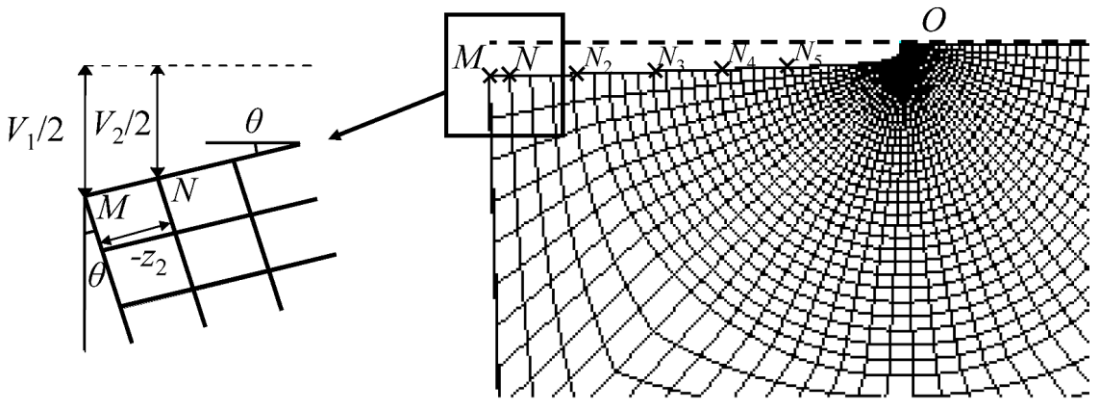

Figure 4.9. Schematically illustration of the double clip-on gauge method in FEA

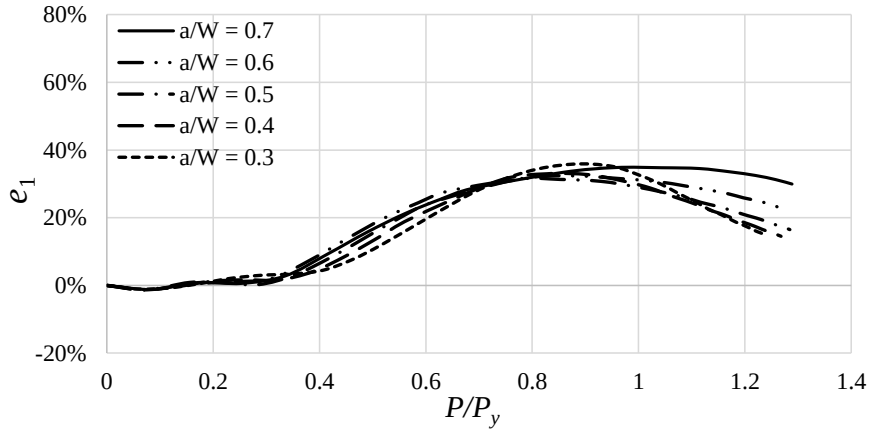

(a) *B/W* = 0.5

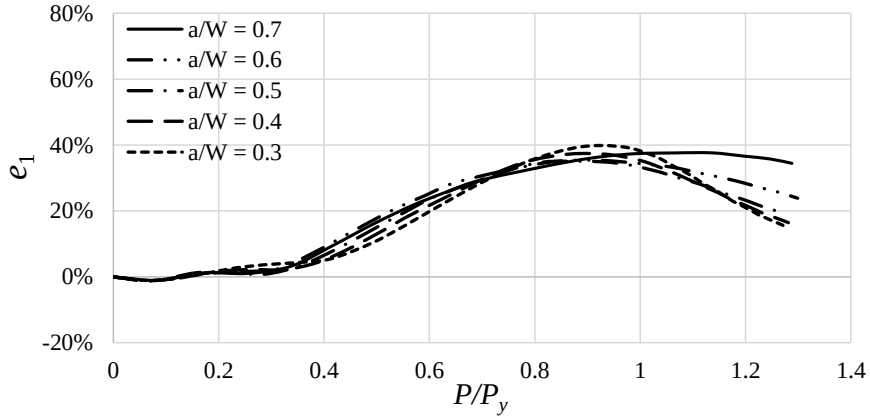

(b) *B/W* = 1

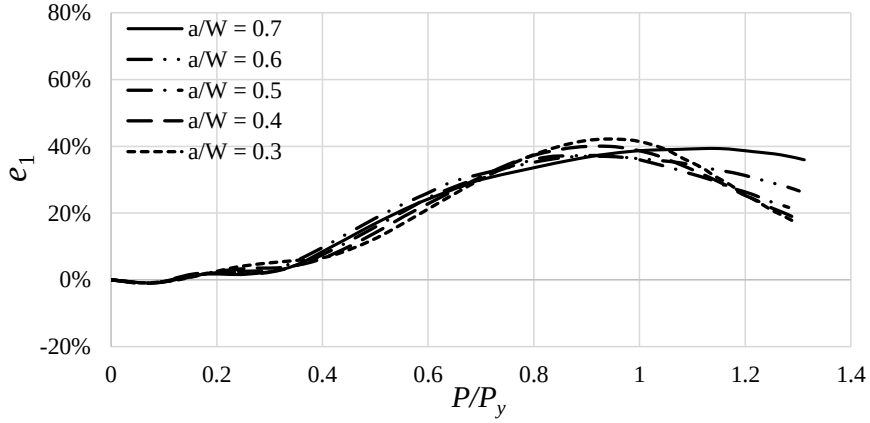

(c) *B/W* = 2

Figure 4.10. Variation of e_1 against *P/Py* for plane-sided specimens with *n* = 10 and the same *B/W*

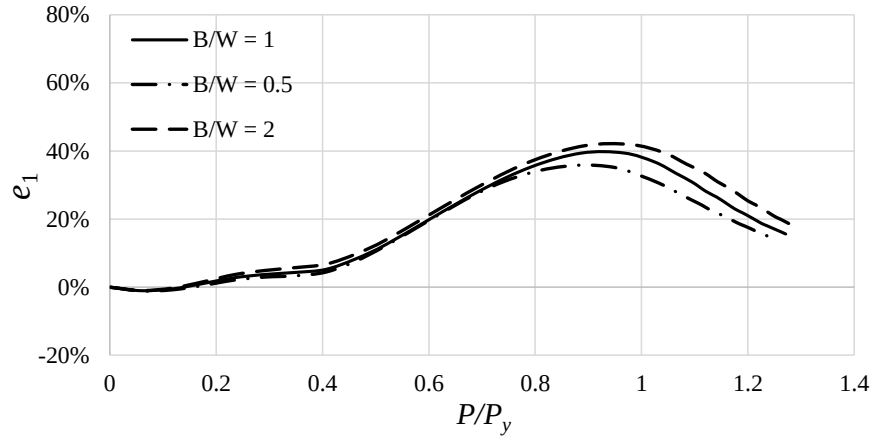

(a) $a/W = 0.3$

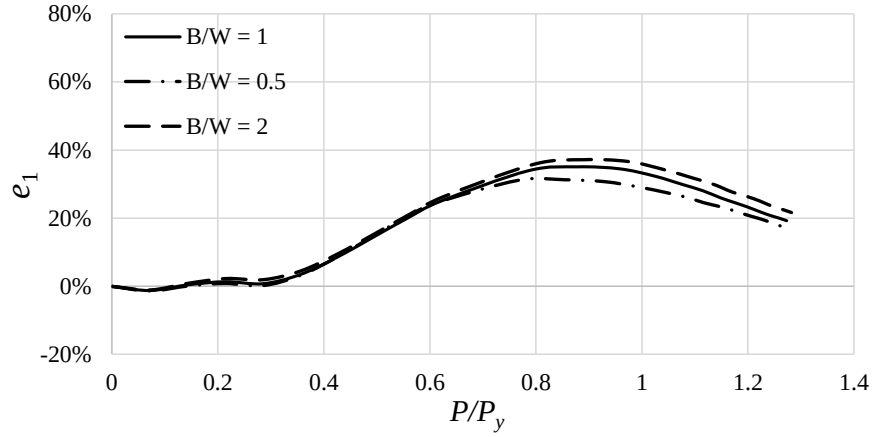

(b) $a/W = 0.5$

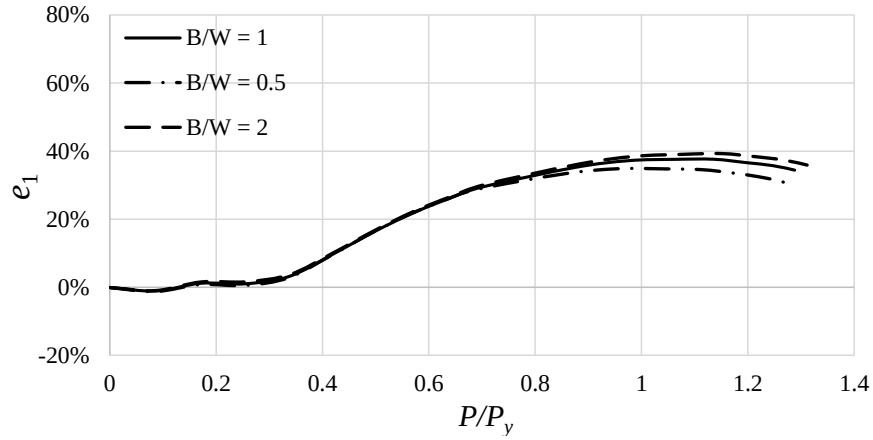

(c) $a/W = 0.7$

Figure 4.11. Variation of e_1 against *P/Py* for plane-sided specimens with $n = 10$ and the same *a/W*

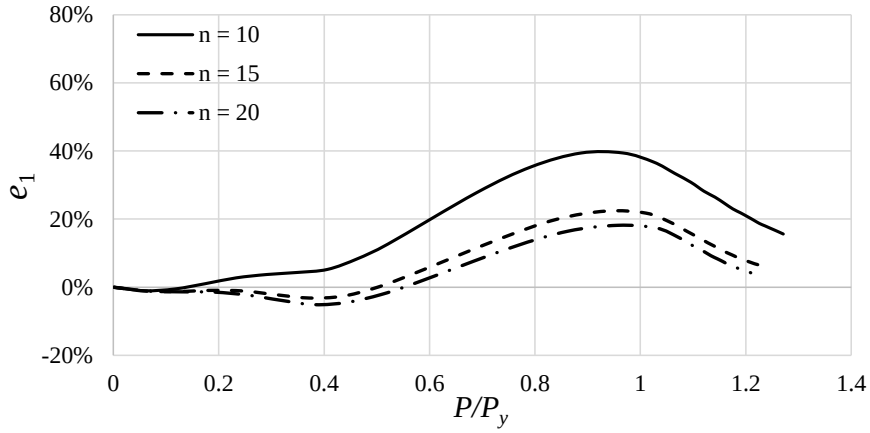

(a) $a/W = 0.3$

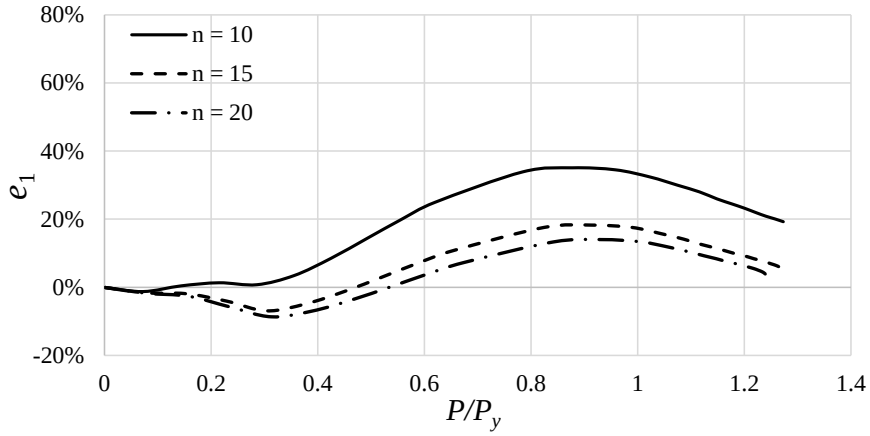

(b) $a/W = 0.5$

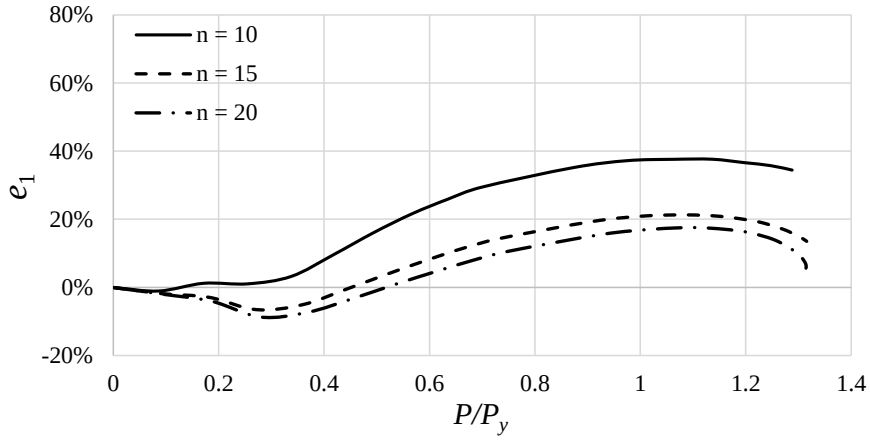

(c) $a/W = 0.7$

Figure 4.12. Variation of e_1 against P/Py for plane-sided specimens with $B/W = 1$ and the same a/W

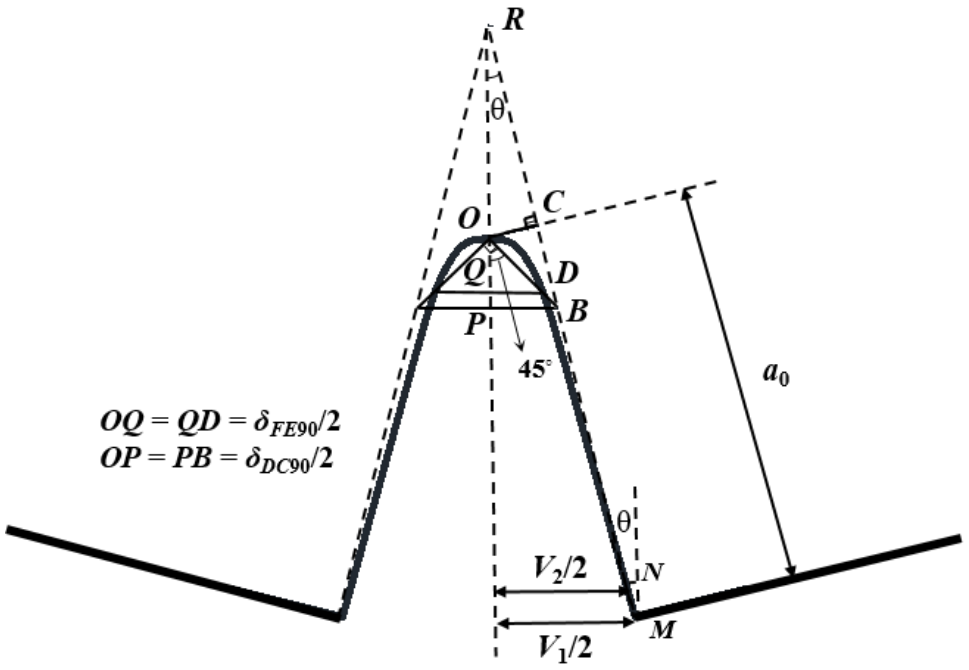

(a)

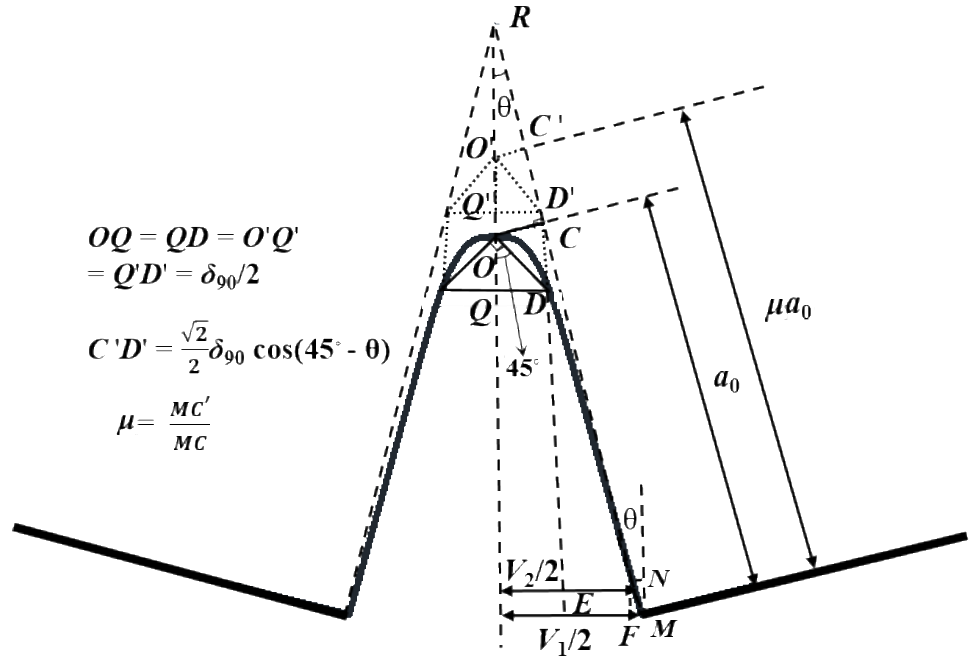

(b)

Figure 4.13. Geometric relationship surrounding the blunt crack tip

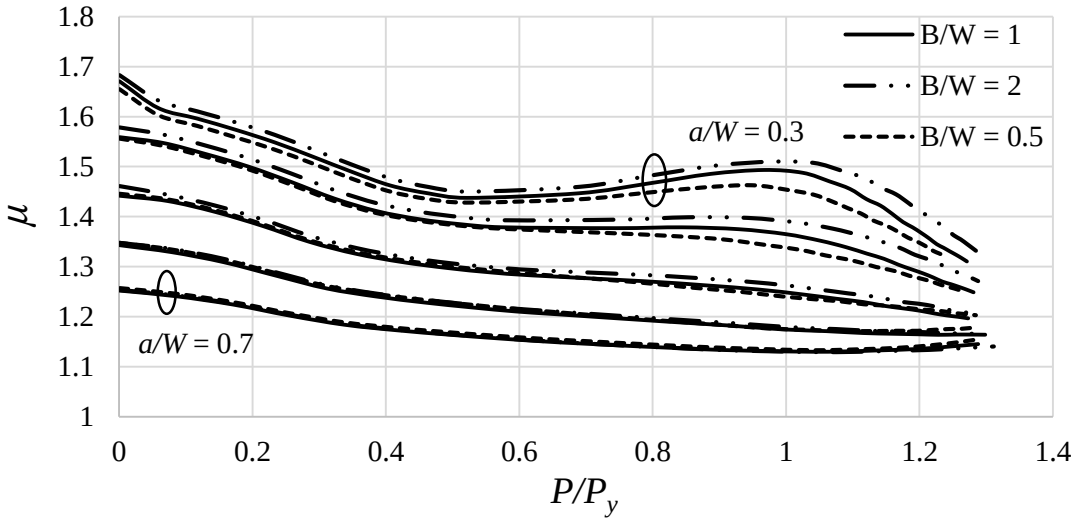

Figure 4.14. Variation of the proposed correction factor μ against *P/Py* for plane-sided specimens with n = 10

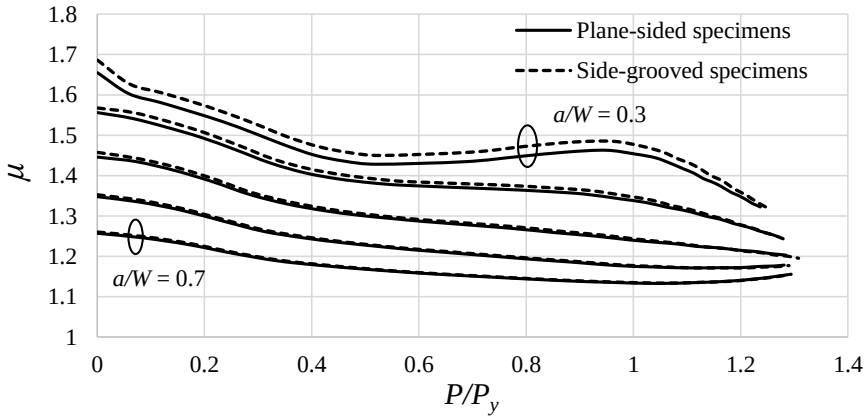

(a) $B/W = 0.5$

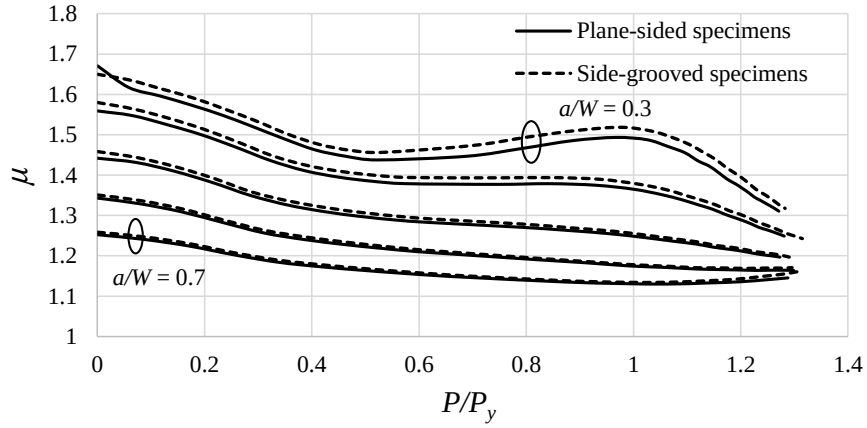

(b) $B/W = 1$

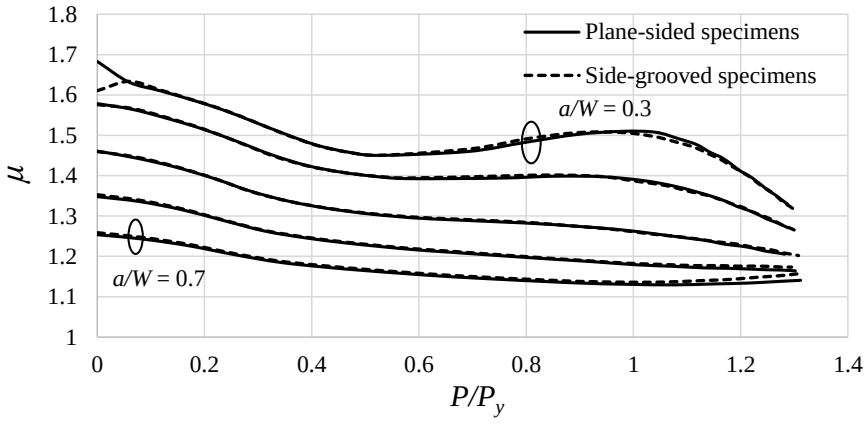

(c) $B/W = 2$

Figure 4.15. Variation of the proposed correction factor μ against P/Py for specimens with $n = 10$

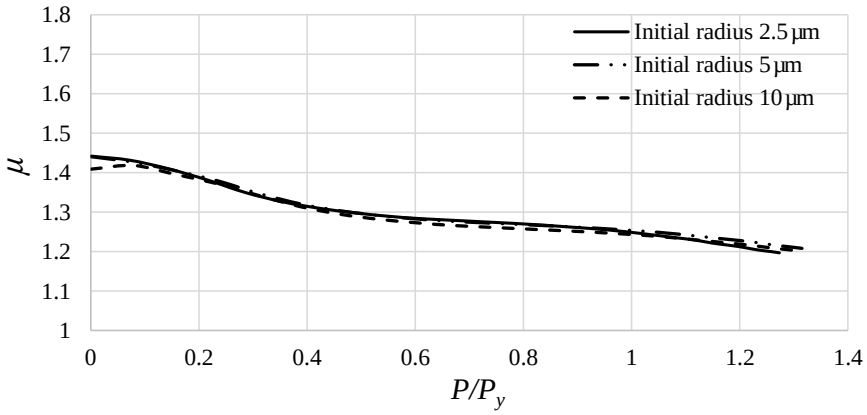

Figure 4.16. Variation of the proposed correction factor μ against *P/Py* for plane-sided specimens with *B/W* = 1, *a/W* = 0.5, *n* = 10 and different initial radius

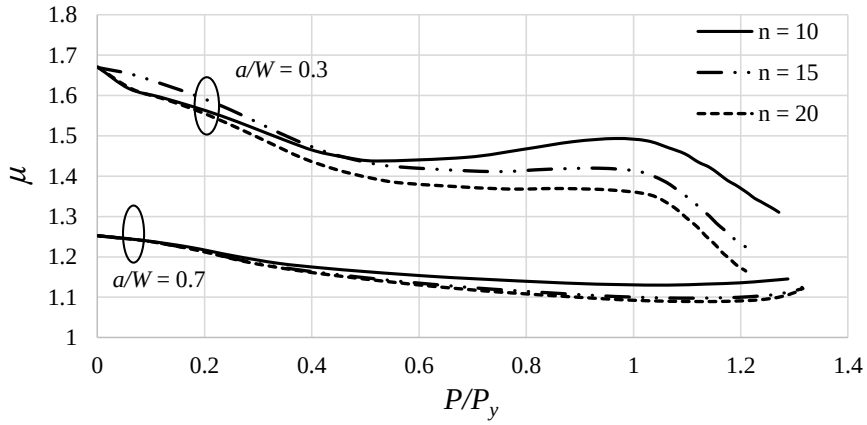

Figure 4.17. Variation of the proposed correction factor μ against *P/Py* for plane-sided specimens with *B/W* = 1 and different *n* values

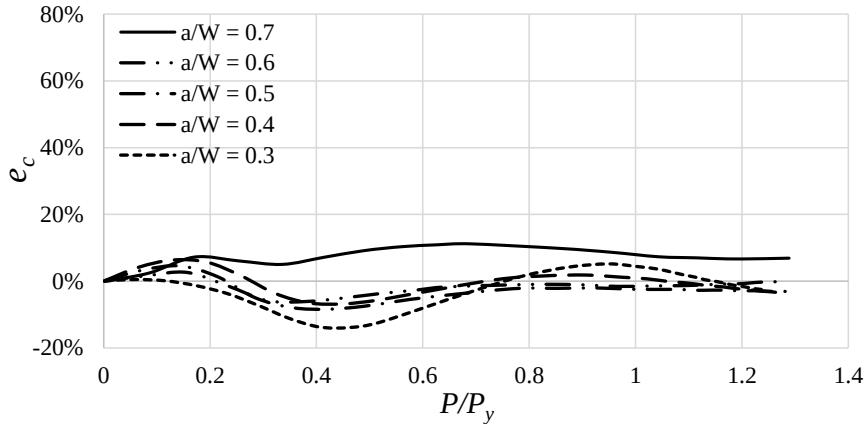

(a) $B/W = 0.5$

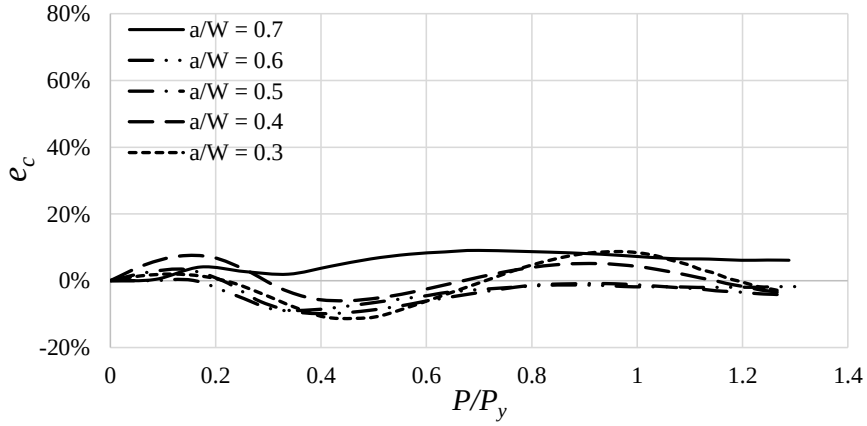

(b) $B/W = 1$

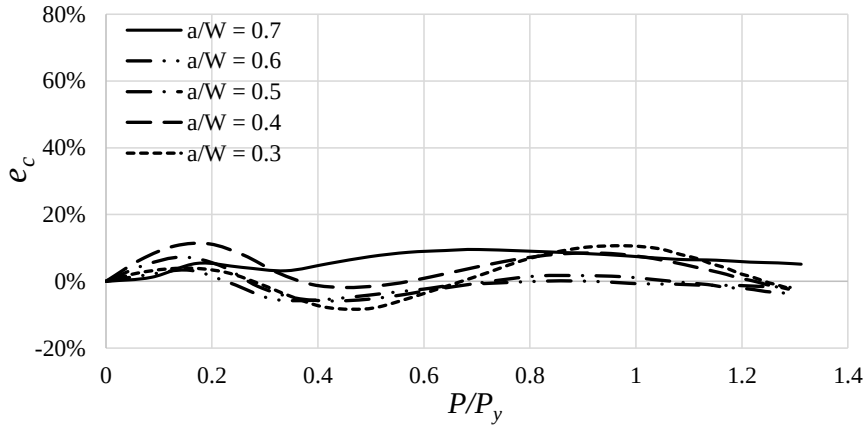

(c) $B/W = 2$

Figure 4.18. Variation of e_c against P/Py for plane-sided specimens with $n = 10$ and the same B/W

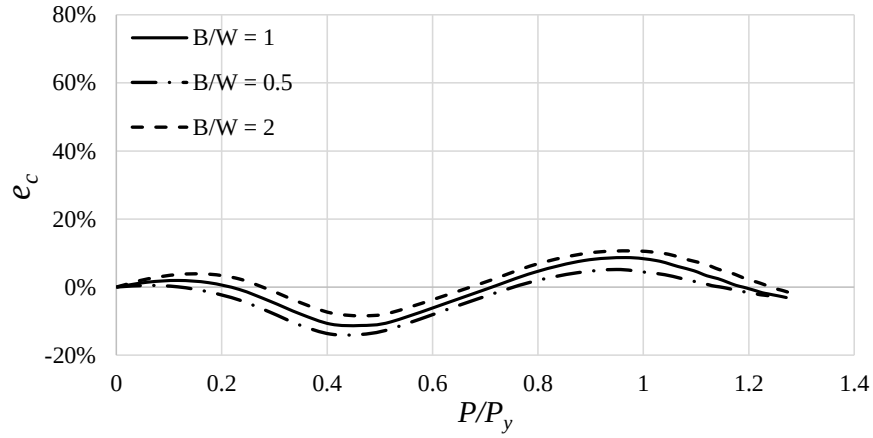

(a) $a/W = 0.3$

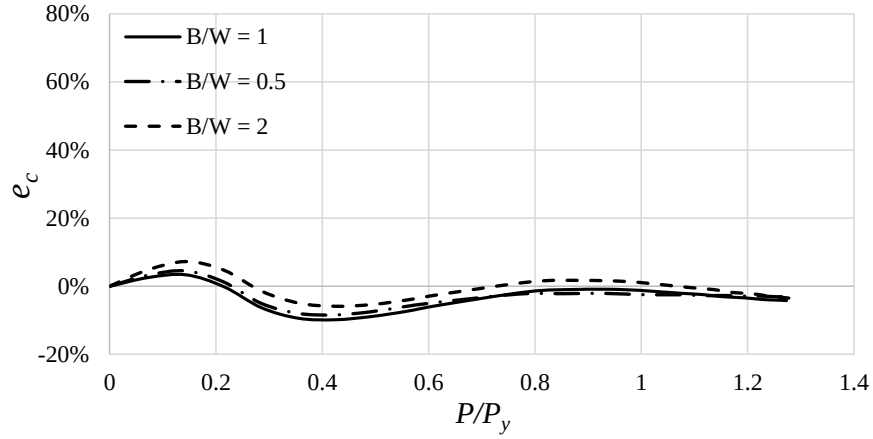

(b) $a/W = 0.5$

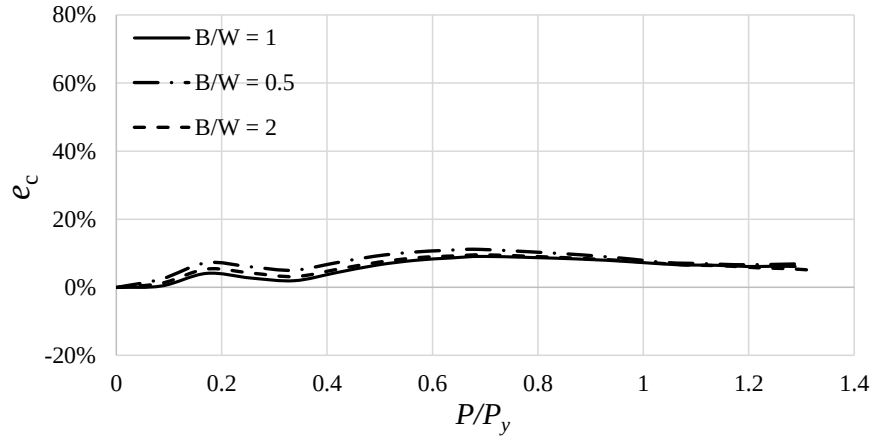

(c) $a/W = 0.7$

Figure 4.19. Variation of e_c against P/Py for plane-sided specimens with $n = 10$ and the same a/W

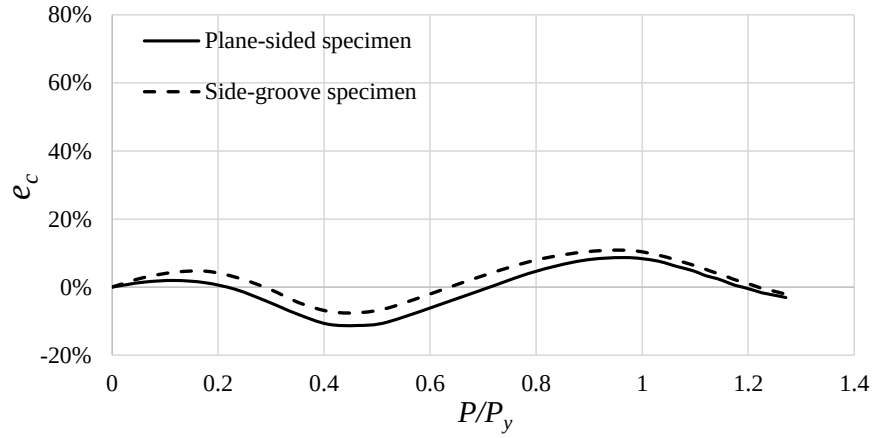

(a) $a/W = 0.3$

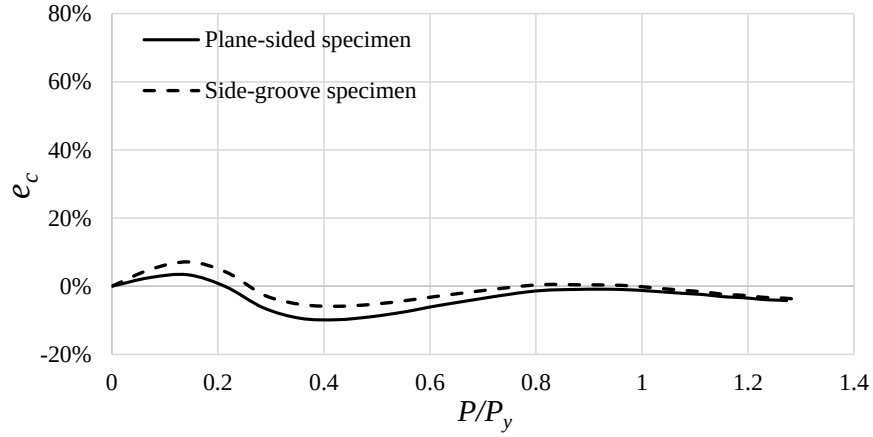

(b) $a/W = 0.5$

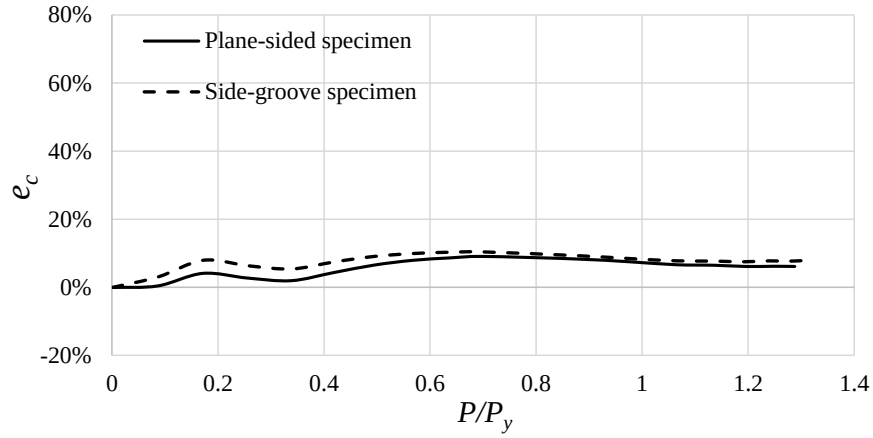

(c) $a/W = 0.7$

Figure 4.20. Variation of e_c against P/Py for specimens with $n = 10$, $B/W = 1$ and the same a/W

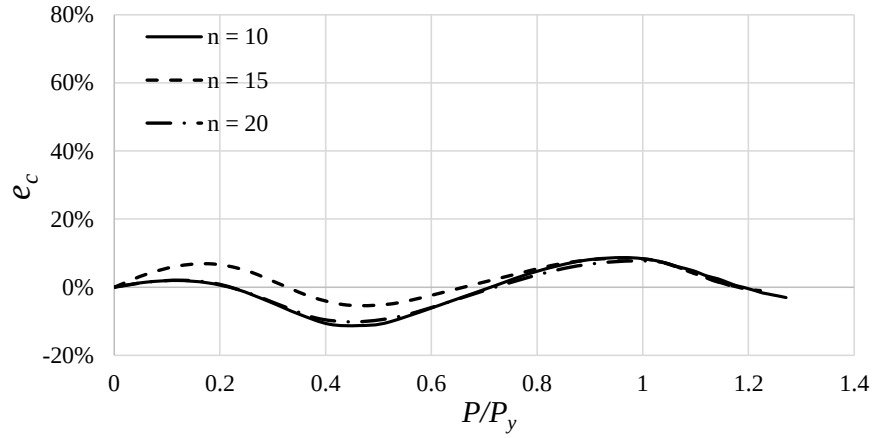

(a) $a/W = 0.3$

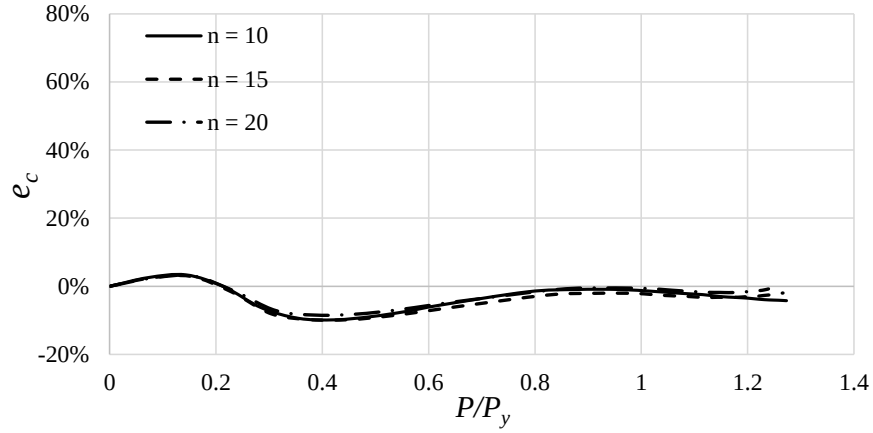

(b) $a/W = 0.5$

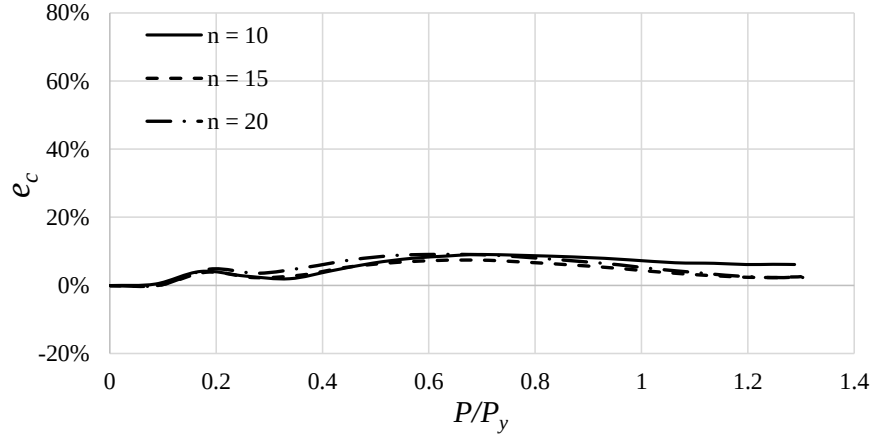

(c) $a/W = 0.7$

Figure 4.21. Variation of e_c against P/Py for plane-sided specimens with $B/W = 1$ and the same a/W

Chapter 5 Summary and Conclusions

The fracture toughness is a key input for the structural integrity assessment and strain-based design of steel energy pipelines containing planar defects (i.e. cracks). For modern ductile pipeline steels, the fracture process is usually accompanied with relatively large plastic deformation at the crack tip and considerable crack extension. As the crack grows, a plastic zone at the crack tip increases in size and the driving force must increase accordingly to maintain the crack growth. Therefore, the fracture toughness resistance curve (e.g. J-integral (*J*) or crack tip opening displacement (*CTOD*) resistance curve) is typically used to characterize the fracture property of the pipeline steels. There are two main components of the toughness resistance curves, namely the crack growth, Δa, and the toughness value (*J* or *CTOD*) corresponding to this particular crack growth.

The *J-R* and *CTOD-R* curves are commonly measured on small-scale specimens, e.g. the three-point single-edge notched bend (SE(B)), compact tension (C(T)) and single-edge notched tension (SE(T)) specimens. During tests, the applied load (*P*), the corresponding load-line displacement (*LLD*) and the crack mouth opening displacement (*CMOD*) need to be measured simultaneously. The obtained *P-LLD* and *P-CMOD* curves are the main input of the experimental evaluation of *J-R* or *CTOD-R* curves.

5.1 Effect of the Crack Front Curvature on the *CMOD* Compliance and *J* for SE(B) Specimens

As specified in test standards such as ASTM E1820-11, all machine notched specimens need to be fatigue pre-cracked to simulate natural sharp cracks before the resistance curve testing. The fatigue pre-cracking often introduces curved as opposed to straight crack fronts. Furthermore, the crack growth during the test is in general non-uniform across the crack front.

Steenkamp investigated the influence of the crack front curvature on the specimen compliance using two-dimensional (2D) plane strain finite element analyses based on seven specimens with the same average crack length but different crack front curvatures.

The previous studies, e.g. Crouch, Nikishkov et al., Zhou and Soboyejo, all focused on the effects of the crack front curvature on the local crack driving forces, and the crack front straightness is generally defined based on the difference between the maximum and the minimum crack length, which is not constant with the crack front straightness criterion specified in ASTM E1820-11. In the present study, the main focus is on the effect of the crack front curvature on the average J-integral over the crack front, which is considered to be more relevant to the characterization of the experimentally determined *J-R* curve. Symmetric bowed crack fronts with different curvatures were considered in the analysis. The crack front curvature was characterized by a parameter λ, which is consistent with the crack front straightness criterion specified in ASTM E1820-11. The larger is λ, the higher is the crack front curvature. The maximum allowable crack front curvature according to ASTM E1820-11 corresponds to $\lambda = 0.05$. A power-law expression as proposed by Nikishikov et al. was adopted to characterize the curved crack front, and it was validated using crack fronts data collected in this study. Two values of shape parameter of the power-law expression for the curved crack front, namely $p = 3$ and 2.5, were considered to investigate its influence on the results. For specimens with given a_{ave}/W, B/W and p, the crack fronts with different levels of curvature were generated by varying λ.

The impact of the crack front curvature on the *J-R* curve experimentally measured from the SE(B) specimen was investigated through systematic linear-elastic and elastic-plastic three-dimensional (3D) finite element analyses (FEA) of plane-sided SE(B) specimens containing both straight and curved crack fronts. A wide range of average crack lengths ($a_{ave}/W = 0.3$, 0.5 and 0.7) and thickness-to-width ratios ($B/W = 1$, 0.5 and 0.25 covering the range specified in ASTM E1820-11) was included.

Linear elastic 3D FEA was employed to investigate the impact of the crack front curvature on the *CMOD* compliance and the evaluated crack length. The *CMOD* compliance value for the specimen with a curved crack front was compared with the value obtained from a specimen with a straight crack front and having the same average crack length and thickness. For a given specimen with either a straight or curved crack front, the accuracy of the crack length predicted from the *CMOD* compliance using the

empirical equations reported in the literature was examined. The use of three different elastic moduli, i.e. E, E' and E_e, in the prediction of the average crack length from the *CMOD* compliance was compared.

The numerical results show that the crack front curvature has a negligible impact on the *CMOD* compliance for $\lambda \leq 0.05$ for the SE(B) specimen, and the crack length predicted from the *CMOD* compliance is insensitive to the crack front curvature for all the considered λ values (up to $\lambda = 0.10$) regardless of a_{ave}/W and B/W ratios. It is observed that the use of E_e as reported by Wang et al. can lead to the most accurate prediction of the average crack length with errors being less than 1% for wide ranges of a_{ave}/W, B/W and crack front curvatures for SE(B) specimens.

The Ramberg-Osgood constitutive law was employed as the uniaxial stress-strain relationship for investigating the impact of the crack front curvature on the accuracy of the average J over the crack front, J^{η}, evaluated using the plastic eta factor-based approach as specified in ASTM E1820-11. The plastic geometry factors recommended in ASTM E1820-11 were employed to evaluate the *CMOD*- and *LLD*-based J^{η} for all the specimens considered, except for the *LLD*-based J^{η} for the specimens with $a_{ave}/W = 0.3$, in which case the plastic geometry factors proposed by Zhu et al. were adopted. Two values of the strain hardening exponent, namely $n = 10$ and 20, were considered to investigate the influence of n on the J evaluation.

The numerical results show that given a_{ave}/W and B/W, as the crack front curvature increases, J^{η} becomes less conservative and tends to overestimate the actual average J. For specimens that have curved crack fronts with the crack front curvature equal to the maximum allowable value ($\lambda = 0.05$) as specified in ASTM E1820-11, the errors in J^{η} are between -7% and 6% for almost all the specimens considered in this study. Results of the sensitivity analysis indicate that the choice of the value of p has a negligible impact on the accuracy of J^{η}. New crack front straightness criteria for the SE(B) specimen were recommended by considering that J^{η} overestimates the actual J by no more than 5%. The suggested criteria vary with a_{ave}/W, B/W and n, and are in most cases less stringent than

those specified in ASTM E1820-11, which could potentially lead to a decrease in the specimen rejection rate and cost savings.

5.2 Accuracy of the Double Clip-on Gauge Method for Evaluating *CTOD* of SE(T) Specimens

Due to the similar crack-tip constraint levels between the single-edge tension (SE(T)) specimen and full-scale pipes containing surface cracks under longitudinal tension, there is an increasing trend to determine the toughness resistance (e.g. *CTOD-R*) curve using the SE(T) specimen in the pipeline industry over the last decade. The use of the double clip-on gauge method to experimentally measure *CTOD* was reviewed, and its accuracy was examined through systematic 3D FEA of clamped SE(T) specimens with a wide range of specimen dimensions (a/W = 0.3 to 0.7 with an increment of 0.1, and B/W = 0.5, 1 and 2). The commonly-used 90 degree intersection definition of *CTOD* was adopted in this study as opposite to the definition used by Tang et al. and Moore and Pisarski. Side-grooved SE(T) specimens were also modeled in this study as sensitivity cases to investigate the impact of the presence of side grooves on the measured *CTOD* values. A power-law constitutive relationship was assumed, and three values of strain hardening exponent, namely n = 10, 15 and 20, were considered to investigate the influence of t n on the accuracy of the double-clip on gauge method.

It is observed that the *CTOD* values determined from the double clip-on gauge method may involve errors with as large as 40 - 100%. This error primarily depends on the crack length, the material property and the loading level. The primary attributing factor to the error was identified by examining the geometry surrounding the blunt crack tip. Based on the investigation, a modified *CTOD* evaluation equation was developed to improve the accuracy of *CTOD* evaluated using the double-clip on gauge method. The error in *CTOD* evaluated from the modified double-clip on gauge method is generally within 10%. The results will facilitate the application of the double clip-on gauge method to experimentally determine *CTOD* values.

5.3 Recommendations for Future Work

Recommendations for future work are as follows:

1. Further studies can be carried out to investigate the impact of the crack front curvature on the experimentally determined *J-R* curve for SE(B) specimens based on the crack front straightness criteria specified in the other widely used test standards such as BS 7448 and ISO 12135, and compare the adequacy of these criteria with those specified in ASTM E1820-11.
2. The impact of the crack front curvature on the experimentally determined *J* or *CTOD*, for the non-standard SE(T) specimen can be investigated, which will facilitate the standardization of the SE(T) specimen-based fracture toughness testing procedure.
3. For the investigation on the accuracy of double clip-on gauge method, experimental studies can be carried out to further validate the numerical results obtained in the present study.

Appendix A Derivation of the Relationship between β and λ for Symmetric Bowed Crack Fronts

Consistent with the crack front straightness criterion in ASTM E1820-11, the parameter λ is defined as

$$\lambda = max(a_{max9} - a_{ave}, a_{ave} - a_{min9})/B \tag{A.1}$$

where a_{max9} and a_{min9} are the maximum and minimum values of the nine physical measurements of the crack length. For specimens with symmetric bowed crack fronts characterized by Eq. (2.3), it follows that (see Fig. 2.3)

$$a_{max9} = a_5 = a(0) \tag{A.2}$$

$$a_{min9} = a_1 = a(0) - 4^p \cdot \beta W \left(0.25 - \frac{\Delta}{2B}\right)^p \tag{A.3}$$

where $\Delta = 0.005W$.

The average crack length a_{ave} is then given by

$$a_{ave} = a(0) - \beta W \cdot \left(0.25 - \frac{\Delta}{2B}\right)^p \cdot \frac{1}{8}\sum_{i=1}^{i=8}[abs(i-5)]^p \tag{A.4}$$

The following equation can be derived from Eqs. (A.2), (A.3) and (A.4):

$$(a_{max9} - a_{ave}) - (a_{ave} - a_{min9}) = \frac{\beta W}{2}\left(0.25 - \frac{\Delta}{2B}\right)^p \left(1 + 2^p + 3^p - \frac{3}{2}\cdot 4^p\right) \tag{A.5}$$

Given that the crack front is symmetric and bowed, the value of p is greater than unity as illustrated in Fig. 2.6. Substituting $p = 1$ into Eq. (A.5) leads to (a_{max9} - a_{ave}) - (a_{ave} - a_{min9}) = 0. For $p > 1$, the derivative of the right hand side of Eq. (A.5) with respect to p is always negative. Therefore for $p > 1$, (a_{max9} - a_{ave}) - (a_{ave} - a_{min9}) < 0, which implies that λ = (a_{ave} - a_{min9})/B for specimens with symmetric bowed crack fronts. Substituting Eqs. (A.3) and (A.4) into λ = (a_{ave} - a_{min9})/B results in

$$\lambda = \frac{\beta W}{B}\left(0.25 - \frac{\Delta}{2B}\right)^p \left[4^p - \frac{1}{8}\sum_{i=1}^{i=8}[abs(i-5)]^p\right] \tag{A.6}$$

Equation (A.6) defines a one-to-one relationship between β and λ for specimens with symmetric bowed crack fronts.

Appendix B Computation of J-integral using Virtual Crack Extension Method

The virtual crack extension method was first proposed by Parks (1974, 1977) and Hellen (1975) independently during 1970s, which could be employed to calculate the energy release rate in finite element analysis (FEA). Several years later, deLorenzi (1982, 1985) improved this method by considering the energy release rate of a cintimuum, which is implemented in ADINA (ADINA, 2012) and briefly introduced here.

Figure B.1 schematically illustrates a virtual crack advance in a two-dimensional (2D) continuum. The crack front is surrounded by three zones of material separated by two contours. During the virtual crack extension process, known as virtual shift in ADINA (ADINA, 2012), zone I shifted rigidly by an amount Δx_1 in the x_1 direction, at the meantime material in zone III remain fixed ,causing a distortion in the material in zone II. Since the crack front is contained in zone I, the crack length could increase accordingly, denoted as Δa. For the material that obeys deformation plasticity, deLorenzi (1982, 1985) showed that the energy release rate can be expressed as:

$$J = \frac{1}{\Delta a}\int_{A_C}\left(\sigma_{ij}\frac{\partial u_j}{\partial x_1} - w\delta_{i1}\right)\frac{\partial \Delta x_1}{\partial x_1}dA_C \tag{B.1}$$

where σ_{ij} is the stress tensor; u_i is the components of the displacement (i = 1, 2 for two dimensional analysis); w denotes the strain energy density; δ_{ij} is the Kronecker delta and A_C is the area of the cracked body.

A more general expression of Eq. (B.1), i.e. Eq. (B.2), was derived by deLorenzi (1982, 1985) to evaluate J using virtual crack extension method, which considers a three-dimensional (3D) body and adopted by the commercial software ADINA (ADINA, 2012).

$$J = \frac{1}{\Delta A_C}\int_{V_C}\left(\sigma_{ij}\frac{\partial u_j}{\partial x_k} - w\delta_{ik}\right)\frac{\partial \Delta x_k}{\partial x_j}dV_C \tag{B.2}$$

where V_C denotes volume of the cracked body; Δx_k is components of the virtual crack extension vector (k = 1, 2 or 3), and ΔA_C is the increase in crack area corresponding to Δx_k. The calculation of ΔA_C depends on whether the geometry is 2D or 3D. For a 2D geometry, $\Delta A_C = b\sqrt{\Delta x_1^2 + \Delta x_2^2}$ where b is the thickness at the crack tip. For a 3D geometry, the geometric relationship after virtual shift is schematically illustrated in Fig. B.2, and ΔA_C could be written as $\Delta A_C = \int \sqrt{\Delta x_i' \Delta x_i'}\, ds$, where $\Delta x_i' = \Delta x_i - (\sum_{j=1}^{3} t_j \Delta x_j) t_i$, t_i (i = 1, 2 or 3) is the component or directional cosine of the unit tangent vector along the crack front and $\Delta x_i'$ is always perpendicular to t_i; ds is the differential length along the crack front. For a real 3D problem, J typically varies along the crack front. By assuming ΔA_C incrementally along the crack front, as shown in Fig. B.2(b), it would result in a local J value at that particular point along the crack front (Anderson, 2005). In finite element analysis, this approach will provide a local J value corresponding to each layer along the thickness direction in the FEA model.

By adopting the virtual crack extension method, the contour and surface integrations for two- and three- dimensional problems are converted into an area integration and a volume integration, respectively, which could improve the accuracy of the numerical study significantly. It is noted that Eq. (B.2) is just the basic expression for J calculation and the impacts of hoop stress, thermal effect, and dynamic effect are not considered (ADINA, 2012). More details about the virtual crack extension method could be found in the literature, e.g. deLorenzi (1982 and 1985), Anderson (2005) and ADINA (2012).

Reference

ADINA (2012). *Theory and Modeling Guide*. ADINA R & D Inc., Watertown, MA.

Anderson, T. L. (2005). *Fracture Mechanics—Fundamentals and Applications*, Third edition. CRC Press, Boca Raton.

ASTM (2011). *ASTM E1820-11: Standard Test Method for Measurement of Fracture Toughness*. America Society of Testing and Materials International, West Conshohocken, PA.

deLorenzi, H. G. (1982). On the Energy Release Rate and the *J*-Integral of 3-D Crack Configurations. *International Journal of Fracture,* 19, 183-93.

deLorenzi, H. G. (1985). Energy Release Rate Calculation by the Finite Element Method. *Engineering Fracture Mechanics*, 21, 129-43.

Hellen, T. K. (1975). On the Method of Virtual Crack Extension. *International Journal for Numerical Methods in Engineering*, 9, 187-207.

Parks, D. M. (1974). A Stiffness Derivative Finite Element Technique for Determination of Crack Tip Stress Intensity Factors. *International Journal of Fracture*, 10, 487-502.

Parks, D. M. (1977). The Virtual Crack Extension Method for Nonlinear Material Behavour. *Computer Methods in Applied Mechanics and Engineering*, 12, 353-364.

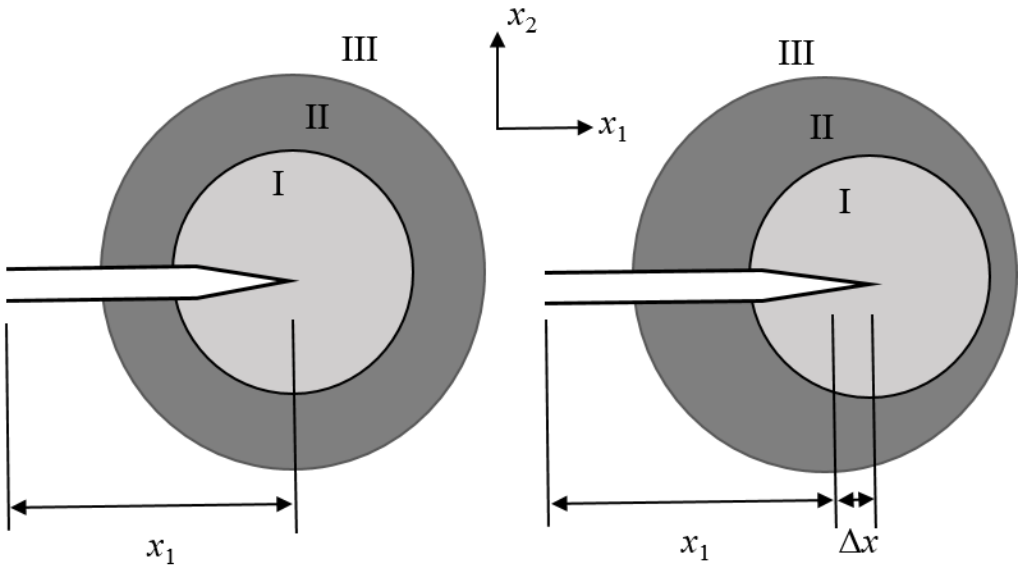

(a) Before virtual shift (b) After virtual shift

I: zone rigidly shifted by virtual shift

II: zone distorted by virtual shift

III: zone unchanged by virtual shift

Figure B.1. The virtual crack extension method in two-dimensional analysis

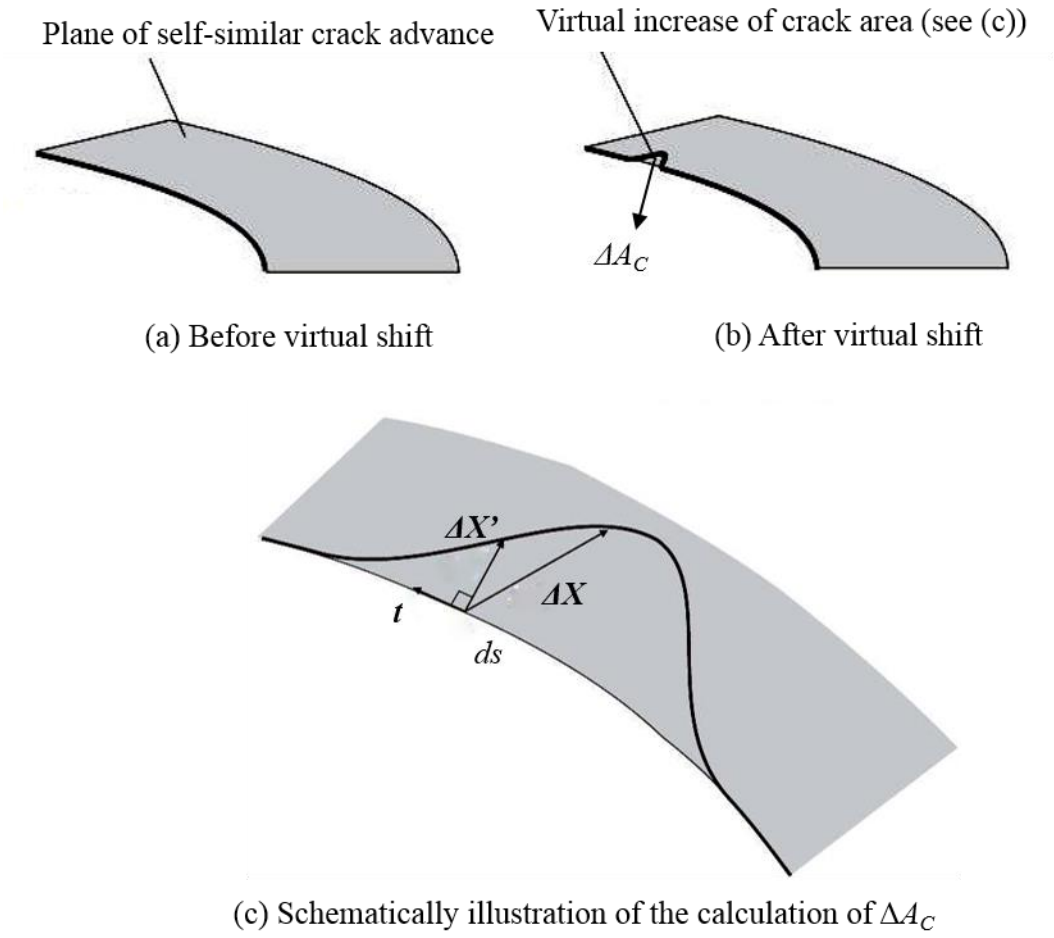

Figure B.2. The virtual crack extension method in three-dimensional analysis

Appendix C Copyright Permission

Permission to include the following articles has been requested and granted with the condition that this thesis would not be published commercially or on a website:

Yan, Z., and Zhou, W. (2014). Effect of Crack Front Curvature on CMOD Compliance and Crack Length Evaluation for Single-edge Bend Specimens. *Proc. of the CSME International Congress*, Toronto, Ontario, Canada, June 1-4.

Yan, Z., and Zhou W. (2014). Effect of Crack Front Curvature on Experimental Evaluation of J-integral for Single-edge Bend Specimens. *Journal of Testing and Evaluation*, in press.

RE: CSME Conference Publications Permission Request - Use Copyrighted Material in a Master's Thesis

June 25th, 2014

CSME Publications (csme2014@mie.utoronto.ca)

To whom it may concern:

I am a University of Western Ontario graduate student completing my Master's thesis entitled "INVESTIGATION OF FRACTURE TOUGHNESS MEASUREMENT FOR PIPELINE STEELS BASED ON SE(B) AND SE(T) SPECIMENS". My thesis will be available in full-text on the internet for reference, study and/or copy. Except in situations where a thesis is under embargo or restriction, the electronic version will be accessible through the Western Libraries web pages, the Library's web catalogue, and also through web search engines. These rights will in no way restrict republication of the material in any other form by you or by others authorized by you.

I would like permission to allow inclusion of the material presented in *the CSME International Congress 2014* entitled "Effect of Crack Front Curvature on CMOD Compliance and Crack Length Evaluation for Single-edge Bend Specimens".

The material will be attributed through a citation. Please confirm in writing or by email that these arrangements meeting with your approval.

Yours sincerely

Zijian Yan

FW: CSME Conference Publications Permission Request - Use Copyrighted Material in a Master's Thesis

Dear Zijian Yan,

Yes, it is fine. Permission is granted for you to reuse the CSME paper "Effect of Crack Front Curvature on CMOD Compliance and Crack Length Evaluation for Single-edge Bend Specimens," by Z. Yan and W. Zhou, Proceedings of the CSME International Congress, Toronto, Ontario, Canada, June 1-4, in your Masters dissertation under full citation.

Regards,

Dr. Yu Sun, P.Eng., FCSME, FEIC, FASME, FCAE
University of Toronto
CSME International Congress 2014

RE: JTE-2014-0073.R1 -Reproduction

July 17th, 2014

Dear Mr. Yan,

ASTM International grants permission to reproduce the article, "Effect of Crack Front Curvature on Experimental Evaluation of J-integral for Single-edge Bend Specimens," in your Master's thesis, as requested in your email to Kathy Dernoga dated 16 July 2014, provided the following conditions are met:

1. The article is first published by ASTM International.

2. Your thesis is not published commercially or on a website.

3. The following credit line is used: "Reprinted, with permission, from the *Journal of Testing and Evaluation*, copyright ASTM International, 100 Barr Harbor Drive, West Conshohocken PA 19428-2959."

Thank you for your contributions to ASTM publications program. Should you have any questions, please contact me or Kathy Dernoga.

Kind regards,

Kathe Hooper
ASTM International
100 Barr Harbor Drive, PO Box C700
West Conshohocken, PA 19428-2959
Phone: 610-832-9634
Fax: 610-834-7018
Email: khooper@astm.org

8/2013

ASTM International
Author/Copyright Owner Agreement

Paper/Chapter Title as submitted (the "Work")

For U.S. and foreign government employees *who have prepared this Work as a part of their official duties, it is understood that copyright is not available for assignment. This agreement must be accepted so as to agree to and acknowledge all other terms of this agreement.*

"You" means the Author(s) (and Copyright Owner(s), if different))

Author's Obligations. You have submitted the Work to ASTM for publication. You represent that the Work submitted has not been previously published. You promise that the Work is not currently under consideration by another publication. You warrant that the Work is original material (except for any material from copyrighted sources reproduced with the written permission of the copyright holder sufficient to permit ASTM to use the Work as contemplated), and is in no way a violation or an infringement of any copyright belonging to any third party; that the materials contained in the Work are accurate; and that the Work contains no defamatory or otherwise illegal materials.

You grant the following rights to ASTM: the worldwide and perpetual right to (a) print and/or electronically publish and distribute the Work (or portions thereof) in all versions of ASTM publications (in any language and with the right to translate), websites and/or newsletters and right to print and/or electronically publish and distribute the Work to other sites under license or contract with ASTM; (b) include the Work in advertising and promotion; (c) include the Work in print and non-print products anywhere in the world.

Corresponding Author: The corresponding author is the person with whom ASTM communicates. He/She is responsible for updating all co-authors regarding the status of the Work. The corresponding author is responsible for transferring copyright and has communicated the terms of ASTM copyright with co-authors prior to publication.

Electronically accepting this Agreement represents and warrants that you (and any co-authors) are the sole copyright holder(s) of the Work and that you have identified all co-authors to ASTM. You also represent that each of the co-author(s) have also granted permission to ASTM to use their name(s) in connection with any past, present, or future promotional activity by ASTM, including, but not limited to, promotions for upcoming issues or publications, circulation solicitations, advertising, or other publications in connection with the publication.

Compensation. You will not receive or be entitled to any royalty, fee, commission, payment or other compensation.

Copyright Assignment. It is ASTM's policy to require authors/copyright owners to assign the copyright in the submitted works, in order that ASTM may disseminate the Work to the fullest extent. You hereby assign all rights, including the copyright, in the Work to ASTM, prior to publication, by executing this Agreement. including but not limited to any and all copyright(s) therein held by each Author, together with any rights of each to secure renewals, reissues and extensions of copyright that may be secured under the laws now or hereafter in force and effect in the United States or in any other country, and any and all rights to enforce such copyright(s) or bring other claim in connection with such copyright.

The Work becomes the copyrighted property of ASTM and shall not be published anywhere without the prior written consent of ASTM. ***ASTM reserves the right of first publication of all papers offered for publication.***

The author(s), if different from the copyright owner(s) also represents that he/she/they prepared the Work within the scope of their employment, as a work-for-hire.

Peer Review Policy. All papers are subject to review by two anonymous peer reviewers, as the process is described in ASTM's peer review process (copy will be provided upon request). Submission of Work does not in any way guarantee that ASTM will publish the Work.

Limited Right of Use by Author(s)' Employer. ASTM grants the authors' employer the limited and non-exclusive license to make a limited number of photocopies (hardcopy paper copies, specifically excluding any electronic copies) and circulate these copies within its company for internal purposes. Author(s)' employer acknowledges and will retain ASTM's copyright notice on each hardcopy it makes.

As the Author, ASTM permits you certain uses that do not require permission from ASTM. These include:

- The right to make copies of the Work for your own personal use, including for your own classroom teaching use;
- The right to make copies and distribute copies of the Work to research colleagues, for the personal use by such colleagues(but not commercially or systematically, e.g. via an email list or list serve);
- The right to post the pre-print version of the Work on your website or your employer's website with reference to the publication by ASTM as the copyright holder. This preprint will be sent to you by the copyeditor. This version does not include the final edits. Such preprints may be posted as electronic files on the Author's own website for personal or professional use, or on the Author's internal university or corporate networks/intranet, or secure external website at the Author's institution, but not for commercial sale or for any systematic external distribution by a third party (eg: a list server or database connected to a public access server). Prior to publication, the Author must include the following notice

on the preprint: "This is a preprint of an article accepted for publication in Publication (journal or book) Title, Copyright @ (year), ASTM International, West Conshohocken, PA, doi10/1520_____". NOTE: Directing researchers to the doi will ensure the authors get appropriate citations from CrossRef.

- After publication of the Work by ASTM International, the preprint notice should be amended to read as follows: "This is a preprint of an article published in Publication (journal or book) Title, Copyright @ (year), ASTM International, West Conshohocken, PA, doi10/1520_____, page numbers, www.astm.org". The Author agrees not to update the preprint or replace it with the published version of the Work;
- A PFD of the final version will be supplied to each author and co-author, with a Watermark on the last page that states: "Copyright ASTM International. All rights reserved, date, time. Downloaded by (author's name, affiliation, pursuant to Author/Copyright Owner Agreement. No further reproduction authorized." This version can be given to your employer or funding agency. Continue to direct researchers to the doi for proper CrossRef attribution.
- The right to present the Work at a meeting or conference and to distribute copies of such Work to the delegate attending the meeting after the Work is published by ASTM with appropriate citation to the published article;
- For the author's employer, if the Work is a "work for hire", made within the scope of the author's employment, the right to use all or part of the information in (any version of) the Work for other intra-company use (e.g., training);
- You retain any patent and trademark rights and rights to any process or procedure described in the Work ;
- **The right to include the Work in full or in part in a thesis or dissertation (provided that this is not to be published commercially);**
- The right to use the Work or any part thereof in a printed compilation of works of the author, such as collected writings or lecture notes (subsequent to publication of the Work by ASTM); and
- The right to prepare other derivative works, to the extent the Work is not book-length form, or to otherwise re-use portions or excerpts in other publications, with full acknowledgement of its original publication by ASTM.

Other uses by authors must be authorized in writing by ASTM.

By electronically accepting this Agreement, you agree to all the above terms and limitations.

N:Author_Agreements_Journals_Current/UniversalAuthorCopyright HolderAgreementElectronic(tbo).doc

Curriculum Vitae

Name:	Zijian Yan
Post-secondary Education and Degrees:	Harbin Institute of Technology Harbin, China 2008-2012, Bachelor of Engineering (B. Eng) (Civil Engineering) The University of Western Ontario London, Ontario, Canada 2012-2014, Master of Engineering Science (M.E.Sc) (Structural Engineering)
Honours and Awards:	Western Graduate Research Scholarship (WGRS) 2012- 2014 Graduate Student Teaching Assistantship 2012- 2014 Li & Fung Scholarship 2010 Thomas T.C. Hsu Scholarship 2009
Related Work Experience：	Research and Teaching Assistant The University of Western Ontario 2012-2014

Publications:

Yan, Z., Zhang, S. and Zhou, W. (2014). Model error assessment of burst capacity models for energy pipelines containing surface cracks. *International Journal of Pressure Vessels and Piping*, 120-121, 80-92. DOI: 10.1016/j.ijpvp.2014.05.007

Yan, Z., and Zhou W. (2014). Effect of Crack Front Curvature on Experimental Evaluation of J-integral for Single-edge Bend Specimens. *Journal of Testing and Evaluation*, in press.

Yan, Z., Huang, Y., and Zhou W. (2014). Accuracy of the Double-clip on Gauge Method for Evaluating CTOD of SE(T) Specimens. *Proc. of the 2014 10th International Pipeline Conference*, Calgary, Alberta, Canada, Sep. 29- Oct. 3, one of seven finalists in the 7th student paper competition. Paper No. IPC2014-33219.

Yan, Z., and Zhou, W. (2014). Effect of Crack Front Curvature on CMOD Compliance and Crack Length Evaluation for Single-edge Bend Specimens. *Proc. of the CSME International Congress*, Toronto, Ontario, Canada, June 1-4.

Huang, Y., Zhou W., and **Yan, Z.** (2014). Evaluation of Plastic Geometry Factors for SE(B) Specimens Based on Three-dimensional Finite Element Analyses. *International Journal of Pressure Vessels and Piping*, in press. DOI: 10.1016/j.ijpvp.2014.08.005